Integrated Microreactor System for One-stage Synthesis of Dimethyl Ether from Carbon Dioxide and Hydrogen

Zur Erlangung des akademischen Grades einer

DOKTORIN DER INGENIEURWISSENSCHAFTEN

von der KIT-Fakultät für Chemieingenieurwesen und

Verfahrenstechnik des Karlsruher Instituts für Technologie (KIT)

genehmigte

DISSERTATION

von

M.Sc. Soudeh Banivaheb

aus Kerman, Iran

Tag der mündlichen Prüfung: 27/07/2023

Erstgutachter: Prof. Dr.-Ing. Roland Dittmeyer

Zweitgutachter: Prof. Dr.-Ing. Jörg Sauer

Acknowledgments

I would like to begin by expressing my sincere appreciation to my advisor, Prof. Dr.-Ing. Roland Dittmeyer, for his unwavering support, invaluable guidance, and the wealth of knowledge he shared with me throughout my Ph.D. journey. His exceptional patience, enthusiasm, and insightful vision of the research greatly contributed to my success.

I am also grateful to my group leader, Dr.-Ing. Michael Rubin and Dipl. Chem. Manfred Kraut, for his continuous support. I would also like to extend my gratitude to my collaborators, Dr. Stephan Pitter and Dr. Karla Herrera Delgado at IKFT Institute, for their collaboration and assistance. Furthermore, I would like to acknowledge the valuable contributions of Prof. Dr.-Ing. Jörg Sauer, who served as the reviewer for this dissertation.

I would acknowledge the financial support by the Helmholtz Association of German Research Centers within the Helmholtz-Program Topic 4: ''Power-based Fuel and Chemicals'' and the Vector Stiftung for funding the project "CO_2mpactDME".

Dedication

To **my parents**, whose guidance, love, and unwavering support have been constants in my life. Their presence and encouragement have played a pivotal role in shaping the person I am today.

To **my sisters**, whose enduring love and support have been a source of strength and inspiration. Their belief in me has pushed me to achieve greater heights.

To **my beloved spouse**, who has been by my side throughout this joyful journey, I express my deepest gratitude. Your unwavering love, understanding, and encouragement have been my anchor.

Some passages have been quoted and figures and tables reused from the following published sources:

- S. Banivaheb, S. Pitter, K. Herrera Delgado, M. Rubin, J. Sauer, R. Dittmeyer, Recent Progress in Direct DME Synthesis and Potential of Bifunctional Catalysts, Chem. Ing. Tech. 2022. DOI: 10.1002/cite.202100167.

Abstract

The direct conversion of carbon dioxide into dimethyl ether (DME) with the intermediary use of methanol (MeOH) holds significant potential for realizing the Power-to-X concept. In the frame of this dissertation, the conversion of CO_2 into DME (Dimethylether) is done in decentralized plants via a two-stage reaction with methanol as an intermediate, where a Cu/ZnO-based catalyst (CZ) either promoted with ZrO_2 (CZZ) or with CeO_2 (CZC) is used for methanol synthesis and a solid acid catalyst (HZSM-5) for methanol dehydration. With this purpose, two different Cu-based catalysts were synthesized via flame spray pyrolysis (FSP) method with a semi-continuous process, which now allows the preparation of larger amounts of the methanol synthesis catalyst. The influence of two different promoters, specifically ZrO_2 and CeO_2, on the CZ catalyst was investigated. The catalysts were characterized for their physical and chemical properties, as well as their activity, both individually (CZZ and CZC catalysts) and in combined configurations for the (CO_2-to-DME) CTD reaction. The results demonstrated that the addition of the proper amount of promoter positively affects the dispersion of copper, and enhances the catalyst's activity. The screen-printing method was employed to integrate the catalysts into microchannel reactors, ensuring the formation of sufficiently porous, uniform, and well-adherent catalyst layers. With the intention of achieving this goal, pastes were formulated by the adjusting rheological parameters using various percentages of catalyst and additives. The screen-

printing method was optimized and utilized to create coatings in the form of layers within a microchannel reactor, serving a bifunctional purpose. The integration of CZZ, CZC, and HZSM-5 (Z) catalysts involved arranging them in different configurations, including double layer, hybrid, and face-to-face arrangements. Various operating conditions such as temperature, GHSV, and pressure were explored to achieve higher DME yield. The results indicate that the CZC catalyst outperforms the CZZ in both methanol and direct DME synthesis. Additionally, the close contact between the two catalysts (Cu/ZnO-based catalyst and HZSM-5) causes rapid deactivation of the catalysts. Among the different configurations, the double layer structure (CZZ-Z-DLA and CZC-Z-DLA) were identified as the most favorable catalyst configurations in microchannel reactors, exhibiting high potential for CO_2 conversion and DME selectivity.

Zusammenfassung

Die direkte Umwandlung von Kohlendioxid in Dimethylether (DME) unter Zwischenschaltung von Methanol (MeOH) birgt ein erhebliches Potenzial für die Verwirklichung des Power-to-X-Konzepts. Im Rahmen dieser Dissertation erfolgt die Umwandlung von CO_2 in DME in dezentralen Anlagen über eine zweistufige Reaktion mit Methanol als Zwischenprodukt, wobei ein Kupfer/Zinkoxide (CZ)- basierter für die Methanolsynthese und ein fester Säurekatalysator (HZSM-5) für die Methanoldehydratisierung eingesetzt verwendet wird. Zu diesem Zweck wurden zwei verschiedene Kupfer/Zinkoxide (CZ)- basierter Katalysatoren mittels Flammensprühpyrolyse (FSP) in einem halbkontinuierlichen Prozess synthetisiert, der die Herstellung größerer Mengen des Methanolsynthese Katalysators ermöglicht. Es wurde der Einfluss verschiedener Promotoren, namentlich ZrO_2 und CeO_2, auf den CZ-Katalysator untersucht. Die Katalysatoren (CZZ und CZC) wurden sowohl einzeln als auch in kombinierten Konfigurationen für die CO_2-zu-DME-CTD-Reaktion analysiert, um ihre physikalischen und chemischen Eigenschaften sowie ihre Aktivität zu charakterisieren. Die Ergebnisse zeigen, dass die Zugabe einer geeigneten Menge an Promotor die Dispersion von Kupfer positiv beeinflußt und die Aktivität des Katalysators erhöht.

Die Katalysatoren wurden im Siebdruckverfahren in Mikrokanalreaktoren integriert, wodurch die Bildung ausreichend poröser, gleichmäßiger und gut haftender Katalysatorschichten gewährleistet wurde. Dafür wurden Pasten entwickelt, in denen die

rheologischen Parameter durch verschiedene Konzentrationen von Katalysatoren und Additiven geeignet eingestellt wurden. Das Siebdruckverfahren konnte somit optimiert und zur Herstellung von mehrlagigen Beschichtungen innerhalb eines Mikrokanalreaktors eingesetzt werden, die einen bifunktionalen Zweck erfüllen. Bei der Integration von CZZ, CZC und HZSM-5(Z)-Katalysatoren wurden diese in verschiedenen Konfigurationen angeordnet, darunter Doppelschicht-, Hybrid- und gegenüberliegende Anordnungen. Es wurden verschiedene Betriebsbedingungen wie Temperatur, GHSV und Druck untersucht, um eine höhere DME-Ausbeute zu erzielen. Zudem führt der enge Kontakt zwischen den Katalysatoren (Cu/ZnO-basierter und HZSM-5) zu einer schnellen Deaktivierung beider. Unter den verschiedenen Konfigurationen wurden die Doppelschichtstrukturen (CZZ-Z-DLA und CZC-Z-DLA) als die günstigsten Katalysatorkonfigurationen in Mikrokanalreaktoren identifiziert, da diese ein hohes Potenzial für die CO_2-Umwandlung und DME-Selektivität aufweisen.

Contents

1. Motivation

It is indisputable that the excessive use of non-renewable energy sources such as coal, oil, and natural gas results in adverse effects on the climate as a result of the significant emission of greenhouse gases such as methane and CO_2 that are not effectively [1]. The consensus is that there is an urgent need to significantly decrease CO_2 emissions to reach a net-zero or even net-negative level during the latter half of the 21st century, in order to mitigate the effects of human-caused climate change. The latest assessment report by the Intergovernmental Panel on Climate Change (IPCC) has highlighted that without substantial cuts to carbon dioxide in the upcoming years, global warming could exceed 1.5°C as early as 2030s [2]. To minimize the adverse effects of human-induced climate change, it is imperative to swiftly transition from the current energy system that heavily relies on fossil fuels to one powered by renewable energy (RE) sources. This shift will not only transform the electricity sector, making solar and wind power the primary energy sources, but also impacts the transportation and the chemical industry [3]. Although the chemical industry will continue to rely on chemical energy carriers and hydrocarbon-based feedstocks to some extent, sector coupling between green electricity and chemistry is necessary. However, by nature, corresponding renewable sources (e.g., from solar and wind power) are fluctuating in their availability and usually not accessible in large quantities (rather up to the MW than GW scale) at a certain location [4, 5]. To convert renewable electricity

into chemical compounds that can be easily transported, stored, and utilized in various applications, the use of load-flexible Power-to-X (PtX) technologies is a feasible solution. PtX products may be gaseous, potentially liquefied, such as hydrogen, synthetic methane, and DME, or liquid, such as Fischer-Tropsch hydrocarbons and methanol [6]. Adhering to the principles of PtX, it is feasible to manufacture CO_2-neutral synthetic fuels and chemicals by utilizing green hydrogen produced through water electrolysis powered by renewable electricity, and CO_2 derived from sources like unavoidable industrial process gases, biogas, or other renewable sources. CO_2 can also be extracted from the atmosphere through Direct Air Capture (DAC) technology, especially in regions where it is available in high concentrations [7].

Given the various conceptual factors at play, methanol and DME exhibit potential as PtX-products for the chemical industry and heavy-duty transportation. They can be utilized in various applications, including direct methanol fuel cells, blended with gasoline for combustion engines, and as a replacement for diesel fuel [8]. In decentralized Power-to-Fuel (PtF) methods, it is essential to have streamlined and effective processes. Decentralized plants utilize a two-stage reaction process with methanol as an intermediate to convert CO_2 into DME. Methanol synthesis involves the use of a Cu-based catalyst, while methanol dehydration utilizes a solid acid catalyst. DME can be efficiently liquefied at moderate pressure and transported to a centralized plant where it can be transformed into fuels through conventional large-scale processing. DME is an ideal intermediate for this process due to its favorable physicochemical

properties such as being non-toxic and easy to liquefy, as well as its ability to be synthesized under milder conditions (more energy-efficient) compared to methanol. The latter is due to the fact that by formation of DME methanol is removed from the equilibrium-restricted methanol synthesis step before, which then enables higher synthesis gas conversion. However, for small-scale DME synthesis plants to be economically viable, a highly efficient plant design that employs effective catalysts and optimal plant technology is required. Figure 1.1. illustrate the conversion of CO_2 from renewable sources in to DME and in two stage and one stage of DME production [6, 9].

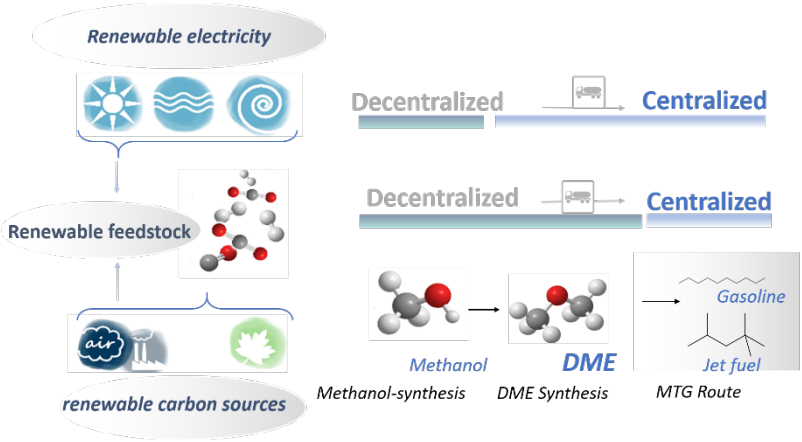

Figure 1-1 Illustration of centralized versus decentralized process for DME synthesis.

1.1 Objective of this Dissertation

The primary objective of this dissertation is to investigate the one-stage synthesis of DME in a microstructured reactor using an optimized catalyst configuration. The aim is to demonstrate process intensification through catalyst optimization and optimal catalyst integration. There are several unresolved scientific challenges that need to be addressed in each aspect of the study.

Firstly, it is crucial to identify, prepare, and extensively characterize an efficient catalyst or catalyst combination with high activity for converting CO_2/H_2 mixtures into methanol. The effect of promoters such as Zr and Ce should be studied to enhance the catalyst's activity. Furthermore, previous investigations have indicated that layer thicknesses exceeding 10 μm do not impose limitations on performance due to mass transport. Therefore, coating strategies for microstructured reactors, specifically based on screen printing, need to be developed. Optimization of paste rheology and screen-printing parameters is important to ensure good adhesion and homogeneous catalyst layers.

To achieve the best synergistic effect and high DME yield, the implementation of two catalysts is necessary: a solid acid catalyst for methanol dehydration and a methanol synthesis catalyst. Different catalyst layer configurations, including hybrid layers, double layers, and Face-to-Face layers, should be designed and evaluated (Figure 1.2).

The optimal conditions for DME synthesis need to be determined by considering the influence of temperature, pressure, and gas space

velocity. Experimental design should be employed to identify the operating conditions that yield high methanol and DME production. Additionally, the interaction between the synthesized CTM (Carbon dioxide to Methanol) catalysts ($CuO/ZnO/ZrO_2$ and $CuO/ZnO/CeO_2$) and the MTD (Methanol to Dimethyether) catalyst (zeolite-HZSM-5) in the integrated system should be analyzed.

Overall, this dissertation aims to address these scientific challenges and provide insights into the efficient synthesis of DME by optimizing catalyst configurations and operating conditions in a microstructured reactor.

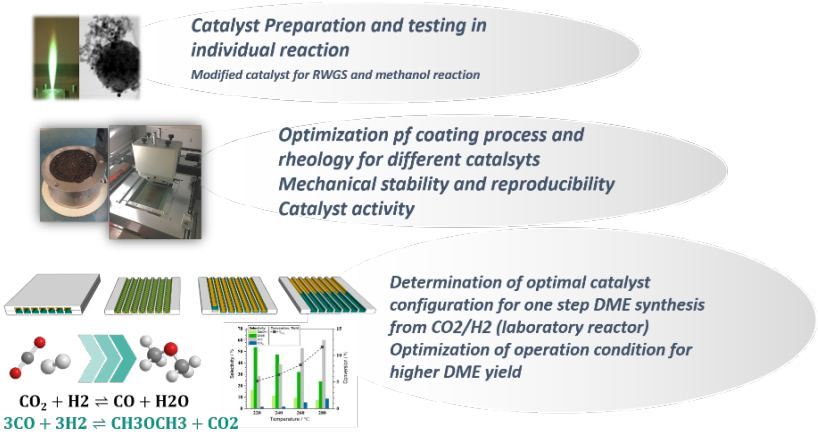

Figure 1-2 Outline of the study on one-stage integrated CTM-MTD process in microchannel reactor.

2. Introduction and Background

2.1 MeOH Synthesis

The conventional process for producing methanol involves using a copper-zinc-based catalyst and synthesis gas streams consisting of CO/H_2. The reaction occurs based on the stoichiometric reaction (R1, STM: syngas to methanol). This process entails the creation and refinement of syngas, the synthesis of methanol, and the distillation of crude methanol [6].

$$CO_{(g)} + 2 \cdot H_{2(g)} \rightleftarrows CH_3OH_{(g)} \qquad \text{(R1)}$$

$$\Delta H^0_{298.15\,K} = -90.6\ \text{kJ} \cdot \text{mol}^{-1}$$

$$\Delta G^0_{298.15\,K} = -25.2\ \text{kJ} \cdot \text{mol}^{-1}$$

Currently, the annual production of methanol is approximately 110 million metric tons, with the majority being produced through the oxidation and/or reforming of natural gas [10], as well as coal gasification using low and medium pressure processes [2]. Syngas can also be derived from various other sources such as crude oil, residual oil, and bio-waste products, which are widely available globally, including agricultural residues, forestry or landscaping waste, and paper waste [11]. Recently, there has been a growing interest in using CO_2 from the air or from inevitable industrial emissions (e.g. steel industry) as a carbon source for methanol

production. This approach allows for a significant reduction in the environmental impact of greenhouse gases and offers the opportunity to use low cost carbon source [11–13]. The utilization of green hydrogen, which is generated from renewable sources through electrolysis, enhances the efficacy of producing synthetic fuels from CO_2 [14, 15]. The conversion of CO_2 to methanol through hydrogenation (R2) is a less exothermic process than the production of methanol from pure syngas. Moreover, it necessitates the implementation of the water-gas-shift reaction (RWGS, R3).

$$CO_{2(g)} + 3 \cdot H_{2(g)} \rightleftarrows CH_3OH_{(g)} + H_2O_{(g)} \quad \text{(R2)}$$

$$\Delta H^0_{298.15\,K} = -49.4\ \text{kJ} \cdot \text{mol}^{-1}$$

$$\Delta G^0_{298.15\,K} = +3.5\ \text{kJ} \cdot \text{mol}^{-1}$$

$$CO_{(g)} + H_2O_{(g)} \rightleftarrows CO_{2(g)} + H_{2(g)} \quad \text{(R3)}$$

$$\Delta H^0_{298.15\,K} = -41.2\ \text{kJ} \cdot \text{mol}^{-1}$$

$$\Delta G^0_{298.15\,K} = -28.6\ \text{kJ} \cdot \text{mol}^{-1}$$

When CO_2 is used as a feedstock in the production of methanol, it can lead to additional challenges, such as the loss of catalyst activity due to water formation [16]. The deactivation could be due to different reasons like blocking active sites for CO_2 and producing carbonate or formate species or blocking of hydrogen adsorption sites, morphology changes of Cu [17, 18]. Researchers are currently working on developing catalysts with higher service lifetimes,

particularly under high CO_2-rich syngas conditions. Several studies are being conducted to address this challenge and improve the performance of the catalysts used in the process which will explained in the next sections [16, 19, 20].

The conversion of syngas into methanol through the hydrogenation of CO and CO_2 is limited by the kinetics and thermodynamic equilibrium of the reversible and strongly exothermic reactions involved. Therefore, it is necessary to maintain an optimum process temperature of 200-300°C through effective heat removal. To enhance the CO and CO_2 conversion and increase the process yield, new techniques such as once-through process with interstage [19] and in situ methanol removal [21] have been suggested, which eliminate the need for gas recycling [6, 21].

2.1.1 Recent Developments in Catalyst Design

There are many review articles on catalysts for methanol synthesis, reflecting its great importance. The following sections summarize the latest developments in the most important catalyst groups for use in fundamental research and process development for methanol synthesis.

Transition Metal-based Catalysts

Commercially available catalysts containing CZA ($CuO/ZnO/Al_2O_3$) typically possess a metal distribution that falls within the range of 60 wt.% Cu, 30 wt.% Zn, and 10 wt.% Al. This category of catalysts was developed by Imperial Chemical Industries (ICI) in the 1960s to allow for methanol synthesis under more moderate reaction conditions (5-

10 MPa, 220-300°C) [22, 23]. The impact of ZnO in multi-component catalysts based on Cu typically arises from the combination of advantageous stoichiometry and optimized production methods, resulting in two main benefits. Firstly, ZnO acts as a geometric spacer between the Cu centers in the nanometer size range, leading to an enhancement in Cu dispersion and increased accessibility of the specific Cu surface [24, 25]. Secondly, ZnO has a modulating effect on the electronic properties due to specific metal/support interactions (SMSI). Conversely, Al_2O_3 serves as a structural promoter, promoting a homogeneous distribution of Cu and improving the mechanical stability of the catalyst. Promoters, such as ZrO_2 [26], TiO_2 [27], MgO [28], or Ga_2O_3 [29] also are used to improve the catalytic performance. Amongst the aforementioned metal oxides, ZrO_2 has been one of the most extensively researched modifiers for enhancing the CZ (CuO/ZnO) catalyst [30–32]. The improved performance of the CZZ (CuO/ZnO/ZrO_2) system can be attributed to the weak hydrophilic nature of zirconium oxide, which prevents the strong adsorption of water, as well as the rise in surface basicity, which promotes CO_2 adsorption and, consequently, the productivity of methanol. Furthermore, ZrO_2 promotes the creation of oxygen vacancies during reduction, which enhances Cu dispersion and, thus, multiplies Cu-ZnO interactions [33]. Both the improvement in Cu dispersion and the rise in Cu-ZnO contacts are explained by the increase in the stability of the Cu+ sites caused by interaction with zirconia [34]. CeO_2 is another promising promoter due to its weaker hydrophilic characteristic than alumina, which may boost the dispersion of copper as it interacts strongly with Cu and the basicity of the surface.

Due to its distinctive structural characteristics, which include oxygen vacancies and reversible valence changes (Ce^{4+} and Ce^{3+}), CeO_2 exhibits tremendous potential. It can serve as an active site for CO_2 activation of oxygen-containing bonds as well as a carrier for immobilizing catalytically active [35]. Arena et al. investigated the influence of various oxide carriers on regulating the catalytic functionality of the Cu-Zn catalyst for hydrogenation of carbon dioxide [36]. They discovered that ceria significantly enhances the Cu-ZnO system's ability to adsorb CO_2 and function. As the methanol dehydration reaction directly benefits from the zeolite's acid characteristics, including the acid type and acid sites, this has an impact on the selectivity of DME in the methanol-to-DME conversion process [37, 38]. Shuai Chang et al. looked into the effect of Zn/Ce ratio of Cu/Zn/CeO_2 catalyst which was synthesized through co-precipitation method. They found that a higher amount of Ce content improves the dispersion of Cu which led to a rise in oxygen vacancies. More basic sites and oxygen vacancy concentrations develop on the catalyst as the CeO_2 level rises, facilitating CO_2 activation [35]. Gao and colleagues prepared Cu-ZnO-based catalysts using hydrotalcite-like precursors and observed that the incorporation of CeO_2 resulted in a rise in the copper surface area and the proportion of highly basic sites. Consequently, the promoted catalyst exhibited greater CO_2 conversion and CH_3OH selectivity than the unpromoted catalyst [39].

Active Sites and Structure–Activity Relationships

Essentially, two possible active sites at the interface are discussed.

One possibility (a) results from the synergy between Cu and ZnO at their interface [40]. The second possibility (b) is the presence of Cu-Zn surface alloy sites, [41] which is related to the partial reduction of ZnO particles towards a $Zn^{\delta+}$ state or favours the modification of the surface Cu by metallic Zn [42–45]. Recent research results regarding the aforementioned "possibility (a)" have been published indeeding experimental data and simulations, which give clear indications about the nature of the top layer of the catalyst surface in Cu/ZnO catalysts [46, 47]. "Possibility (b)" is supported by findings suggesting that Cu steps occupied by Zn atoms are the active sites where coexistence of defined bulk defects and surface species exists [20] . The SMSI-induced formation of a metastable ZnO_x phase on the Cu active sites has also been demonstrated on reduced industrial Cu-ZnO-Al_2O_3 catalysts [42]. The adsorption strength of relevant intermediates such as HCO*, H_2CO* and H_3CO* is also enhanced via Cu-Zn interaction according to DFT calculations [20]. Control of the nanoscale properties of catalysts for methanol synthesis is therefore generally an essential element in catalyst development.

Recently, inverse oxide/metal catalysts with metastable "graphite-like" ZnO layers in Cu/ZnO/Al_2O_3 catalysts have also attracted considerable interest due to the metal-support interaction, [42, 46–48] with ZnO sites being considered as hydrogen reservoirs to favour methanol formation.

Preparation Methods

Out of numerous methods available to optimize the catalytic activity, the co-precipitation process is the most commonly employed

technique, which involves mixing metal salt precursors with a precipitating agent in an aqueous medium, followed by aging, calcination, and reduction [49, 50]. It is crucial to control the synthesis conditions such as temperature, pH value, mixing, and aging procedure for effective results [51]. Many modifications have been made to avoid metal agglomeration and sintering during the calcination process, which is necessary for proper metal dispersion and catalytic performance. These modifications include nitrate-free synthesis using a basic formate or acetate precursor, surfactant-assisted coprecipitation, reverse co-precipitation, reverse co-precipitation with ultrasound irradiation, and continuous co-precipitation [19, 33, 52–57]. Apart from co-precipitation, there are various other synthesis methods such as deposition-precipitation, sol-gel synthesis, citrate decomposition, combustion synthesis, solid-state synthesis, ammonia evaporation, organometallic synthesis, and flame-spray pyrolysis [58–65].

Flame spray pyrolysis (FSP) is a potential technique for producing catalysts for methanol synthesis due to its ability to provide benefits such as adaptability, efficiency, and scalability. Flame spray pyrolysis enables the production of uniform and well-formed particles due to the high temperature and rapid particle growth through sintering and coalescence. Despite this, the particles retain their nanoscale characteristics because of the short residence time and substantial temperature gradient during the synthesis process [66]. Controlling certain properties of multi-component particles produced (such as size, composition, and morphology) in a single nozzle configuration can be challenging. For the production of a catalyst system with a

specific particle configuration, it may be more beneficial to use a multi-nozzle (where the precursor solution is sprayed from two different nozzle with the specific angle) FSP system to regulate the formation of particles and the injection rate of different metal precursor solutions. For instance, Strobel et.al synthesize $BaCO_3/Al_2O_3$ particles with two nozzle flame without formation of $BaAl_2O_4$ [67]. The formation of particles in FSP can occur through either the droplets-to-particle route or the gas-to-particle route, depending on the precursor formulation (metal concentration and combustion enthalpy). The droplets-to-particle route can result in micron-sized particles due to incomplete droplet evaporation, while the gas-to-particle route, which occurs due to the supersaturation of metal vapor, is preferred in this method because it ensures particle size in the nano range as well as homogeneity. Therefore, the selection of metal precursors and solvents with suitable combustion enthalpies, melting/decomposition temperatures, miscibility, and chemical stability is critical to the overall particle formation in the flame, which determines the resultant particle properties. The particle size and crystal structure of FSP-produced particles are determined by their reaction temperature and residence time. Additionally, the feeding rate and choice of solvent can affect the homogeneity of particle size and shape, as well as the BET surface area [65, 66]. Jensen et al. showed that it is possible to produce $Cu/ZnO/Al_2O_3$ catalysts with a specific surface area greater than 100 m^2/g_{cat} by utilizing a flame combustion technique [68]. A series of Cu/ZrO_2 catalysts was prepared by Copéret et al. using a two-nozzle spray pyrolysis method, where only the Cu particle size was changed

with higher dispersion gas flow (O_2) for the Cu nozzle spray. The researchers observed that the catalysts with smaller Cu particle size exhibited higher activity and selectivity towards CH_3OH in CO_2 hydrogenation [69].

Precious Metal-Based Catalysts

Cu-based catalysts have some unfavourable factors, such as the increased mobility of ZnO when water is formed, the limited stability due to sintering and agglomeration, and partly pyrophoric properties [70, 71]. As an alternative to Cu-based catalysts, precious metal-based catalysts are often used because they have high stability and better resistance to sintering and poisoning.

Monometallic Catalysts

Pd and Pt supported catalysts have been found to be effective in catalyzing methanol formation through CO hydrogenation at low temperatures [72] . The use of Pd catalysts on supports such as La_2O_3, Nd_2O_5, and CeO_2 have been found to be highly selective in the formation of methanol [73]. Supports with existing oxygen vacancies, such as CeO_2 and In_2O_3, have been found to facilitate CO_2 adsorption or activation in Pd-based catalysts [74, 75] . Additionally, Au-based catalysts on various supports [76, 77] as well as Pt-based catalysts [74] have demonstrated catalytic activity in the formation of methanol.

Alloy Catalysts

Pd and Pt form various alloys with metals that are active themselves in CO/CO_2 hydrogenation. In such alloys, the surface properties are altered compared to the pure metals, so that new active sites can be

created, [78] such as in Pd-Cu, Pd-Zn and Pt-Co alloys, among others. In Pd-Zn alloys, the SMSI effect between metallic Pd and ZnO at high temperatures ensures the formation of a stable alloy, although the nature of the active sites is the subject of scientific debate [79]. On the one hand, the formation of PdZn alloys often correlates with catalytic activity and methanol selectivity [80–83]; however, Pd nanoparticles decorated with ZnO_x islands are partly discussed as active sites [84]. In this context, PdZn alloys could stabilise formate intermediates and inhibit the RWGS reaction at the same time [84, 85].

Other Catalysts

In_2O_3 and Ga-based Catalysts

In recent years, In_2O_3-based catalysts have emerged as a highly selective catalyst for methanol production, with a key effect being the suppression of the reverse water-gas shift reaction pathway [86–88]. These catalysts have shown good long-term stability when combined with suitable support materials such as monoclinic zirconia, which enhances the CO_2 adsorption capacity [89–91]. To increase the rate of H_2 cleavage, which is limited in bulk In_2O_3, doping with hydrogenation-active metals such as palladium [92, 93], platinum [94], rhodium [95] or nickel [92] has been explored. Gallium has also been used in various methanol synthesis catalysts [96], including Ga_2O_3 supported Pd catalysts, where it is believed to promote CO_2 adsorption, and Pd catalyses the dissociation of H_2 resulting in hydrogen spill-over to the oxide surface and the formation of formate [97]. Among various alloys, Ni_5Ga_3 has been found to be particularly active and selective in terms of methanol synthesis [98].

MOF/ZIF-based Catalysts

Metal-organic frameworks (MOFs) and zeolitic imidazolate frameworks (ZIFs) are considered highly attractive materials for methanol catalysts due to the structure sensitivity of the reaction. These materials offer tailored surface accessibility, pore functionalities, and reactive open metal sites [99]. The unique feature of these frameworks is the ability to confine catalytically active metal nanoparticles (NPs) within their structures, thereby minimizing the possibility of their aggregation or agglomeration [100]. Different methods can be used to prepare MOF/ZIF- based catalysts for methanol synthesis, which can be broadly classified into two types: Bottom-up and top-down approaches. In the bottom-up approach, the catalyst is prepared by impregnation, similar to the preparation of the composite ZIF-8-supported Pd catalyst [81]. For example, a ZIF-8-supported Cu catalyst has been synthesized using this approach [101]. which showed considerable methanol productivity. On the other hand, in the top-down approach, NPs are encapsulated in the framework by selecting appropriate precursors. A highly active MOF-supported Cu/ZnOx catalyst was prepared using the top-down method [31], along with a ZrOx-supported Cu/ZnOx catalyst [102]. Another method involves the MOF directed synthesis of a Cu catalyst highly dispersed in graphene [103].

2.1.2 Process Modeling of Methanol Synthesis

For many years, researchers have investigated the synthesis of methanol. Despite this, they have not yet fully grasped the reaction mechanism and the recovery processes associated with the typical

Cu-based catalyst. Gaining a complete understanding of the mechanism would enable experts to fine-tune input parameters and reaction conditions accurately, leading to improved process efficiency and economic viability [104]. Over the years, multiple formal kinetic models have been suggested for methanol synthesis [105–109]. Each model has its unique factors to consider, such as rate determining steps (RDS) and lumped parameters fitted to experimental data at various conditions. As a result of these assumptions and fitting of unknown parameters, various effects may blend with the kinetic model, leading to its deviation from the experimental data.

Theoretical models based on first principles Density Functional Theory (DFT) calculations have been suggested for methanol synthesis, incorporating different surface reaction pathways where all reactions may be rate limiting [110–116]. These models are deemed more appropriate for extrapolation purposes than empirical models, which rely on numerous experimentally fitted parameters [114, 117]. Despite their advantages, implementing theoretical models for methanol synthesis is more complicated and computationally demanding than using simplified kinetic models [118]. Earlier theoretical [19, 44, 98] and experimental research [119–121] conducted on methanol catalysts revealed a synergistic impact of metallic components in the catalyst, resulting in reversible structural changes reaction conditions. This also significantly affects the active sites on the catalyst surface, which influences catalytic activity. Despite the understanding of these alterations, modeling their dynamic behavior remains difficult and incomplete [122]. This

underscores the significance of transient mechanistic investigations paired with fundamental in situ catalysis research in developing kinetic models. Advanced analytical techniques such as X-ray diffraction and absorption spectroscopy (XRD, XAS) [119] and diffuse reflectance IR-spectroscopy (DRIFTS) [123, 124] are now more accessible for in situ and operando analysis. These methods allow for the creation of more sophisticated models based on a fundamental understanding of individual steps. However, as pointed out by Fehr and Krossing [124], particular attention must be paid to correctly assigning IR bands (CO_2 gas molecule versus adsorbate) when studying technically relevant conditions using IR spectroscopy. This is because several combination bands and overtones of CO_2 molecules can lead to misinterpretations.

Recently, multi-scale modeling has been employed to create more comprehensive models that accurately describe the chemistry involved in methanol synthesis [108, 114, 125]. These models incorporate surface reaction kinetics, significant intermediates, diverse active sites, and in some cases, structural modifications (an example is illustrated in Figure 2.1). However, there is still a need for further enhancements to improve the accuracy of kinetic and surface activity models in describing the behavior of methanol catalysts.

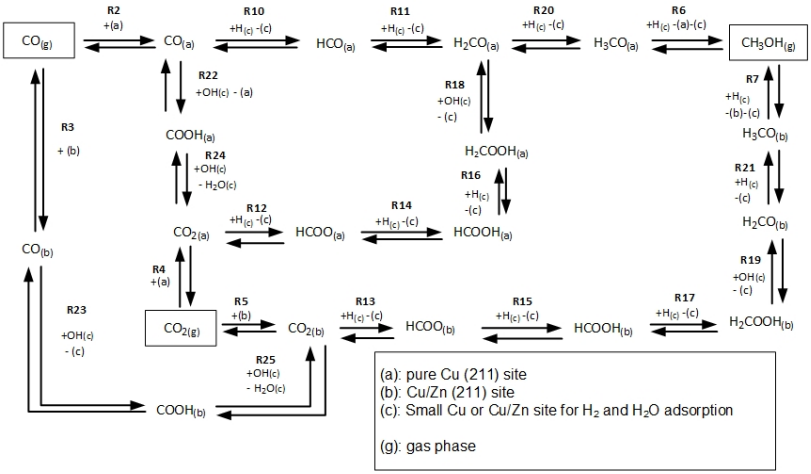

Figure 2-1 Reaction network of the carbon-containing species in the methanol synthesis and the WGSR. Adapted from Ref. [114] with permission from the Royal Society of Chemistry.

2.2 DME Synthesis

2.2.1 Two-step Synthesis of DME

The main method for producing DME on a large scale involves the dehydration of methanol (MTD: methanol to dimethyl ether). The initial step in this process is the production of methanol from synthesis gas, which occurs on Cu/ZnO-based catalysts at temperatures between 240 and 280°C and pressures ranging from 3 to 7 MPa, as described by reaction equation (R1). After the methanol is purified in a subsequent reactor, it is converted into DME using an acid catalyst, as described by reaction equation (R4) [126].

$$2 \cdot CH_3OH_{(g)} \rightleftarrows CH_3OCH_{3(g)} + H_2O_{(g)} \quad \text{(R4)}$$

$$\Delta H^0_{298.15\,K} = -23.4\ \text{kJ} \cdot \text{mol}^{-1}$$

$$\Delta G^0_{298.15\,K} = -16.8\ \text{kJ} \cdot \text{mol}^{-1}$$

The indirect process involves the production of methanol from synthesis gas, followed by its conversion into DME through an acid catalyst. The composition of the synthesis gas depends on the carbon content of the carbon source and ideally corresponds to the stoichiometry of methanol synthesis. Technical synthesis gas compositions usually contain proportions of CO_2 and CH_4 of <5% each. Methanol dehydration in the indirect process is exothermic and takes place at lower temperatures of around 200°C to avoid the formation of by-products. However, the thermodynamic limitation of methanol formation results in low gas conversion per pass (15-25%), leading to high capital and operating costs at increased recirculation rates.

2.2.2 Direct Synthesis of DME

The direct process, also known as the one-stage process or STD (syngas to dimethyl ether), is an alternative to the indirect process. In this process, both methanol synthesis and the dehydration of methanol to DME occur in the same reactor using a bifunctional catalyst system. The process is designed to favor primary methanol formation, and it has been described in previous literature [127, 128]. The direct process is currently being tested on an experimental scale up to a pilot demonstration level, and it is not yet commercially

available. The economic benefits of the direct process are often discussed, as it requires only one reactor, and the conversion during methanol formation can be increased through the parallel process of methanol dehydration, as shown in Figure 2.2. As a result, lower pressure is needed, and methanol synthesis can occur at higher temperatures, resulting in a higher reaction rate. However, higher reaction temperatures are not ideal for DME formation. In the direct DME synthesis process, water is generated during dehydration, which causes the RWGS reaction (reverse reaction (R3)) to occur. As a result, the direct process requires a lower H_2/CO ratio for DME production than for methanol synthesis alone, and it is especially suitable for converting biomass-produced syngas [129].

$$3\,CO_{(g)} + 3 \cdot H_{2(g)} \rightleftarrows CH_3OCH_{3(g)} + CO_{2(g)} \qquad \text{(R5)}$$

$$\Delta H^0_{298.15\,K} = -246.0\ \text{kJ} \cdot \text{mol}^{-1}$$

$$\Delta G^0_{298.15\,K} = -95.7\ \text{kJ} \cdot \text{mol}^{-1}$$

The direct process is less favorable for the direct hydrogenation of CO_2 or the conversion of CO_2-rich synthesis gas, resulting in lower DME yield [130]. However, reducing the carbon footprint of peak power generation from CCU fuels is a key driver in current process technology development through the use and recycling of CO_2. In the synthesis of methanol or DME from CO_2-rich synthesis gas, the reverse water gas shift reaction (R3), CO_2 or CO hydrogenation (R1, 2), and methanol dehydration (R4) are involved, resulting in a net reaction (R6) for the direct synthesis of DME from CO_2/H_2 synthesis gas.

$$2\,CO_{2(g)} + 6 \cdot H_{2(g)} \rightleftarrows CH_3OCH_{3(g)} + 3 \cdot H_2O_{(g)} \qquad \text{(R6)}$$

$$\Delta H^0_{298.15\,K} = -122.2\ \text{kJ} \cdot \text{mol}^{-1}$$

$$\Delta G^0_{298.15\,K} = -9.8\ \text{kJ} \cdot \text{mol}^{-1}$$

To achieve maximum DME yield, CO_2 hydrogenation should ideally be performed near equilibrium by either operating at high pressure or at lower temperatures [131]. However, higher temperatures can lead to increased consumption of CO_2 and H_2 through the RWGS reaction, resulting in higher H_2O content which can hinder DME formation. This can occur due to the competing adsorption on the active centers of the methanol catalyst [132] and on the acidic centers of the dehydration catalyst [133].

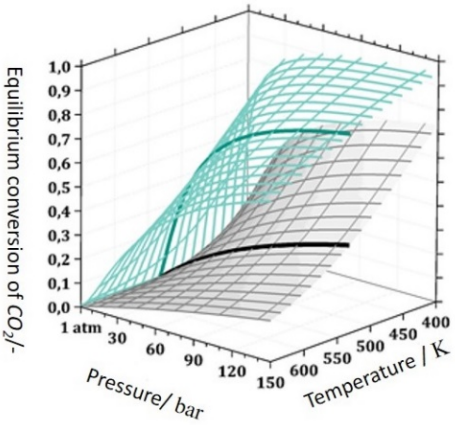

Figure 2-2 Thermodynamic equilibrium conversion of CO_2 as a function of temperature and pressure for methanol and direct DME synthesis from CO_2/H_2 = 3/1.

2.2.3 Process Development

To increase the efficiency of the direct synthesis of DME from $H2/CO/CO_2$, various reactor designs have been suggested and studied. This review will specifically concentrate on two process intensification methods, microstructured and membrane reactors, which have shown promise for the direct synthesis of DME [134].

Microstructured Reactors

To describe reactor concepts with tailored structuring of the reaction and/or cooling section, the term "microstructured reactor" is used. This type of reactor is designed to improve heat and mass transport characteristics through microstructuring. It is important to note that the term "microstructured" does not refer to the size of the reactor, and structures in the dimension of 10^{-3} m are also commonly referred to as microstructured [135]. Although microstructured devices are typically created by stacking pre-fabricated foils, recent advances in additive manufacturing have allowed for more flexibility in designing the internal structure of these devices. This is not possible with traditional microfabrication techniques like milling, slotting, or etching.

Generally, there are two main approaches to incorporating catalysts into microstructured reactors. One approach involves packing the catalyst into the microchannels, while the other involves coating the inner walls of the microchannels with catalysts. Tailored coatings, which may be multifunctional, are used in the latter approach to achieve a low pressure drop and improved heat transfer [136], and may provide additional features to the reactor system. A third

approach involves constructing the entire reactor from the catalytically active material, such as Rh [137], Cu or Ag [138]. To convert H_2/CO/ CO_2, microstructured reactors have been used to synthesize hydrocarbons such as methanation [139] Fischer-Tropsch synthesis [140] and oxygenates, such as methanol synthesis [95] and DME [141], through the application of tailored cooling concepts. Allahyari et al., [142] investigated microreactors coated (wash-coating) with CZA-HZSM-5 catalysts with varying thicknesses of 20 μm to 60 μm. They found that increasing the catalyst loading resulted in a less uniform morphology. They found that the performance of the microreactor is hindered as the thickness increases (60 μm), despite the larger number of active sites, due to the decreased availability of these sites caused by the greater diffusion distance. At high feed flow rates, the microreactor experiences a substantial decrease in residence time, resulting in a significant decline in performance when a thick layer of catalyst coating is present.

Membrane Reactor

A membrane reactor combines a chemical reaction and product separation within a single unit. The ''in situ'' removal of the product or by-product from the reaction zone through a membrane provides several benefits. It allows for an increase in conversion by modifying the thermodynamic equilibrium through the withdrawal of the (by)product. Moreover, in the case of selective product separation, it enables the collection of the product with enhanced purity. Additionally, selective product separation can improve product purity [143, 144]. Incorporating a membrane (whether porous,

organic, or inorganic) into a reactor while maintaining high selectivity (i.e., a defect-free membrane) under reaction conditions is a common challenge. Typically, tubular membrane systems or planar systems with the catalyst inside are used to address this challenge [145, 146]. For methanol and direct DME synthesis, the removal of the byproduct water using a membrane is discussed to increase product yield by increasing and decreasing the partial pressure of the reactants and the inhibiting byproduct water, respectively, which helps to protect the catalyst from deactivation], [147, 148].

A zeolite-based membrane reactor was reported to have achieved improved CO_2 conversion and high methanol yield compared to a conventional reactor at different H_2/CO_2 feed ratios and temperatures [149, 150].

Gorbe et al. [151] conducted an experiment to measure the permeation of a mixture of H_2, CO_2 and H_2O through a zeolite A membrane in the temperature and pressure range suitable for methanol synthesis (160–240°C, 10–27 bar). They focused on the membrane's ability to selectively separate water and methanol by comparing the water partial pressure in the permeate and retentate sides. The experiment was conducted with a retentate side temperature range of 160-260°C and a feed water pressure of 10-18 kPa. The authors found that there was a surprisingly high-water partial pressure in the permeate, which they attributed to the radial temperature in the experimental system.

Li et al. [148] incorporated a Na+-gated water-conducting membrane into the direct DME synthesis reactor to create a dry reaction environment. This allowed for a 4- and 10-fold increase in the

activities of the CO_2 hydrogenation catalyst (CZA) and methanol dehydration catalyst (HZSM-5), respectively, due to the absence of water. The authors reported single-pass CO_2 conversion rates of up to 73.4%, which is well beyond the thermodynamic equilibrium of the bare methanol synthesis, and DME yields of up to 54.5%. Furthermore, they demonstrated a reduction in catalyst deactivation. Brunetti et al. [152] used ZSM-5 type zeolite membranes supported on TiO_2 and γ-Al_2O_3 as catalytic membrane reactors for DME synthesis via MeOH dehydration. They investigated the effect of two different support structures on the zeolite membrane as a function of temperature and feed pressure, covering a wide range of accessible feed compositions. The researchers found that the ZSM-5 supported on γ-Al_2O_3 had higher methanol conversion than the TiO_2 supported membrane (as shown in Figure 2.3), indicating that the membrane support had an influence on the process. This was attributed to an enhancing effect induced by γ-Al_2O_3, which increased methanol dehydration. Both membrane reactors showed exclusive formation of DME.

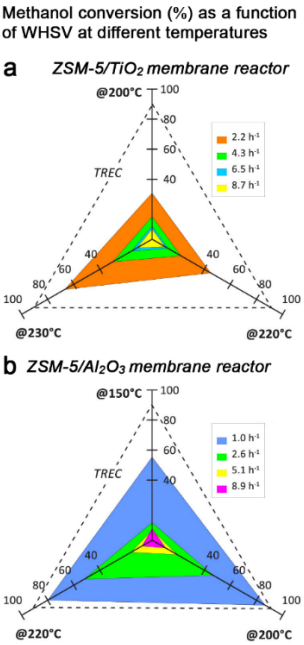

Figure 2-3 Methanol conversion as a function of temperature and WHSV in a catalytic membrane reactor with the zeolite ZSM-5 membrane supported on TiO_2 (a) and Al_2O_3 (b). Dashed lines connect the equilibrium MeOH conversion at the temperatures indicated. Feed pressure=120 kPa. MeOH concentration =100% molar. Reproduced with permission [152]. Further permission related to the material excerpted should be directed to the ACS.

Rodriguez-Vega et al. [153] investigated the performance of a packed bed membrane reactor (PBMR) for direct synthesis of dimethyl ether (DME) via the hydrogenation of CO_2 and CO_2/CO mixtures. A hydrophilic LTA zeolite membrane was employed to remove water from the reaction mixture, as it was found to have superior permeation properties compared to other zeolites (LTX and SOD). The PBMR was equipped with a mechanically mixed catalyst system

comprising CZZ/SAPO-11, and both the feed and sweep gas (permeate side) had the same composition and flow rate. The results showed that the CO_2 conversion achieved with the PBMR was higher than that of the conventional packed bed reactor (PBR) without the membrane by up to 37% at 325°C.

To learn more about the current state of separation and the reaction mechanism in catalytic membrane reactors, readers can refer to a recent review by Li et al. [154]. This article discusses different types of high-temperature water and gas separating membranes and their applications in membrane reactors for CO_2 utilization.

2.2.4 Process Modeling DME

To improve the overall efficiency of the DME synthesis process, it is crucial to identify and quantify the relationships between process parameters and performance using an appropriate mathematical description and precise predictions derived from all relevant chemical and physical processes [155].

Researchers have conducted numerous investigations to describe and simulate the impact of variable CO/ CO_2 content feeds and different catalyst bed compositions based on thermodynamic and kinetic data. As a result, models have been proposed to quantitatively describe the direct DME synthesis process and generate predictions [130, 155, 156]. Studies on optimizing the composition of the dual catalyst bed using models have shown that an optimized distribution with a higher quantity of methanol catalyst improves catalytic performance, resulting in a substantial shift towards equilibrium CO or CO_2 conversion [155–157].

Various modeling techniques have been utilized to simulate the direct DME synthesis process. One of the initial approaches involved coupling models for methanol formation [105, 106, 109] with models for its dehydration [158, 159]. However, in recent years, lumped kinetic models have been developed based on prior knowledge of the direct CO/CO_2 conversion to DME [155, 156, 160]. The simplified models have certain limitations due to possible model deficiencies caused by assumptions and uncertainties in the mathematical description, particularly outside the fitted operational conditions. Although formal kinetic models have been extensively used, their inability to describe significant changes on the catalyst during time on the stream has prompted a microkinetic modeling approach [118, 161]. While some microkinetic studies have been conducted for methanol dehydration to DME [161–164], none have been found for direct DME synthesis. However, recent studies have utilized artificial neural networks (ANNs) due to their flexibility and robustness [165–169], as traditional models such as formal kinetic models may have limitations in describing catalyst changes during operation outside of fitted conditions. The use of ANNs to optimize process conditions and predict the performance for the direct DME synthesis has been studied [165, 170–172]. The ANN-based models are flexible in adapting new data, their accuracy is higher, and they proved to be applicable to extrapolations outside known experimental conditions.

2.2.5 Concepts on Catalyst Application for Direct DME Synthesis

As discussed earlier, combining methanol synthesis with its dehydration can result in a higher conversion of CO and CO_2 than the equilibrium conversion achieved through methanol synthesis alone. However, to achieve this synergistic effect, the two catalysts involved (methanol synthesis catalyst, and solid acid catalyst for methanol dehydration) must be properly implemented. Figure 2.4 illustrates various concepts related to this.

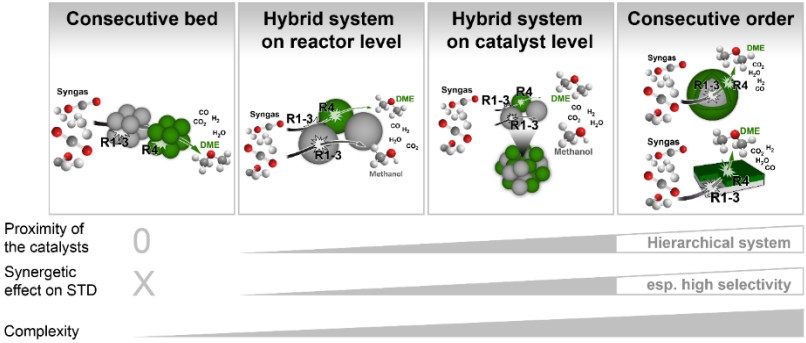

Figure 2-4 Schematic depiction of different catalyst integration strategies for the direct synthesis of DME.

As the two catalysts involved in the methanol synthesis and its dehydration are brought closer together, the potential synergy as well as the design and preparation of the catalyst system are affected. One of the simplest ways to combine the two catalysts is to mix the particles or pellets on the reactor level, which is referred to as a hybrid catalyst bed. This approach has been reported in several studies [132,

173, 174]. A mixture on the catalyst bed level increases the proximity of the active sites for the two reactions and, thus, decreases the probability for the intermediate (MeOH) to leave the reactor without getting dehydrated to DME. Combining the two catalysts on the particle level increases the closeness of the active sites involved in the two reactions, resulting in a further decrease in the likelihood of the intermediate (MeOH) escaping the reactor without undergoing dehydration to form DME. This has been supported by various studies [175–180]. The previously mentioned approach can be achieved by combining the dried STM- and MTD-catalysts through mixing [176, 179, 180]. This can be done by preparing a suspension of the two catalysts, filtering, washing, drying and calcination before pelletizing [177, 181]. Additionally, it has been reported that co-precipitation of the STM catalyst in a suspension containing MTD catalyst [174] and self-assembly of the metallic and acidic functionalities are also possible methods [182]. These methods enable improvement and customization of the proximity of the two components. However, the specific arrangement of the two catalysts within the pellet cannot be precisely controlled, even though these preparation approaches can adjust the desired weight ratio of the STM-/MTD-catalyst. To overcome the imprecise arrangement of the two catalysts within a pellet, synthesizing hierarchically structured bifunctional catalysts is a promising alternative. This approach aims to achieve a desired arrangement of the two catalysts by synthesizing at least one catalyst in the presence of the other, for example, in a core@shell system, such as STM-@MTD-catalyst. The core@shell system, where one catalyst is synthesized in the presence of the other,

is a promising alternative for achieving a desired arrangement of two catalysts. This arrangement has been found to increase DME selectivity significantly, as methanol formed at the core has to diffuse through the shell with dehydration functionality. It should be noted that the hybrid bed, hybrid particle, and core@shell particle concepts described for particulate systems are also applied to planar counterparts, resulting in bifunctional wall coatings. [142, 183].

2.2.6 Synthesis Methods and Performance of Advanced Bifunctional Catalyst Systems

While physically mixing and pelletizing a combination of the two catalysts on the reactor or particle level is relatively straightforward, producing hybrid catalysts involves considering a wide range of parameters that may impact both the individual catalysts and the interaction between them. Various techniques have been investigated, including co-precipitation, impregnation, coprecipitation-sedimentation, sol-gel, sol-gel impregnation, and liquid-phase synthesis [184, 185]. More advanced methods, such as colloidal approach [177, 186] and ultrasound-assisted co-precipitation, have been reported for STD synthesis in recent years [187].

The hybrid configuration at the catalyst level holds significant importance as it allows for precise customization of the intimate contact between the active sites responsible for methanol synthesis and methanol dehydration. One potential drawback of the hybrid catalyst configurations is that it may become deactivated during the

reaction due to the proximity of the methanol synthesis catalyst and the acidic sites of the dehydration catalyst. This issue has been observed in various studies, with examples including the migration of Si to a CZA catalyst, pore blockage resulting from the deposition of carbonaceous species, and the sintering of Cu nanoclusters as a result of contact with aluminosilicates. [186, 188–193]. According to Migliori et al. [194], the interaction between metal and acid plays a crucial role in the methanol dehydration process over hybrid CZZ-zeolite (FER and MFI) catalysts. The authors found that the dehydration catalyst exhibited a higher level of deactivation during the reaction, which resulted in a decrease in DME selectivity and the formation of byproducts such as methyl formate and dimethoxymethane. The authors attribute these effects to two factors: (1) the migration of active metal from the methanol synthesis catalyst to the acidic sites of the dehydration catalyst, and (2) sintering, which is promoted by the water produced during the dehydration reaction. To circumvent the issues discussed earlier, the most straightforward approach is to minimize the contact between the active metallic and acidic phases, which can be achieved by using a mixture on the reactor level. However, this also reduces the potential synergistic effect that could be obtained from a bifunctional system, Nevertheless, it has been reported that this approach improves CO_2 conversion in direct DME synthesis [195].

The application of hierarchically structured catalysts has been viewed as a promising method for enhancing catalyst performance in the direct STD reaction. This method achieves the aim of combining the two catalysts involved while minimizing the negative effects

discussed earlier. Both configurations of DME synthesis function in the core and methanol synthesis function in the shell, or vice versa, have been synthesized, characterized, and thoroughly examined [133, 196–199]. Furthermore, to prevent direct contact between the two active phases in the core@shell configuration, an inactive layer can be added [200].

Sánchez-Contador et al. [133] synthesized a bifunctional catalyst with a Cu/ZnO/ZrO_2-core@SAPO11-shell structure. This catalyst exhibited superior CO and CO_2 conversion, as well as DME selectivity, compared to the hybrid reference catalyst formed by physically mixing the individual components. Phienluphon et al. [201] introduced a novel approach called the physical coating method, which eliminates the need for hydrothermal synthesis, to prepare core-shell CZA-SAPO11, and they found improved performance regarding CO conversion and DME selectivity. To create planar bifunctional systems in microstructured reactors, techniques such as wash-coating [142] or screen printing [183] have been proposed.

2.2.7 Modeling of Different Catalyst Configurations

Numerous investigations have focused on examining the impacts of the configuration and design approach in bifunctional catalyst systems, including hybrid beds, pellets, and hierarchical structures, in both particulate and planar applications from a theoretical perspective [183, 202–205].

Through using mathematical modeling, Gufftani et al. [203] concluded from investigations on the active phase distribution at the pellet scale in catalytic reactors that a significant impact of the

different spatial distribution of the active phases on the reactor performance exists. According to the authors, intraparticle diffusion limitations within the catalyst bed result in lower DME yield compared to hybrid systems on the pellet level. However, for the latter system the authors found a more pronounced hotspot formation. This effect in turn was less pronounced in STM-catalyst core@MTD-catalyst shell systems, which showed comparable yields of DME as the hybrid catalyst system. A micro-kinetic model has been proposed by Ateka et al. [205] to explain the DME synthesis process over a CZZ-based core@SAPO11-shell catalyst. This model allows for the quantification of the impact of particle size on the performance of the reaction and predicts that an increase in catalyst particle size up to 4 mm (which is relevant for use in larger-scale fixed bed reactors) has minimal impact on DME yield and CO_2 conversion. Ding et al. [204] employed a one-dimensional heterogeneous model to simulate the reactions and diffusion occurring in a catalyst comprising a CZA based core and a zeolite shell. Their findings revealed that the thickness and activity level of the shell play a crucial role in determining the catalyst's overall performance. Baracchini et al. [183, 202] conducted a comparison between hybrid catalysts and two catalyst configurations: close or medium proximity, and double layer. Through simulation analysis of the investigated catalyst configurations, it was observed that the hybrid system, where the catalysts are in close proximity, achieves significantly higher CO conversions compared to the double layer system. However, the DME selectivity remains comparable between the two configurations. The lower conversion rate observed in the core@shell

system was attributed to the highly intergrown zeolite shell, which creates mass transport limitations while maintaining high selectivity towards DME.

2.3 State of the art of Screen Printing

Part 1.3.6 outlines that the implementation of the planar bifunctional catalyst in microchannels can be achieved through various coating methods, such as wash-coating and screen printing. Coating can be a challenging process for heterogeneously catalyzed reactions. Different techniques have been published for coating various layers, including (photo)-catalytic, photovoltaic, and electrode materials on different substrates. These methods can be divided into two categories: those in which the slurry, suspension or paste preparation and the coating process are separated, and those in which the substance to be coated is directly applied to the substrate. The slurry can be prepared first using shear method [206], ball milling method [207, 208], homogenization method [209] and ultrasonic method [210, 211], and then coated using techniques such as spray coating [212], spin-coating [213], inkjet [214], and screen printing. Screen printing [215] works similarly to the spreading approach but is more adjustable during the loading phase. It is widely used in electronics production, specifically surface-mount device procedures. The loading process for the catalyst is fast and stable, and the layer can be created in a single step. Unlike the spraying process, the paste used in screen printing does not need to be stirred as frequently, but solvent evaporation must be taken into account. For mass production, screen-printing is considered the best approach for loading catalysts due to its speed, stability, and ability to handle

various pastes and contaminants.

However, the quality of the printed layers can be affected by various parameters, including resolution, adherence to the substrate, and thickness. Patterning resolution is determined by the number and materials of the meshes used in the screen-printing process. Figure 2.5 is a summary of various factors that can impact the outcome or success of the printing process. Ink rheology also affects the precision of the edges and whether the pre-patterned area is dispensed. Surface tension and wettability of the printable pastes to the substrate affect the adherence of the printed film, which can be controlled by the solvents and binders used. The mesh number, screen fabric thickness, and paste composition all play a role in the thickness of printed films. Since standardized production processes are used to make displays, there is little room for variation in their attributes. Therefore, research efforts in screen-printed film improvement primarily focus on paste modulation, including active compounds, solvents, binders, and conductive additives. The rheology of the paste is analyzed using two methods: flow curve test and thixotropic test. The flow curve test measures the viscosity and shear rate of a liquid and identifies its yield point. On the other hand, the thixotropic test assesses how a liquid behaves when subjected to a sudden change or stress. According to Lin et al., for screen printing, the viscosity of the paste preferentially should be in the range between 10 and 20 Pa. s at a shear rate of 100 s^{-1} [216]. Somalu et al. claimed a viscosity in the range 15 - 45 Pa. s at the same shear rate as appropriate for the printing, similar ranges were reported in the works of Ried et al. [217] and Sanson et al. [218]. Performing a shear jump experiment can help

identify the thixotropic behavior of a material, where a sudden increase in shear rate is applied to the material. Poor thixotropic behavior is often caused by inadequate particle dispersion in the ink, which can result in low particle network strength and the formation of cracked films after sintering. The shear jump test is crucial as it simulates the printing conditions and provides information on how the material will behave during the printing process. It is important to ensure that the viscosity of the paste is within a suitable range that allows it to move through the printing sieve during the printing process, but also high enough to prevent it from moving when there is no shear stress applied.

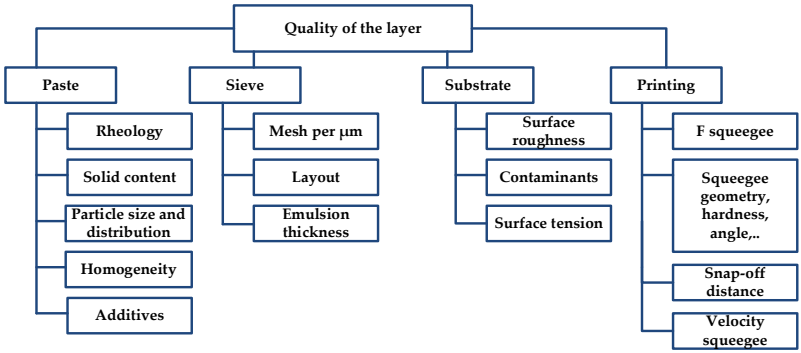

Figure 2-5 Set of screen-printing parameters for the quality of the layer.

A steel mesh or synthetic fiber screen is used in the process of screen printing (shown in Figure 2.6). Applying a design or pattern to the screen prepares it for applying printable materials to the substrate using squeegee pressure through the mesh. As a result, the pattern is transferred to the substrate with a distinct image. The design is

created by coating the regions of the screen that shouldn't transfer the printing materials with an emulsion that is impervious to ink or paste. The printing parameter (Figure 2.5) can have effect on the thickness of the layer [219, 220].

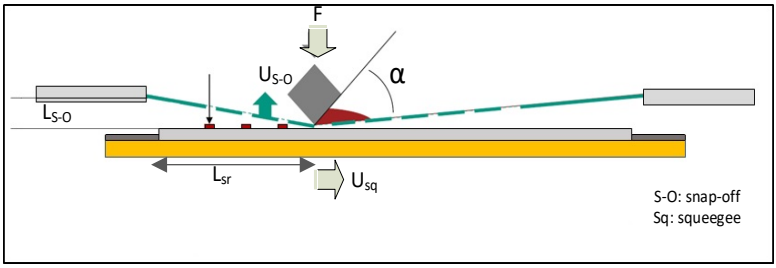

Figure 2-6 The elements that play a role in the process of screen printing.

The squeegee's force F is determined by the interaction of its speed U_{sq}, the paste's viscosity, a squeegee angle function, and a factor f (Q) which depends on the amount of the paste in front of the squeegee (Equations 2.1 and 2.2). Any parameter used in screen printing that causes an increase in hydrostatic paste pressure will result in an increase in the thickness of the deposited layer [221].

$$F = \gamma \times U_{so} \times \frac{2\alpha.sin\alpha}{\alpha^2 - \sin^2 \alpha} \times f(Q) \quad (2.1)$$

$$U_{so} = \frac{U_{sq} \times L_{so}}{L_{sr}} \quad (2.2)$$

3. Experimental Procedure and Catalyst Characterization Method

3.1 Synthesis of CZZ and CZC Catalyst via Flame Spray Pyrolysis

CZZ and CZC catalysts of different molar ratio (Cu: Zn: Zr, Ce) have been prepared by flame spray pyrolysis (FSP). In order to prepare the precursor solution for FSP, metal nitrates were dissolved in ethanol. Copper (II) nitrate tri-hydrate $Cu(NO_3)_2$ -3 H_2O (Carl Roth GmbH, 99%), zinc nitrate hexa-hydrate $Zn(NO_3)_2$ -6 H_2O (Carl Roth GmbH, 99%), Zirconyl (IV) nitrate hydrate (ACROS Organics GmbH, 99.5%) and cerium (III) nitrate hexahydrate (Acros Organics, 99.5%) were used. Precursor solutions of different molar ratio (Cu: Zn: Zr or Ce equal to 6:3:0, 6:3:1, 6:3:2) were prepared, with total molar metal concentration being 0.5 M for all precursor solutions. In general, after adding the metal nitrates to ethanol, the obtained solution was stirred (magnetic stirrer) until the salts were completely dissolved. For FSP, the metal precursor solution was fed to the flame generator (NanoPowderNozzle®, Tethis Spa, Milan) using a syringe pump (PHD Ultra™, Harvard) with a flow rate of 5 ml min^{-1}. The supporting flame was fed by CH_4 (0.5 L min^{-1}) and O_2 (1.9 L min^{-1}). Additional dispersion gas (O_2, 3.5 L min^{-1}, pressure at the nozzle: 2 bar) was fed through the space around the precursor solution nozzle. Sheath gas (O_2, 5 L min^{-1}) was dosed through a sinter-metal ring surrounding the flame in order to maintain a stable flame. The schematic of the FSP is shown in Figure 3.1, and Figure 3.2 shows the description of CTM powder synthesis steps via FSP.

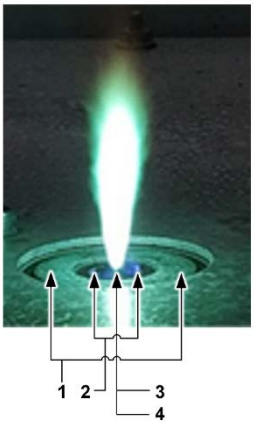

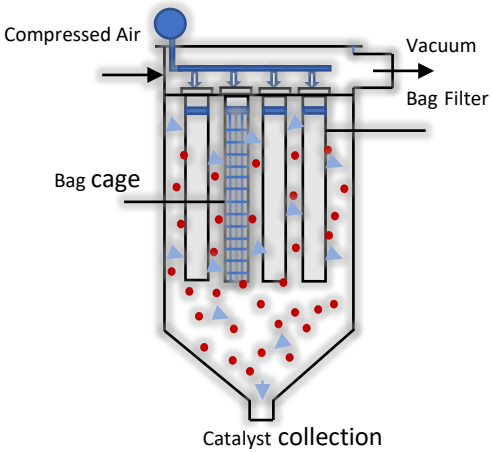

1 Sheet gas (O_2)
2 Supporting flame gas (CH_4, O_2)
3 Dispersion gas (O_2)
4 Precursor solution

Figure 3-1 Illustration of the a) FSP system and b) baghouse filter used for the preparation of the different CZZ and CZC catalysts.

The powder produced was collected semi-continuously via a bag-house filter (Wegner Consulting, Zürich. 4 PTFE filter-bags, pulsation 0.05 s every 5 s). The FSP cylinder was linked to a bag-house filter that contained four polytetrafluoroethylene (PTFE) filters supported by metallic cages, all of which were housed in a stainless-steel casing. The powder-rich air was suctioned to the bag-house filter and the particles were captured at the surface of the filters. The air that had been cleaned of particles was then directed to the hood. To prevent the temperature at the entrance of the housing from exceeding the maximum-operating temperature of 200°C, the synthesis was

stopped when the temperature reached 180°C, and the air vacuum-cleaning continued. Typically, the maximum temperature was reached after one hour of synthesis, which is referred to as the time of synthesis run in this thesis. The resulting product gathered at the bottom of the housing through the use of pulsing. Thanks to the bag-house collection system, there was no restriction on the synthesis time due to the limited capacity of the glass fiber filter. Additionally, there was no need for any treatment, such as sieving, of the product. In the following, powder samples from FSP are denoted CZZ/C-6:3:*x*-(*x*=0, 1, 2).

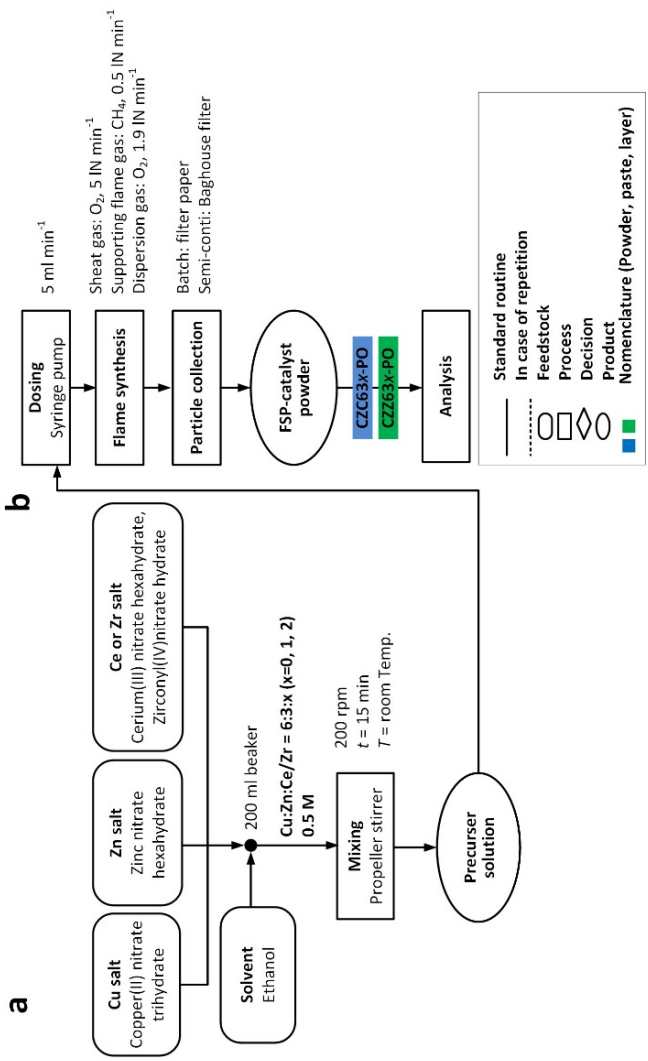

Figure 3-2 The flowchart, nomenclature, and color coding used for the standard CTM (carbon dioxide to methanol) powder synthesis. (a) Preparation of the precursor solution, (b) Details with regard to synthesis condition (dosing of the solution, flow of gas and collection of the powder).

3.2 Optimization of Catalyst Paste and Screen Printing

The different planar catalyst layer configurations considered in this work were prepared by subsequent coating of microstructured foils with the accordant catalysts via screen printing. In particular, stainless steel foils containing 50 semicircular micro-channels created by chemical etching (Ätztechnik Herz GmbH & Co.KG) were coated by the different FSP-CZZ/CZC catalysts and Zeolite HZSM-5 catalyst, respectively. The latter was obtained by calcining as received NH_4-ZSM-5- (SiO_2:Al_2O_3 molar ratio 80:1 (Alfa Aesear GmbH)) at 550 °C for 12 h. According to previous research conducted at IMVT [222] terpinol was first utilized as a solvent while ethyl cellulose was used as a binder. The viscosity of the ethyl cellulose was reported to be 100 cP (5% in toluene/ethanol 80:20) from Sigma Aldrich. However, it was discovered that the terpinol solvent reacts with the zeolites in the MTD catalyst. As a result, water was used as an alternative solvent. Initially, methyl cellulose was used as the binder, since ethyl cellulose is insoluble in water. However, the viscosity of methyl cellulose (ranging from 300-560 cP at 2% concentration in water from Sigma Aldrich) was found to be too low, causing issues with achieving the desired viscosity of the screen-printing paste without altering the proportion of ethyl cellulose in the mixture. Subsequently, 2-hydroxyethyl cellulose was selected as an alternative binder due to its water solubility and higher viscosity compared to methyl cellulose. Nonetheless, working with water-based screen-printing pastes presented challenges due to the rapid evaporation of water in comparison to solvents with higher boiling points. This resulted in changes to the composition and viscosity of the screen-printing

pastes during production and printing, ultimately affecting the reproducibility of the pressure applied. Therefore, for the accordant catalyst pastes, first a suspension consisting of a glycol-based dispersant Decoflux WB110 (Tschimmer und Schwarz, 50-75% 2,2-oxydiethanol, ≤0.01% Bronopol) and 2-Hydroxyethylcellulose (Sigma Aldrich, average molecular weight 1,300,000, viscosity 3,400-5,000 cP (1st % in water)) as binder was prepared by mixing. The suspension was stirred (propeller stirrer) for 20 minutes at room temperature until the catalyst powder was blended homogenously in the solvent. Table 3.1 summarizes the composition of the individual pastes prepared. To further increase the homogeneity, and to break potential agglomerates of the catalyst powder in the suspension, the suspension was further treated using a three-roll-mill (EXAKT 50; EXAKT Technologies, Inc., USA). The three-roll mill's role in homogenizing the screen-printing paste is critical to the production of uniform coatings with consistent layer thickness. Achieving homogeneity in the paste is a crucial step in ensuring the desired outcome. For this, the distance between the rolls as well as the rotation speed was stepwise decreased resp. increased until a homogeneous suspension was achieved, meeting the requirements for further printing (characterized using a rheometer). The two rear rollers, through which the paste was initially conveyed, were set at a distance twice as large as the distance between the two front rollers. Optimal settings for the CTD and MTD screen printing pastes varied due to the influence of several factors on paste viscosity, such as solids content, particle size, particle shape, and surface properties. The CTD screen printing paste was homogenized at a distance of 6/3

and a speed of 8 rpm, while the MTD screen printing paste was homogenized at a distance of 2/1 and a speed of 8 rpm. For the coating, a screen printer (E2, ERKA screen printing technologies GmbH) with an 80-mesh sieve and a mask opening of 100 μm (Koenen GmbH) was used. As previously mentioned, various coating arrangements were suggested for one-stage CTM-MTD integration in micro-channel reactors. For face-to-face patterns, CTM and MTD catalysts were printed independently and then combined using a foil arrangement. In the double-layer pattern, the initial layer that was printed was the CTM catalyst, which was subsequently covered by a layer of the MTD catalyst. To create the hybrid pattern, a paste containing both the CTM and MTD catalysts was formulated. The printing process was repeated multiple times to ensure that there was an adequate amount of catalyst present on the foil as well as desired thickness and ratio between the two catalysts. In general, directly after printing, the accordant layer was dried at 120 °C for 12 h before the next printing step was conducted. In order to remove all of the dispersant and to increase adhesion, coated layers were further heat treated (2 h at 300 °C, 2 K min^{-1} heating/cooling rate). Figure 3.3, provides a depiction of the paste preparation process for CZZ/CZC, zeolite, and hybrid catalysts, along with a detailed explanation. Similarly, Figure 3.4 illustrates the procedure for creating planar catalyst configurations with multiple layers, which is explained in detail in this section. Furthermore, the mechanical stability of the coated foils was evaluated through a drop test that enables the determination of adhesion quality of the coated catalyst by weighing the foils before and after the test. This test was based on a previous

study by Zapf et al. [223] on the adhesion of wash-coats on stainless steel microchannels. In the test, a coated foil was fixed to a metal pole positioned 0.5 meters above a stainless-steel plate. The foil was then dropped onto the plate, achieving a velocity of 3 m/s upon contact. The foil was dropped five times, and the weight loss of the coated foil was calculated to determine the reference value for the mechanical stability of the coated catalyst.

Table 3-1 Composition of prepared pastes for screen printing.

Paste for	**Deco uxwb110**	**2-Hydroxylethyl cellulose**	**Solid content**
CZZ/CZC	84.9-89.9-74.9 wt.%	0.1 wt.%	10-15-25 wt.%
Hybrid (CTM+MTD)	84.9-89.9-74.9 wt.%	0.1 wt.%	10-15-25 wt%
HZSM-5	74.9 wt.%	0.1 wt.%	25 wt.%

The screen-printing parameters for coating of different pastes (Hybrid, Zeolite and CZZ and CZC) also can be found in the Table 3.2.

Table 3-2 The optimized screen-printing parameter use in this research.

Screen printing parameter	
Squeegee speed	30 mm/s
Squeegee pressure	69 bar/N
Snapp off	1 mm
Squeegee angle	45°

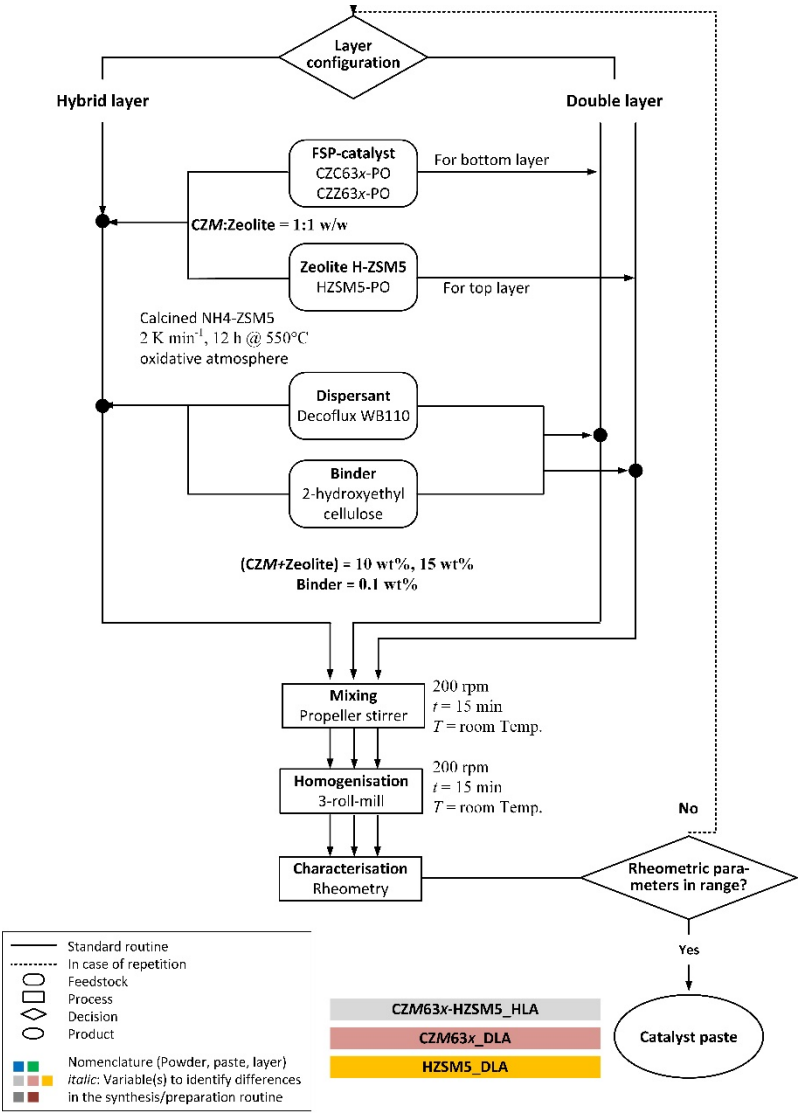

Figure 3-3 Flowchart, nomenclature, and color coding used for paste preparation and screen-printing: Paste optimization procedure.

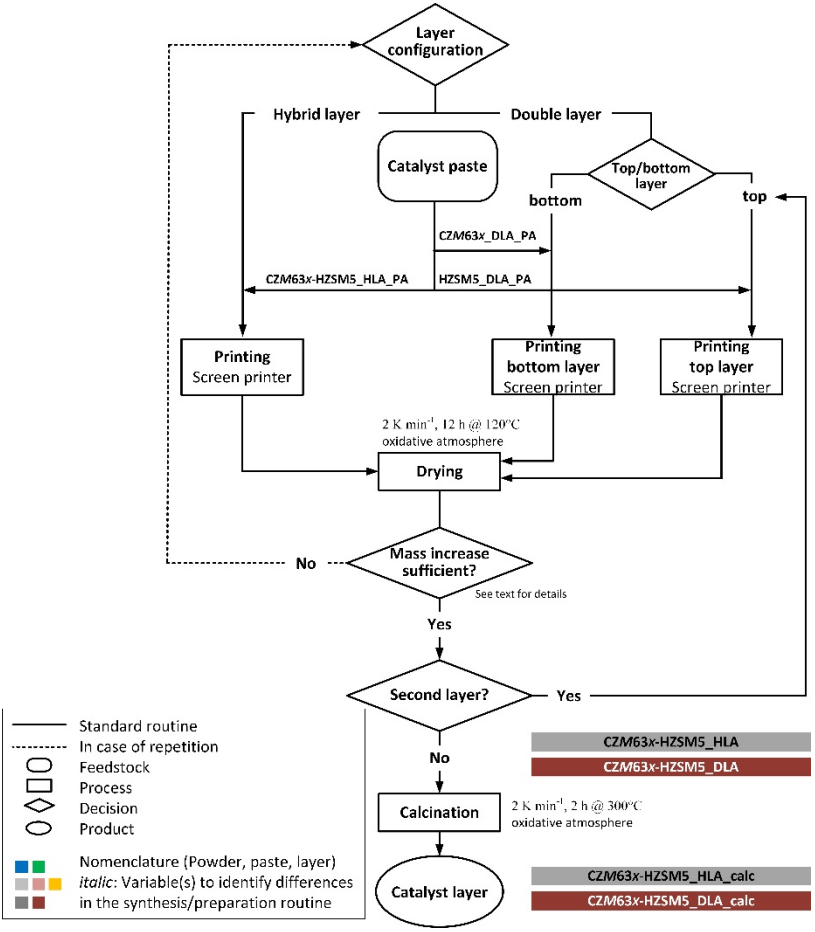

Figure 3-4 Printing process for different planar catalyst layer (hybrid, double layer). For details with regard to times, temperatures, input materials used and post-treatment steps refer to the text.

3.3 Characterization Method

X-ray diffraction (XRD) measurements were carried out using a Bruker D8 Advance (Bruker-AXS, Knielingen, Germany) equipped with a position sensitive detector (PSD) Lynxeye® in θ-θ geometry, variable divergence slit, 2.3° Soller-slits on both sides, at Cu $K_{\alpha 1,2}$-radiation (λ= 0.154018 nm). XRD data were acquired from 5 to 85 °2θ (step width: 0.015 °2θ, 3 s per step, i.e. due to the usage of a PSD the total measurement time per step is 576 s).

Reducibility of the CuO phase of the CZZ catalysts was studied via temperature programmed reduction (TPR) measurements with a ChemBet TPR/TPD Chemisorption Analyzer (Quantachrome Instruments). After outgassing the sample at 250 °C for 2 h, the reduction was performed by ramping the sample with 5 K min^{-1} to 500 °C under a flow of 5% H_2 in Ar. The H_2-consumption was followed using a thermal conductivity detector (TCD).

Nitrogen adsorption and desorption isotherms were measured by a Quantachrome Instruments Nova Station A at 77 K after outgassing the sample at 110 °C for 12 hours. The specific surface area of the samples was computed using the Brunauer-Emmett-Teller (BET) method in the range of 0.05- 0.1 p/p_0. The pore size distribution was derived using the Barrett-Joyner-Halenda (BJH) model (desorption isotherm).

N_2O chemisorption was used to derive the specific Cu surface area. Approximately 1 g of the sample was placed in a fixed bed reactor. The sample was first outgassed (He, 140 °C) before being reduced in-situ (heating up to 240 °C with H_2: He = 1:4, followed by H_2: He = 4:1 for 1 h at 240 °C). After reduction, the sample was cooled down to 60

°C in pure He. N_2O chemisorption was conducted using 827ppm N_2O in He and was continuously followed using an IR gas analyzer (Leybold-Heraeus, Binos). From the overall consumption of N_2O derived from IR measurements, and assuming a stoichiometry of $N_2O + 2Cu \rightarrow Cu_2O + N_2$, the specific copper surface area was calculated following the method of Chinchen et al [224].

In order to determine the quantity and strength of acid centers on a surface using temperature-programmed ammonia desorption (NH_3-TPD), a ChemiSorb 2750 device from Micromeritics® was employed. The measurement process involved introducing approximately 0.25 g or 0.45 g of the catalyst sample to be analyzed into a U-shaped quartz glass reactor (with an internal diameter of 10 mm) along with 0.1 g of quartz glass wool. The sample bed was arranged so that the measuring device's thermocouple was positioned in the middle of the bed. The reactor with the sample was then inserted into the device and flushed with 25 ml min of an inert gas (such as N_2 or He) for an hour before undergoing thermal pretreatment. The sample was heated at a rate of 10 °C per minute to a maximum temperature of 680 °C, which was held for 3 hours before cooling to 40°C. After cooling to 40°C, the sample underwent a flow of 10 vol at this temperature. Next, the reactor and all lines were flushed with an inert gas at a rate of 25 ml min^{-1} for 90 minutes to remove any residual ammonia from the gas phase. Under the same stream of inert gas, the temperature was then gradually increased by 10° C to 200°C, followed by 450°C and 680°C, with each temperature being maintained for 90 minutes. The amount of desorbed ammonia was determined by comparing the area of the signal from the thermal conductivity detector with the

calibration performed using a 1 ml sample loop, which resulted in an area to NH_3 mole ratio of 0.154×10^{-6} mol^{-1}, the amount of desorbed ammonia can be determined.

The primary particle size of the CZZ powder obtained from FSP was determined via transmission electron microscopy (TEM) image analysis. High-angle angular dark-field scanning transmission electron microscopy (HAADF-STEM) imaging combined with energy-dispersive X-ray spectroscopy (EDXS) was further used for semi-quantitative analysis of the chemical composition and the metal dispersion on the nanometer scale. For characterization, a FEI Osiris ChemiSTEM microscope operated at 200 keV, equipped with a Bruker Quantax system (XFlash detector) for EDXS measurements was used. TEM sample preparation was performed by mixing CZZ particles with ultra-pure water and dispensing one droplet of the solution onto a TEM grid using an ultrasonic nebulizer.

Using an Electron Probe Microanalyzer (EPMA, JXA-8530FPlus, JEOL), back-scattered electron (BSE) and wavelength-dispersive spectroscopy (WDS) images were collected for the cross-section of coated channels to analyze the element distribution and thickness of the catalyst layers.

3.4 Direct DME Synthesis

Experiments on the performance of the layer catalyst system prepared in the direct DME synthesis were carried out using an in-house fabricated microreactor made of nickel-chromium-iron alloy (1.4876) (Figure A.5) which can be loaded with a stacking of 150 mm long microstructured foils, Figure A.3 (49 semi-oval channels per foil,

each channel: width = 250 μm, depth = 130 μm) individually coated with the catalyst. In order to achieve a reasonable catalyst loading, the reactor was loaded with a stack of 30 coated foils (Figure A.4). The stack is to some extent compressed when closing the reactor, so that bypass flow can be ruled out. Besides, as will be discussed in more detail in future chapters, catalyst loading per foil and, thus, layer thickness, was quite reproducible, so that a uniform distribution of the flow through each of the 30x49 channels can be assumed. The temperature of the reactor is regulated using 16 electrical heaters situated in the lateral holes. These heaters have a power output of 300 W per unit and are capable of producing a maximum temperature of 750°C. To monitor and regulate the temperature of the reactor, a set of thermocouples with a diameter of 0.5 mm were inserted into the 2.5 mm deep slits of the reactor cover along the flow direction. Before the actual catalyst performance test the reactor was purged with an N_2-flow at 100 °C for 1 hour. After purging, the catalyst was reduced by feeding 4 vol.% H_2 in N_2. Temperature was ramped to 230 °C within 10 h (0.22 K min^{-1}) and held for another 5 h at 230 °C. After this initial reduction phase, the flow was switched to pure H_2 and the temperature was further increased to 250 °C (0.33 K min^{-1}) and kept for 4 h. The actual reaction was conducted at p = 30, 35 and 40 bar(g), 220 °C ≤ T ≤ 280 °C, at constant feed composition of H_2: CO_2 = 3:1 v/v. In general, N_2 (10 vol.%) was co-fed as an internal standard for the GC analytics, in order to account for the gas volume changes occurring during the methanol synthesis and methanol dehydration reactions when calculating conversion and selectivity (see Equations (3.1) -(3.4)). To check the effect of the space velocity on the catalyst

performance, three different total feed flow rates were compared (i.e., 9700, 7400 and 5250 $Nml_{reag}\ h^{-1}\ g_{cat}^{-1}$. Volume flow rate includes reactants, catalyst mass considers the mass of both catalysts of the layer arrangement). A gas chromatograph (GC 7890A, Agilent Technologies) was used to analyze the effluent gas, which included a methanation unit, two columns (HP-Plot Q (30m x 0.530mm x 40.00m) and HP-Molesieve (5m x 0.530mm x 25.00m)), and two detectors (thermal conductivity detector (TCD) and flame ionization detector (FID)). The conversion *X*, selectivity *S* and yield *Y* reported herein were calculated based on the mean value of the last 4 GC measurements of each operating point after reaching stable conditions after 4h time on stream. Flow diagram of the experimental setup for the CTM-MTD integration study is shown in Figure A.6.

$$Z = \frac{y_{N_2}^{0}}{y_{N_2}} = \frac{\dot{N}_{N_2}}{\dot{N}_{N_2,0}} = \frac{\dot{V}_{N_2}}{\dot{V}_{N_2,0}} \tag{3.1}$$

$$X_{CO_2} = 1 - Z \cdot \frac{y_{CO_2}}{y_{CO_2}^{0}} \times 100\% \tag{3.2}$$

$$S_i = \frac{v_i\,(Z \cdot y_i - y_i^{0})}{y_{CO_2}^{0} - Z \cdot y_{CO_2}} \times 100\% \tag{3.3}$$

$$Y_i = X_{CO_2} \cdot S_i \times 100\% \tag{3.4}$$

with *i* being the reaction products MeOH, DME, CH_4 or CO.

4. Characterization Results and Integration in the Micro-reactor

4.1 Physical Properties of FSP CZZ/CZC- Powder Catalysts

The XRD patterns of the catalysts with different metal ratios produced by FSP are shown in Figure 4.1 for CZZ-PO and CZC-PO catalysts with different molar ratios. The samples show the typical diffraction peaks of copper oxide, zinc oxide and – if present – zirconium oxide and cerium oxide, respectively.

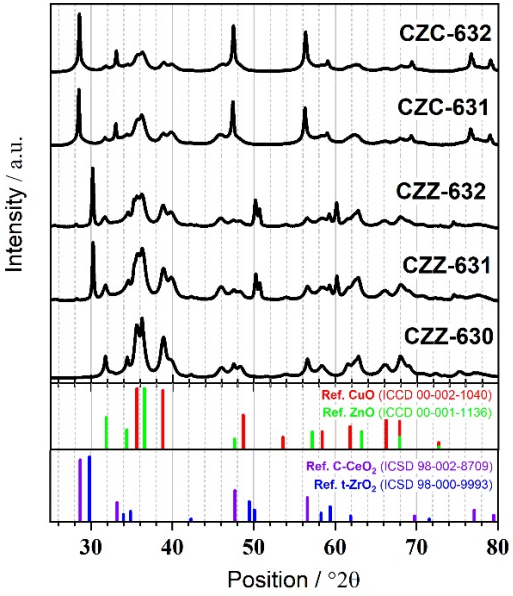

Figure 4-1 XRD patterns of the different CTM samples prepared via FSP with different ratios and accordant references.

The two reflections at 35.56 °2θ and 38.8 °2θ in the XRD pattern are assigned to the (0 0 2) and (1 1 1) plane of tetragonal CuO, respectively [ICCD 00-002-1040], the two peaks at 34.41 °2θ and 36.25 °2θ originate from the (1 1 0) and (0 0 2) lattice planes of wurtzite ZnO [ICCD 00-001-1136]. In addition, the reflection at 30.25 °2θ can be attributed to the (1 0 1) diffraction peak of tetragonal ZrO_2 (t-ZrO_2), reflexes for monoclinic ZrO_2 (m-ZrO_2) were not observed in the diffraction patterns of the CZZ catalysts investigated in the present study. The t-ZrO_2 diffraction peak shows an increase in relative intensity with increasing ZrO_2 content which was also described by Wang et al. (*cf.* samples CZZ-631 vs. CZZ-632) [ICSD 9993, [225]. Witoon et al. found that the catalyst with t-ZrO_2 has a higher catalytic activity than the catalyst with monoclinic ZrO_2 (m-ZrO_2) for CO_2 hydrogenation to methanol [226]. According to Grabowski et al., the oxygen vacancies of t-ZrO_2 are essential for generating the active sites for the reaction [227]. The CuO and ZnO peaks of the samples CZZ-631 and CZZ-632 are less pronounced and wider than the CuO peaks of the CZZ-630 catalysts without any zirconium oxide. This is an indication that the presence of zirconium oxide improves the dispersion of copper and zinc oxide, which can also be seen in the average crystallite size computed using the Scherrer equation using the CuO (1 1 1) reflection (see Table 4.2). Moreover, the reflections at 28.6 °2θ, 47.7 °2θ, 56.20 °2θ correspond to the cubic structure (1 1 1), (2 2 0) and (3 1 1) [ICCD 98-002-8709]. Intensity rise with increasing CeO_2 content (cf. sample as CZC-631 vs.CZC-632). The presence of cerium oxide in CZC-631 and CZC-632 samples leads to weaker and wider CuO and ZnO diffraction peaks

compared to CZ and CZZ catalysts. This suggests that the dispersion of copper and zinc oxide is improved with the addition of cerium oxide, as evidenced by the average crystallite size calculated using the Scherrer equation with the CuO (111) reflection in Table 4.2. Additionally, it can be inferred that cerium oxide is more effective than zirconium oxide because it has a higher surface area, providing more active sites for copper and zinc deposition, and promoting greater interaction between the metals and the oxide support. This ultimately leads to better metal dispersion. With an increase in the Zr and Ce contents from 0 to 10% mol% in the FSP synthesis mixture (CZ-630 vs. CZZ-631 and CZC-631), the average size of the CuO crystallites slightly decreased from 14.3 nm to 10.6 nm and 7.63 nm, respectively. However, increasing the Zr content from 10 mol% to 18.18 mol% in the FSP synthesis mixture did not have an effect on crystallite size. Additionally, the increase in Ce amount (10% to 18.18%) did not enhance the dispersion of CuO as the crystal size of CuO increased by a factor of 1.09. However, the results suggest that adding appropriate amounts of Ce and Zr can impede the growth of CuO crystals, leading to smaller CuO crystallites and improved dispersion of the catalysts [228].

To catalyze methanol synthesis, copper oxide needs to be reduced to metallic copper. Consequently, the CZZ catalysts' reducibility was investigated via TPR. The accordant TPR profiles are shown in Figure 4.2.

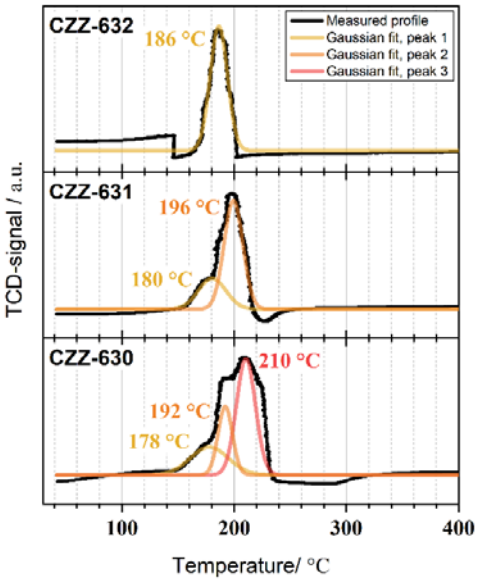

Figure 4-2 TPR profiles of the different CZZ and CZC samples prepared via FSP. Solid line: TCD-signal measured, dashed lines: peak fitting (Gaussian). For reduction range and peak position see Table 4.1.

The different reduction peaks are resulting from the reduction of solely copper oxides occurring in different stages as ZrO_2 and ZnO are not reducible within the temperature range investigated (100–450 °C) [229]. The shoulders of the peaks can be assigned to the reduction process of first Cu^{2+} to Cu^{1+} and then further to metallic copper Cu^0. After deconvolution of the profile (Gaussian peak fitting, see Table 4.1), each sample shows at least two reduction peaks (T_{red}) related to Cu^{2+} reduction. The reduction of well distributed small CuO clusters (lower temperature, *cf.* Peak 1 in Table 4.1), which is ascribed to the one at lower temperature (approx. 180 °C), is followed

by the reduction of more bulky CuO [230–232]. CZZ-630 shows an additional peak (higher temperature, *cf.* Peak 3 in Table 4.1) which is related to the reduction of larger clusters (see also TEM, below) at higher reduction temperature resp. after longer reduction time compared to the smaller clusters. By comparing CZZ-630, CZZ-631 and CZZ-632, the addition of ZrO_2 to the CuO-ZnO material enhances copper oxide reducibility and lowers the main reduction temperature from 210 °C to 186 °C (*cf.* Peak 1 in Table 4.1) being well below the reduction temperature of standard bulk CuO (ca. 280 °C) [233].

Table 4-1 Reduction range and peak temperatures of the CZZ samples prepared via FSP.

Sample	**$T_{red.,range}$/°C**	**$T_{red.,max}$/ °C**	**TPR peak position (Temperature / °C)**		
			Peak 1	**Peak 2**	**Peak 3**
CZZ-630	142-235	210	178	192	210
CZZ-631	115-216	196	180	196	-
CZZ-632	148-202	186	186	-	-
CZC-631	119-165	167	112	167	
CZC-632	117-177	172	140	174	

The TPR results are in good agreement with the XRD results: With increasing ZrO_2 and CeO_2 content, the reduction profile shifts to lower temperatures since the crystallite size of CuO decreases when adding zirconium/cerium to the synthesis via FSP. Similar reduction temperatures have been reported in literature by Witoon et al., who measured $T_{red.}$ in the range of 180-260 °C for a CZ catalyst and showed with changing the CZZ catalyst composition and addition of Zr from 20 to 40 mol% that the reduction temperature was decreased from 226 °C to 206 °C [229]. Kriprasertkul et al. measured $T_{red.}$ in the range of 150 – 360 °C for different catalysts (CZZ, CZ, CZZA and CZA). The reduction temperature of the CZZ catalyst was lower in comparison to the other catalysts tested. The authors conclude that the addition of ZrO_2 causes a reduction of CuO at lower temperature because it assists in reducing the size of the CuO crystallites, while the addition of Al_2O_3 results in an increase in CuO crystallite size and, thus, higher reduction temperature [234]. The main reduction temperature decreased from 210°C to 167°C and 174°C for CZC-631 and CZC-632, respectively (Figure 4.3). This is much below the reduction temperature of standard bulk CuO [230]. It is also possible to draw the conclusion that because the CZ catalyst has a higher Cu loading (66.7%), the reduction peak has shifted to a higher temperature because the Cu particles are larger than that for CZC/CZZ catalysts, which is also in good agreement with the TEM and XRD results. Zhu et al. also, through comparison of the Cu (45)/ZnO-CeO_2 and Cu (5)/ZnO-CeO_2, found that higher amount of Cu caused higher reduction temperature [235].

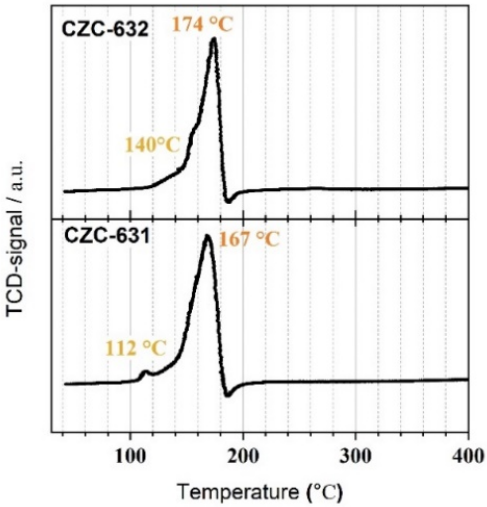

Figure 4-3 TPR profiles of the different CZC with different ratios samples prepared via FSP.

The physicochemical properties of the synthesized catalysts with different ratios of copper, zinc and zirconium/cerium are summarized in Table 4.2. It can be seen that the binary CZ catalyst possesses the lowest BET surface area of 41.65 $m^2 g^{-1}$. By addition of ZrO_2/CeO_2 as a structural promoter (CZZ/CZC-631, 10 wt % of ZrO_2 and CeO_2 based on FSP precursor solution), the surface area increases to 60.32 $m^2 g^{-1}$ and 72.05 $m^2 g^{-1}$, respectively. Similar BET surface areas have been reported in literature by Angelo et al., who measured 61 $m^2 g^{-1}$ for the CZZ catalyst investigated (19 wt.-% of ZrO_2) [236]. The increase in specific surface area is in accordance with findings from XRD, showing that ZrO_2 and CeO_2 plays a role in CuO nano-

structuring. However, while CuO crystallite size (XRD) and specific surface area (BET) decreased resp. increased with addition of ZrO_2 (CZZ-630, CZZ-631), a further increase of ZrO_2 (CZZ-632) did not have a significant effect on CuO crystal size and surface area. Reduced CeO_2 particle size in the CZC catalyst due to the 4f orbit and Ce structural relaxation will also increase the surface area and concentration of defects such as oxygen vacancies [228]. Moreover, CeO_2 can also produce greater BET surface area than CuO [237]. According to Zhou et al., increased loading of CeO_2 (from 3 to 4 wt%) results in a decrease in surface area, which may be related to the growth of the crystallites as the CeO_2 concentration increases [228]. As the Zr/Ce content increases, the pore diameter decreases, indicating that the addition of Zr/Ce hinders the growth and crystallization of the new phase, leading to smaller metal oxide sizes. Moreover, the incorporation of Zr/Ce into the space of the new phase (Cu-Zn) is suggested reduction in pore volume (see Table 4.2) [229]. In contrast to the specific surface area determined by BET, CZZ-632 and CZC-632 shows a significantly smaller value of the specific copper surface area S_{Cu} (from N_2O chemisorption, see Table 4.2) as compared to CZZ-632 and CZC-631, while CuO crystallite sizes are comparable (XRD). Witoon et al. also found that with increasing the percentage of Zr from 30 mol% to 40 mol%, there is no significant effect on the crystal size which was about 7 and 6.8 nm, respectively, in their case however, the copper surface area differs by a factor of 1.6 [229]. This indicates that a high BET surface area resp. small crystallite size is not necessarily related to a high specific copper surface area but is dependent upon how metallic Cu interacts with

the support [238]. As it can be concluded from the results presented, an increase of the Zr/Ce content in CZZ/CZC material does not only have a significant effect on the specific surface area, crystal size and T_{red} but at some point seems to have a negative effect on the specific copper surface area which is an important factor for the catalytic activity as reported ,e.g., in Refs [33, 239, 240].

Table 4-2 Chemical composition, specific surface area (SBET), specific pore volume (vpore) and CuO crystallite size (D_{CuO}) and Cu surface area (S_{Cu}).

Sample	**[a]Metal Composition / mol%**			**[b]S_{BET} / m^2g^{-1}**	**[c]V_{pore} /cm^3g^{-1}**	**[d]D_{CuO} / nm**	**[e]S_{Cu} / m^2g^{-1}**
	Cu	**Zn**	**Zr /Ce**				
CZZ-630	66.7	33.3	0	41.65	0.2	14.3	17.59
CZZ-631	60	30	10	60.32	0.159	10.6	18.93
CZZ-632	54.54	27.28	18.18	63.61	0.09	10.7	10.88
CZC-631	60	30	10	72.05	0.158	7.63	25.46
CZC-632	54.54	27.28	18.18	76.85	0.17	8.37	12.06

(a) As used in precursor solution
(b) N_2 sorption isotherm (BET)
(c) From N_2 sorption isotherm at p/p_0= 0.99
(d) Via Scherrer equation from diffraction peak at 38.8 °2Θ
(e) From N_2O chemisorption

CZZ-63*x*-PO particle morphology and elemental distribution was investigated using HAADF-STEM/EDXS. From TE-micrographs (Figure 4.4.a) it can be concluded that all samples contain discrete, separated CuO and ZnO. According to EDXS image analysis (Figure 4.4.b), both Cu and Zn are distributed homogenously all over the sample and are well dispersed in the nanometer range within the catalyst aggregate: as-synthesized primary nanoparticles are

polygonal in shape with a particle size of around 5 to 20 nm. However, Zr is partly also aggregated as larger spherical particles with a size of up to 230 nm. Literature studies on the flame synthesis process of Cu-Zn-alumina (CZA) systems report that Zn aluminate and copper aluminate spinel are formed at high temperature, while the formation of copper or zinc oxides is favorable at lower temperatures [68]. In the present work, spinel formation could not be fully excluded but based on the STEM/EDXS investigations it can be assumed that zirconium oxide forms prior to zinc and copper species and aggregates to larger clusters. Such observation was also reported by Lee et al. [65] and Jensen et al. [68] for CZA-systems. In other words, low diffusion rate throughout the FSP-process can lead to solidification of zirconium oxide and thereby to the formation of the separated larger particles observed. However, based on the analyses discussed above, small copper and zinc oxide clusters are predominantly separated from the accumulated larger clusters of zirconia. Moreover, in the sample CZZ-632 a bigger Cu enrichment can be seen which causes the reduction of the specific copper surface area. The average particle size of the CZ catalyst is also demonstrated to be significantly greater than that of the Ce-containing, which is consistent with the specific surface area. Additionally, all three components (Cu, Zn, and Ce) are homogenously and finely distributed, according to the EDXS image analysis (Figure 4.4b). It is obvious that CeO_2 in the support can promote Cu dispersion. There is no doubt that CeO_2 in the support can enhance Cu dispersion. However, it is evident that a higher percentage of Ce (CZC-632) results in a greater Cu enrichment, an increase in the size of copper

oxide, which is consistent with XRD, and a decrease in the copper surface area (Table 4.2). In conclusion, it has been shown that FSP is a viable approach for creating catalysts with scattered Cu particles supported on a mixture of CeO_2 and ZnO oxide, and that Ce can be advantageous for dispersed Cu when added in the appropriate amounts.

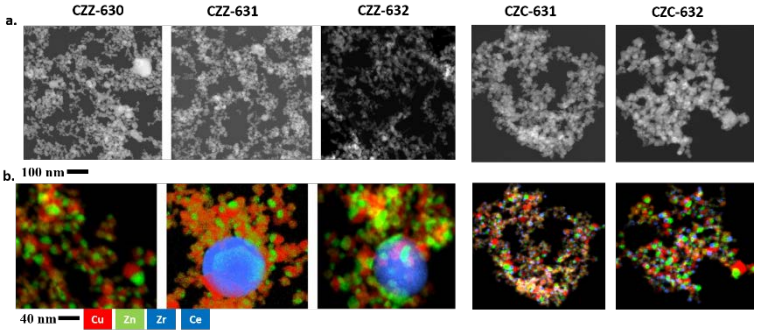

Figure 4-4 TEM-images (top row) and EDXS maps (bottom line) of the different CZZ materials synthesized via FSP: CZZ-630 (a), CZZ-631 (b) and CZZ-632 (c).

In conclusion, the physico-chemical characterization of the CZZ/CZC catalysts of different molar ratios synthesized via FSP investigated in this study revealed that composition of Cu:Zn:Zr= 6:3:1 and Cu:Zn:Ce= 6:3:1 (i.e., sample CZZ-631 and CZC-631) results in a catalyst material of the most promising combination of specific surface area (BET and S_{Cu}), CuO crystallite size, particle size homogeneity within the sample and reduction behavior. Therefore, in order to assess the potential of a different configuration of catalyst layer system for direct DME-synthesis, CZZ-631 and CZC-631 were chosen for further investigations.

4.2 Characterization of Screen-Printing Pastes

The hybrid planar catalyst system (CZZ/C-Z-HLA) and structured double layer configuration (CZZ/C- Z-DLA) and face to face (CZZ/C-Z-FLA) were prepared using the microchannel coating method with pastes whose compositions are outlined in Table 3.1 and described in Section 3.2. The success of the screen-printing process used for coating is highly dependent on the rheology and thixotropy of the pastes, as discussed in Sections 2.3 and 3.2. The pastes' rheology and thixotropy properties were characterized for all preparations.

4.2.1 Rheology

The rheology and thixotropy of the pastes applied for screen printing are both important factors for achieving homogeneous layers. The relevant characteristics of the pastes were evaluated by measurements using a rotating disk rheometer (Rheostress 1, Thermo Scientific, Haake, cone geometry C60/1° (diameter 60 mm, angle 1°)) at 25 °C). The paste was placed between the holder and the cone with a side angle of 1°. The flow plot was obtained running a shear stress linear ramp from 0.1 Pa up to 1200 Pa, and the resulting shear rate was recorded. The thixotropic behavior was determined by measuring the viscosity of the pastes at different shear rates applied as a step function ($0.1\ s^{-1} \rightarrow 100\ s^{-1} \rightarrow 0.1\ s^{-1}$). Figure 4.5.a, 4.6.a show the shear stress and viscosity of the individual pastes prepared as a function of the shear rate. Both pastes show a shear thinning behavior. Besides, starting from a share rate of approx. $100\ s^{-1}$, in comparison to the zeolite paste, the CZZ pastes show lower shear stress and higher viscosity values, respectively. Somalu et al. also

mentioned that it is essential to consider the paste behavior in the shear rate regime occurring throughout the screen-printing process [241]. In order for a successful screen-printing process, the pastes applied should exhibit low viscosity at high shear rate (actual printing) and vice versa (distribution of the paste on the sieve) [216]. Thus, a 3-interval thixotropic test was conducted to mimic the conditions during screen printing. In particular, the shear rate was originally fixed at 0.1 s^{-1} (first 240 s) and then abruptly increased to 100 s^{-1} (next 45 s) before being reduced to 0.1 s^{-1} again (for the last 200 s). Figure 4.5.b and 4.6.b shows the results of the thixotropic test for each of the pastes considered. While the zeolite paste follows the typical shear thinning and thixotropic behavior, the CZZ/CZC pastes show a strong increase in viscosity when stress is initially applied – however, once the CZZ-paste is equilibrated after initial stress, it likewise shows shear thinning with only minor thixotropic behavior (see second set of the 3-interval test). Again, at low shear rate, the CZZ/CZC catalyst pastes have a significantly higher viscosity than the zeolite paste. However, when the shear rate is increased (mimicking the actual printing), the viscosities of the pastes are similar and – even if not exactly within the range suggested in literature (see above) – have been shown to result in satisfactory layers and, thus, can both be considered as suitable for coating using screen printing. Additionally, as it is mentioned in Section 3.2, solid content, particle size, surface area of the particle and also binder content have effects on the quality of the layer. The amount of binder used in a paste for screen-printing has a significant impact on its rheological properties. Using too much binder can cause the paste to

become excessively sticky, leading to poor printability and reduced quality of the resulting catalyst layer. Conversely, using too little binder can result in cracking of the green films during drying due to weakened particle networks within the ink. Therefore, achieving an optimal balance between solid and binder content is crucial to controlling the ink's rheology [241]. Consequently, the amount of binder was maintained at a constant level, which was found to be adequate in previous IMVT research to produce high-quality layers and the amount of catalyst was optimized [242]. Furthermore, when preparing screen-printing pastes using powders of a nano-sized scale, the resultant paste may have a low solid content owing to the high surface area of the powders. This, in turn, may enhance inter-particle interaction within the powder, leading to greater viscosity and viscoelastic properties in the inks, even at low solid contents. These effects are more pronounced in comparison to commercial powders that have a lower surface area (less than 10 m^2/g). As a result, as it can be seen in Figure 4.5a the CZZ-25%-PA and CZC-15%-PA yield stress and viscosity of the catalysts are even higher than the limited range of printability and it is the reason that with 15% of the CZC catalyst the viscosity is higher, however, for CZZ 15% catalyst the viscosity is in the range. The viscosity of the catalysts, CZZ-25%-PA and CZC-15%-PA, as illustrated in Figure 4.5a, exceed the acceptable range of printability. Additionally, it can be observed that the yield stress of both pastes exceeded 1000 Pa, but decreased as the amount of catalyst was reduced. It was imperative to lower the yield stress values in order to obtain a paste that is suitable for printing. Notably, the viscosity of the CZC catalyst at 15% is higher compared

to that of the CZZ catalyst at the same percentage. This is the likely cause of the higher viscosity for CZZ-25%-PA, whereas the viscosity is within the acceptable range for the CZZ 15% catalyst.

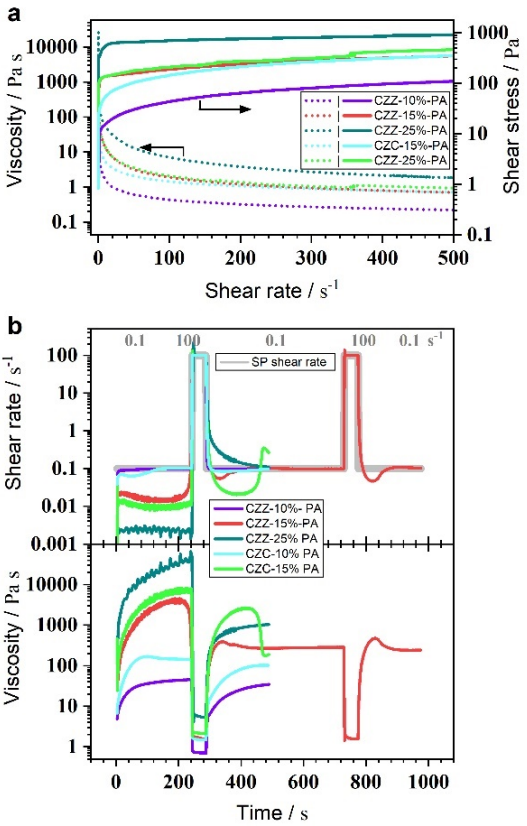

Figure 4-5 Rheological properties of the CTM-pastes applied: (a) Shear stress and viscosity vs. shear rate (b) 3 intervals thixotropy test.

However, the particle size of the commercial zeolite was not in the range, therefore, the viscosity of the HZM5-25%-PA resulted in lower viscosity in comparison with CZZ/CZC. Despite having a higher

surface area, the HZSM-5-25%-PA (Figure 4.6) catalyst had a lower viscosity than CZZ/CZC due to the fact that the particle size of the commercial zeolite was not within the nano-size range. This implies that the preparation of the paste and the quantity of its components can be extrapolated when the starting material has comparable structural properties. This finding is consistent with Somalu et al.'s research [241], which found that the paste viscosity is determined not only by the loading of the solvent and binder, but also by the powder's surface area to be printed. Sun and Kirsch observed that a zeolitic hydrocracking catalyst (Pt-ZSM-5) displayed thixotropic behavior, where the viscosity returned to a similar level within 50 seconds of applying a shear rate of 100 s^{-1} [242, 243]. This finding could potentially enhance the success of the screen-printing process. Although CZZ-10%-PA was within the acceptable range, CZZ-15%-PA was selected for CZZ-Z-DLA layer and CZZ-Z-FLA to increase the amount of catalyst used during printing, minimize the number of printing cycles required to achieve the desired catalyst thickness and weight, and prevent surface layer cracking due to lower solid content.

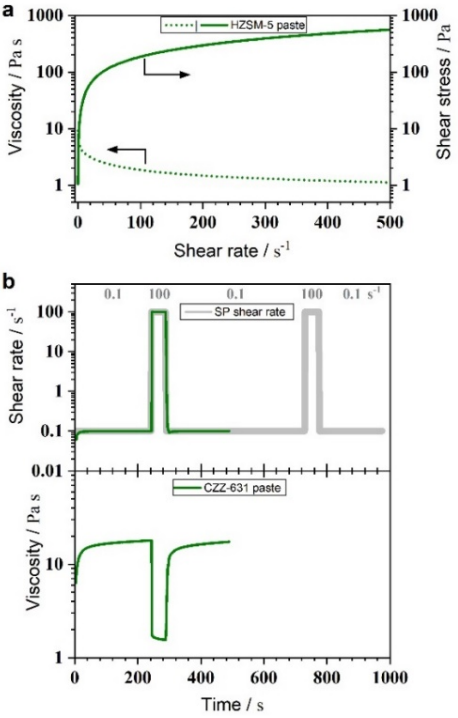

Figure 4-6 Rheological properties of the MTD paste applied: (a) Shear stress and viscosity vs. shear rate (b) 3 intervals thixotropy test.

Both hybrid catalysts (CZZ-Z-HLA and CZC-Z-HLA) were also subject to rheological measurements. The behavior of the hybrid catalysts displayed a comparable pattern, as depicted in Figure 4.7. Consequently, 15% hybrid catalysts were chosen for the printing process. The 25% paste exhibited viscosity and shear rate values that were outside the acceptable range for printing, while the 10% paste contained a lower amount of catalyst, leading to an increased number of printing instances.

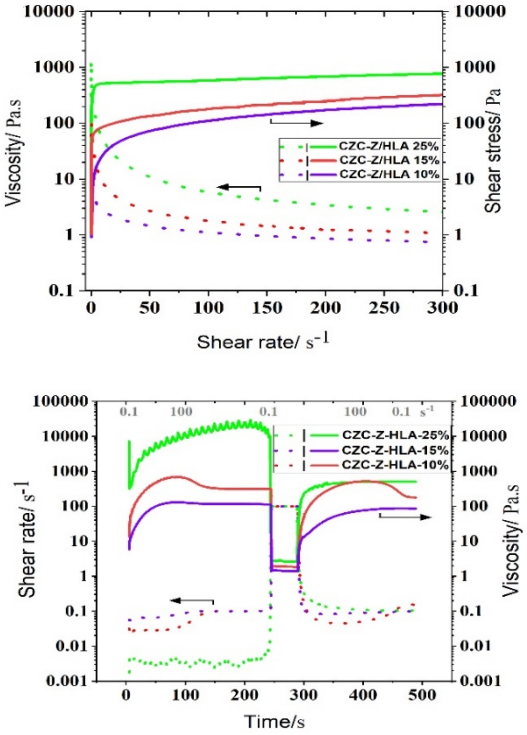

Figure 4-7 Rheological properties of hybrid pastes applied: (a) Shear stress and viscosity vs. shear rate (b) 3 intervals thixotropy test.

Previous simulation studies conducted at IMVT investigated the impact of the catalyst ratio on different configurations through 3D-crystallite pore network model (3D-CPNM) which allows for an evaluation of the influence of the zeolite properties like (porosity, layer thickness). The CO conversion and DME yield as a function of CZA/zeolite weight ratio was investigated. The studies revealed that the maximum carbon monoxide conversion in the μ-CR reactor for

the three configurations (hybrid medium and close proximity, and double layer) was maximum when the ratio of the catalysts was 40%wt approximately. Moreover, it was found that for the coated system, the maximum yield could be achieved at around 40% weight percent for the double-layer configuration and 50% weight percent for the both hybrid-layer configuration. Therefore, a 1:1 ratio of the two catalysts was used in various planar configurations to compare the results [222].

4.2.2 Calcination of Coated Foils

Calcination of the coated foils was required to eliminate the solvent, binder, and paste constituents. To confirm that the suspending agent and binder used in the production of the screen-printing paste would decompose during calcination at 300°C, a Thermal gravimetric analysis (TGA) was conducted. The TGA analysis was performed on a screen-printing paste containing 15 wt% CZZ and hybrid (CZZ- Z-HLA), 0.1 wt% 2-hydroxyethyl cellulose, and 84.9 wt% Decoflux WB 110. The measurement first was conducted using a TGA instrument at IFG of the KIT, where the sample was heated in air to 400°C with a heating rate of 2°C/min. Initially, the sample was heated at a uniform heating rate to a temperature of 100°C, followed by a dwell time of 30 minutes to ensure complete removal of any residual moisture. Subsequently, the temperature was gradually increased to 300°C followed by a hold time of 2 hours, which served as the (calcination time and temperature). Due to the well-known impacts on Cu-based systems at temperatures over 300°C, extra caution was required. Additionally, previous studies in literature have suggested

that the abrupt exposure of the coated layers to elevated temperatures could potentially cause harm to the integrity of the layer. The mass loss of the sample was recorded, and the absolute of the sample mass and relative mass loss against the temperature is presented in Figure 4.8. According to the data presented in the figure, the mass losses observed at various temperatures were ascribed to the constituent components of the screen-printing paste. Notably, the proportion of Bronopol present in the paste was too minuscule to be detected. However, the residual mass, constituting around 15% and 17% of the original mass for hybrid (Figure A.1) and CZZ catalyst, respectively, was roughly equivalent to the mass fraction of CZZ/CZZ-Z-HLA present in the paste. This suggests that the complete decomposition of the suspending agent and binder can be achieved by calcination at a temperature of 300°C as no additional loss of mass was observed beyond 300°C for all samples. Thus, this temperature was selected for the calcination treatment.

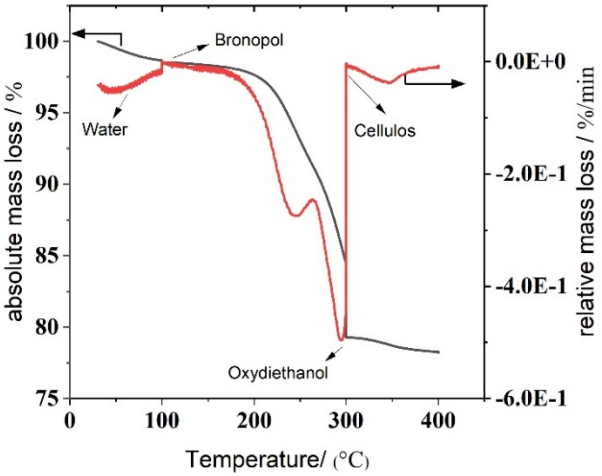

Figure 4-8 Plot of absolute CZZ-15%-PA sample mass versus temperature obtained from TGA analysis of screen-printing paste. The experiment was conducted in air at a heating rate of 2 °C/min, with a hold time of 2 hours at 300°C, and a maximum temperature of 400°C.

4.2.3 Mechanical stability of coated foils

The evaluation of mechanical stability, as described in section 3.2, involved conducting drop tests. The outcomes of the drop test, as depicted in Table 4.3, reveal the weight loss of the coated catalysts CZC10%, CZC-Z-10%-HLA, and CZZ-Z-15%-HLA to be low, with values of only 0%, 4.4%, and 5.8% respectively. Weight loss below 5% indicates excellent adhesion and remarkable mechanical stability of the coated catalysts. These findings demonstrate the successful coating procedure and the optimal composition of the paste, as evidenced by the results presented in Table 3.1.

Table 4-3: Mechanical stability result for three different catalyst after calcination through drop test.

Sample	M_{cat} (g)	M_{before} (g)	M_{after} (g)	M_{diff} (g)	M_{diff} (%)
CZC-10%-PA	0.019	7.4975	7.4975	0	0
CZC-Z-10%-HLA	0.016	7.5858	7.5851	0.0007	4.4
CZZ-Z-15%-HLA	0.026	7.6319	7.6304	0.0015	5.8

4.2.4 Physical Properties of CTM and MTD Pastes

In this section, two distinct copper-based catalyst pastes (CZZ and CZC) were utilized to coat surfaces, both intended for use in methanol synthesis and direct DME synthesis through CZZ/C-Z-DLA and CZZ/C-Z-FLA layers. The physicochemical characteristics of the calcined CZZ, CZC, and zeolite were compared to FSP-powder (see Section 4.1) and the morphology of the resulting layer from CZZ for methanol is presented. Moreover, as previously mentioned, various coating designs were suggested for integrating one-stage CTM-MTD in micro-channel reactors. To create face-to-face patterns, CTM and MTD catalysts were separately printed and then merged through the foil configuration. On the other hand, the dual-layer pattern involved the initial printing of CTM catalyst and subsequently covering it with a layer of CTD catalyst. The morphology of each configuration will also be discussed.

Figure 4.9a displays the XRD patterns of the coated CTM catalysts after calcination which reveals the presence of distinct and well-defined diffraction peaks that correspond to CuO and ZnO, as compared to the powder samples. This observation suggests the

existence of crystalline species with larger crystallite sizes within the paste samples. By applying the Scherrer equation using CuO [111], it was observed from the XRD analysis that the CuO crystallite size of CZZ-15%-PA_c and CZC-10%-PA-c increased after calcination, with a size range of 12.9 nm and 10.4 nm, respectively. The trend observed in the study indicates that the crystallite sizes of both CuO and ZnO increase in the order CZC < CZZ. The results imply that CeO_2 can be considered as better promoter in comparison with ZrO_2, as it facilitates greater dispersion of CuO and ZnO [244]. In addition, the disappearance of diffraction peaks at 39.82° and 45.79° was observed after the calcination process for both catalyst which can be assigned to CuO. The thermal treatment resulted in a significant decrease in the BET surface area of CZC-PA-C and CZZ-PA-C, from their respective initial values of 72.05 and 60.3 $m^2 g^{-1}$ to 28.36 and 18.49 $m^2 g^{-1}$, coupled with the reduction in the pore volume. This can be attributed to the rise in crystallinity and the clustering of the nanoparticles CuO, ZnO, and ZrO_2 as seen by the XRD data mentioned above. Furthermore, a comparison of CZZ-PA-C and CZC-PA-C revealed a reduction of 78.16% and 60.33% in copper surface area, respectively. These findings suggest that cerium is more effective in stabilizing the copper in the catalyst [245, 246]. The comparison of zeolite powder and paste calcined samples yielded no observable differences. Therefore, it can be inferred that the process of making paste using a three-roll mill and also calcination (comparison of dry and calcined sample) did not cause any adverse effects or crystal breakage or physical properties of zeolite as can be seen in Table A.1.

According to the Figure 4.9b, the reduction of the calcined paste CZZ-PA commences at a temperature of 180°C and culminates at 300°C, with a maximum peak at 251°C. However, the CZC calcined paste exhibited a reduction in temperature at a lower temperature, [244] with a maximum peak at 229°C, which is consistent with the BET and XRD characterizations, and concluded at 261°C which shows easier reducibility in comparison to CZZ-PA.

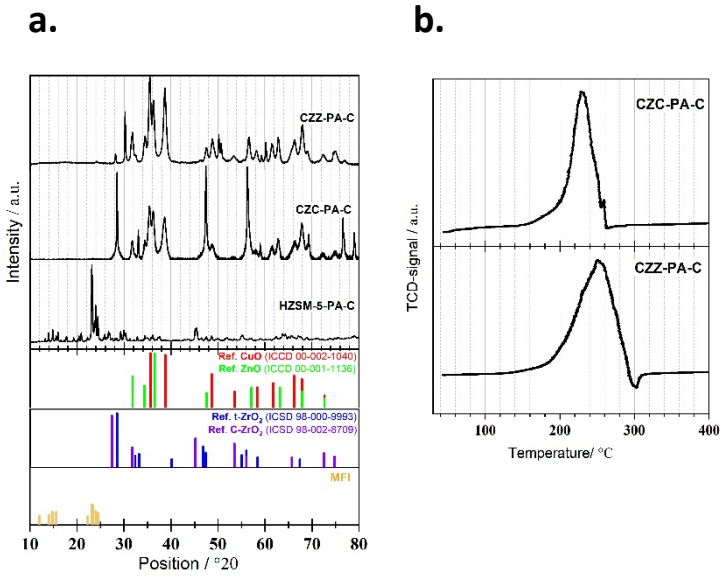

Figure 4-9 (a) XRD and (b) TPR profile patterns of the prepared CZZ-CZC and HZSM-5 calcined paste samples and accordant references.

4.2.5 Physical Properties of Hybrid Pastes

This section focuses on discussing the characterization of the hybrid catalyst paste for hybrid planar configuration. As it is mentioned, the hybrid catalysts were mixed of CTM (CZZ or CZC) and MTD (HZSM-5) with a rough ratio of 50/50 wt/wt. Table 4.5 provides an overview of the physicochemical properties of the hybrid systems that were prepared, including information on composition, texture, and metallic properties.

Table 4-4 Physico-chemical characteristic of the calcined prepared hybrid catalyst

Sample	S_{BET} / m^2g^{-1}	V_{micro} /cm^3g^{-1}	$^{(e)}S_{Cu}$ / m^2g^{-1}
CZZ-Z-HLA-C	211.78	0.059	2.5
CZC-Z-HLA-C	214.23	0.061	6.63

Table 4.4 displays a noteworthy reduction of approximately 43% in micropore volume compared to the bare zeolite. The hybrid catalysts exhibit a decline in micro-porosity, which implies that the mixed oxides were uniformly distributed on the external surface of the zeolites during the paste preparation process which also can be confirmed by TEM (Figure 4.11). Thus, given the remaining microporosity of each catalyst, it is suggested that the effectiveness of active sites for the one-step hydrogenation of CO_2 to DME should primarily be investigated at the mesopore level. Bonura et al. synthesized a CZZ hybrid catalyst system via co-precipitation using various types of zeolite. They determined that the textural properties

of the hybrids are notably influenced by the type of zeolite utilized, resulting in a distinct reduction of surface area compared to the "parent" zeolites [189, 247]. Figure 4.10 a display the XRD patterns of the hybrid pastes following calcination. By comparing the pattern of the sample to the references, it is confirmed that both the MFI and the CZZ/C structures are present. The crystallite size of CuO in the CZZ-Z-HLA and CZC-Z-HLA materials was determined to be 14.71 nm and 10.79nm, respectively, using the Scherrer equation based on the CuO [111] reflection at 2θ = 38.8. Furthermore, it can be inferred that CZZ-Z-HLA has a larger crystal size based on the higher intensity of the CuO peak at 2θ = 38.8° compared to the other samples.

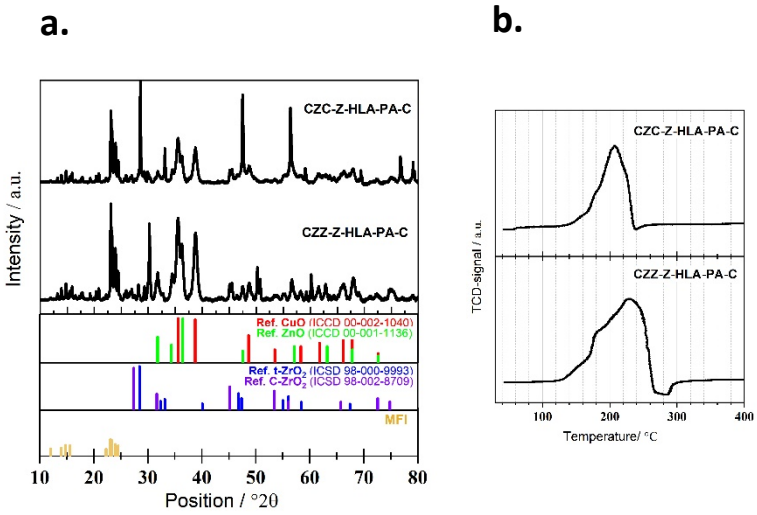

Figure 4-10 (a) XRD and (b) TPR profile patterns of the prepared hybrid catalyst (CZZ-Z-HLA and CZC-Z-HLA) calcined paste samples and accordant references.

Upon analyzing the reduction pattern of both catalysts (refer to Figure 4.10 b), the TPR profiles exhibit a primary peak below 300°C, which corresponds to the gradual reduction of CuO to metallic copper. However, similar to CZZ-PA and CZC-PA, the reduction temperature of CZC-HZSM-5-HLA is lower and it starts from 146°C with a main peak at 206°C. The higher reduction temperature observed in the CZZ hybrid catalyst relative to the CZZ catalyst is possibly attributed to the existence of an extra zeolite phase in the former. This may lead to a more intricate reduction process, culminating in an elevated reduction temperature. Moreover, the way in which the metal-oxide clusters are distributed and interact with the zeolite framework in the hybrid catalyst might also impact the reduction temperature.

Figure 4.11, related to TEM image illustrate the distribution pattern of metal-oxide clusters (consisting of copper, zinc, and zirconia) on the external surface of zeolite. The formation of either smaller or larger agglomerates is observed, resulting in distinct texture, morphology, and catalytic properties. The crucial point is that the preparation procedure promotes a relatively uniform distribution of mixed oxides on the outer zeolite framework, which guarantees intimate surface contact among the phases and suggests minimal limitations in terms of transport phenomena during the reaction for the powder catalyst [189]. However, since we have a layer, the homogeneity of the layer will be discussed in the following sections.

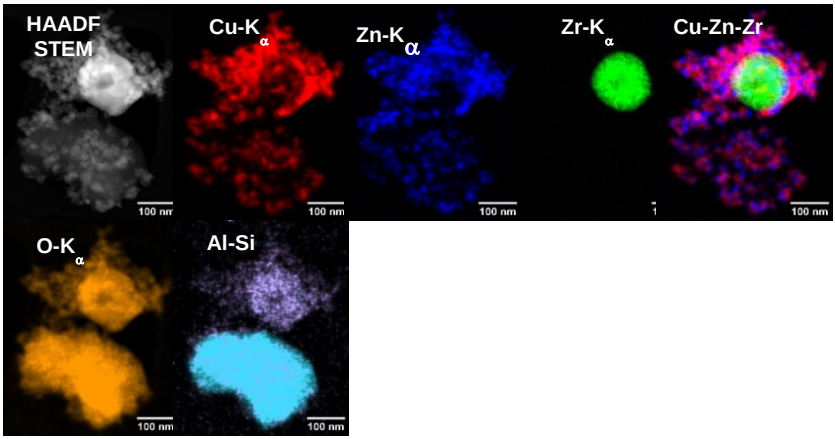

Figure 4-11 TEM-images and EDXS maps of the calcined CZZ-Z-HLA hybrid catalyst after calcination at 300°C.

To perform the CTM only reaction test, two distinct CZ-based pastes, namely CZZ-PA and CZC-PA, were utilized for coating. A comparative analysis of the physico-chemical attributes of the calcined CZZ-PA-C and CZC-PA-C was conducted and detailed in Section 4.2.4. The depiction of the morphology of the final coating layer formed by CZZ-PA-C is illustrated in this section. Since the CZC layer has an identical morphology to that of CZZ-PA-C, in this part, we only present the morphology of the CZZ-PA-C layer. However, the information about the thickness and amount of the CZC-PA-C catalyst will be discussed in this section.

4.3.1. Structural Characterization of CTM Layers

It has been observed in Figure 4.12 that the catalyst layers are evenly distributed within the channel, and their thickness is uniform throughout, so that a uniform distribution of the flow through channels can be assumed. The top view (Figure 4.12a-A) shows that the layer of the catalyst is crack-free. In order to obtain the desired quantity of CZZ-15%-PA-C catalyst, the printing process was carried out three times. However, due to the lower loading of CZC catalyst in the paste (CZC-10%-PA-C), a greater number of printing iterations (5 times) were necessary (See Figure 2.3 for more details). Table 4.6 shows that the printing process is reproducible with respect to the thickness and weight of the catalyst, as evidenced by the example of CZZ-15%-PA-C. Furthermore, Figure 4.12b-A depicts noticeable increase in layer thickness with each successive printing iteration (as indicated in Table 4.5) through the use of colored arrows at the end of each layer. In summary, the total mass of CZZ-15%-PA-C and CZC-10%-PA-C in 30 foils were 1.51g after calcination with a thickness of 16.41 μm and 1.54g with a thickness of approximately 17.01 μm, respectively (Figure 4.12.B).

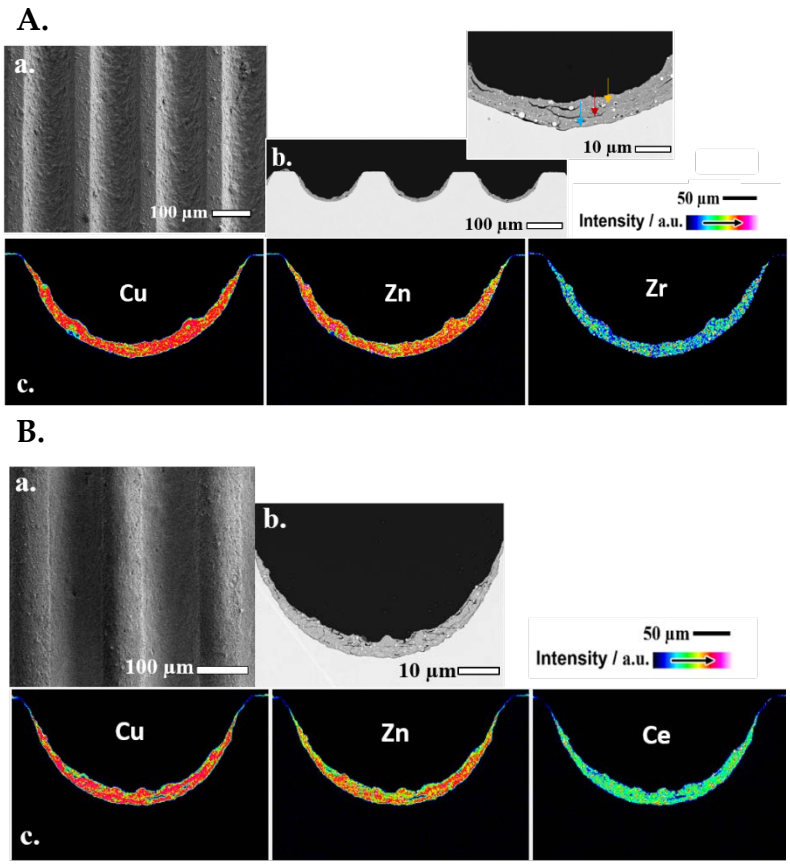

Figure 4-12 (a) SE-micrographs, (b) cross-sectional analysis of the layer via EPMA/BSE and (c) elemental map via EPMA/WDX for A. CZZ layer obtained from the paste CZZ-15%-PA-C and B. CZC layer obtained from the paste CZC-15%-PA-C.

Table 4-5 Properties of different catalyst layers in each step of screen-printing.

Sample	Thickness (μm)			Mass (mg)		
	1st	2nd	3rd	1st	2nd	3rd
CZZ-15%-PA-C	5.60	11.6	17.01	17±1.5	35±1.8	54.2±1.4

4.3.2 CO_2 Hydrogenation to Methanol over CZZ and CZC Catalyst Layers

In the production of methanol, it is common practice to maintain strict reaction conditions with high pressure (at least 5.0 MPa) in order to increase the conversion of CO_2 and minimize the formation of CO [248, 249]. A techno-economic evaluation by Perez-Fortes et al. revealed that in a typical methanol CCU-plant, the compressors required to increase the system pressure account for 45% of the total equipment cost, and the energy consumed in gas compression represents 66% of the total electricity cost [250]. To address these issues, researchers have been working on modifying and developing catalysts that can perform under moderate reaction pressures. However, the current catalytic performance under such conditions is still suboptimal. General copper-based catalysts, including CZ, CA, and CZA, have demonstrated an average methanol selectivity of only 40-60% when tested at 30 bar and 250°C. Wang and co-authors studied the CZZ catalyst's ternary interaction for CO_2 hydrogenation to methanol, finding that adjusting the ZnO and ZrO_2 interaction is a crucial factor for designing high-performance catalysts. By using smaller ZnO particles in the CZZ catalyst, they achieved around 80% selectivity at 493 K and 30 bar for methanol production from CO_2 [32].

Consequently, the utilization of various promoters such as ZrO_2 has a beneficial impact on the copper-based catalyst. In this section, the effectiveness of utilizing layered catalysts CZZ-PA-C and CZC-PA-C in facilitating the conversion of CO_2 to methanol is evaluated. Catalytic tests were performed under controlled conditions, with a pressure of 30 bar, a temperature range of 200-240°C, a H_2/ CO_2 ratio of 3:1, and an internal standard of 10 vol.-% N_2. The gas hourly space velocity (GHSV) was constant at 7400 $Nml_{reag}\ h^{-1}\ g_{cat}^{-1}$. CO_2-conversion (X_{CO2}) and product selectivity (S_i) were calculated using Equations 3.2 and 3.3. In particular, the catalytic performance of both CTM catalysts is affected by changes in reaction temperature. The findings depicted in Figure 4.13 highlight that raising the reaction temperature from 200°C to 240°C leads to a marked increase in the overall conversion of CO_2, from 4.7% to 10.67% for CZZ-PA-C and from 5.7% to 12.67% for CZC-PA-C. It is widely recognized that the CO_2 hydrogenation process occurs via two competing reactions, namely methanol synthesis and reverse water-gas shift (RWGS). The fraction of CO_2 that undergoes conversion into CO displays a steady rise with increasing temperature, attributable to both the favorable thermodynamics of the endothermic RWGS reaction at higher temperatures and the enhanced reaction kinetics facilitated by the increased temperature. Furthermore, the CZC-PA-C catalyst demonstrates a higher level of conversion and greater selectivity in comparison to the CZZ-PA-C catalyst. Specifically, at a higher temperature of 240°C, the methanol selectivity for CZC-PA-C remains at 79.9% with an S_{MeOH}/S_{CO} ratio of 3.9, while the CZZ-PA-C catalyst under the same conditions shows a selectivity of

approximately 67.3% and an S_{MeOH}/S_{CO} ratio of only 2.05. Additionally, a decrease in reaction temperature has been observed to promote the selectivity to methanol, albeit at the expense of a reduction in CO_2 conversion. Both catalysts demonstrated an increase in methanol yield, with CZC-PA-C exhibiting a superior performance, achieving a yield range of 5.14% to 10.12%. Conversely, the CZZ-PA-C catalyst displayed a lower activity towards methanol synthesis, achieving a maximum yield of 7.2% at 240°C. The results presented in this investigation, combined with the characterization data, provide a plausible explanation for the variances in activity and product distribution observed during the CO_2-to-MeOH reaction. The dissimilarities in the copper surface area of the prepared systems (See Table 4.2) could be responsible for the disparate catalytic performance. However, in agreement with previous research conducted by several other authors [251], this is merely one of several factors that can influence catalyst activity. These other factors include, but are not limited to, the creation of an intimate bond between metallic copper and oxide carriers [252], the stabilization of low-valence state copper species ($Cu^{\delta+}$) on oxygen surface vacancies [253], and a change in the morphology of the metallic sites. These observations suggest that the three oxides present in the CZC-PA-C catalyst may have a more effective synergistic effect compared to CZZ-PA-C due to their closer contact. In a related study, Fang et al. also examined CO_2 conversion under moderate pressure (30 bar), and observed a selectivity of 68% for the CZZ catalyst at 250°C. However, the researchers promoted their catalyst, a hybrid catalyst/adsorbent consisting of CZZ supported with hydrotalcite, and found that under

the same operating conditions, the S_{MeOH}/S_{CO} ratio was equal to 5, but CO_2 conversion rate was only about 4.5% [254]. In a previous study at IMVT, the conversion of CO_2 to methanol was investigated using CZA and CZZ catalysts with various precursor solutions in a micro-berty reactor. The results showed that for CZA, the main product was CO, and the maximum methanol production was about 40% at 230°C [222]. Other literature reported that while good activity has been achieved, the stability of CZA for CO_2 hydrogenation has not been sufficient due to the hydrophilic nature of Al in the catalyst, which can adsorb water generated in CO_2 hydrogenation to methanol and reverse water gas shift reactions, thus reducing activity [255, 256]. Prašnikar et al. conducted a study on the deactivation mechanisms of CZA catalysts during CO_2 reduction to methanol, exploring the underlying processes involved in the reaction. Based on their findings, they determined that the primary reason for catalyst deactivation is the acceleration of Al_2O_3 sintering when exposed to water. When the molar fraction of H_2O is raised, the surface area of Al_2O_3 tends to decrease, which in turn leads to an augmentation in the size of Cu particles. They observed that the impact of H_2O on Cu form and Al_2O_3 phase was clear-cut. However, the size of ZnO particles was found to be affected by multiple factors including CO_2 and other reaction products. They conducted various analytical methods and verified that exposure to high concentrations of CO and CH_3OH led to the ZnO phase covering the copper particles [257]. On the other hand, for CZZ, the use of different precursor solutions in FSP synthesis resulted in different outcomes, with the maximum methanol selectivity at 210°C being approximately 75% [222].

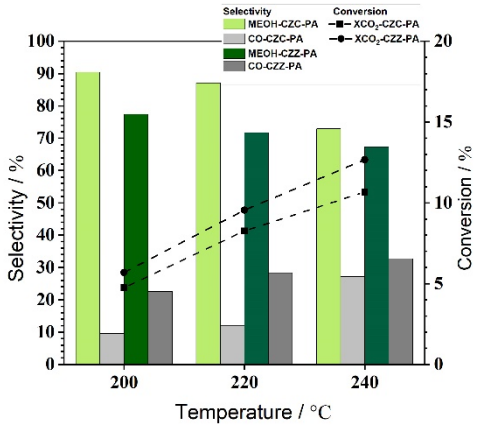

Figure 4-13 Effect of reaction temperature on CO_2 conversion, and product selectivity at a reaction pressure of 30 bar(g), GHSV=7400 $Nml_{reag}\ h^{-1}\ g_{cat}^{-1}$.

4.4 Planar Catalyst Layers for Direct DME Synthesis

Different coating arrangements were proposed for the integration of CTM-MTD in micro-channel reactors, including face-to-face patterns, double-layer patterns, and hybrid patterns. In the face-to-face patterns, CTM and MTD catalysts were printed on independent foils and then combined using foil a face to face arrangement. In the double-layer pattern, the CTM catalyst was printed first and subsequently covered by a layer of the MTD catalyst. A paste containing both CTM and MTD catalysts was developed for the hybrid pattern. The preparation methodology for the pastes and their compositions are explained in Section 3.2 and Table 3.1, respectively.

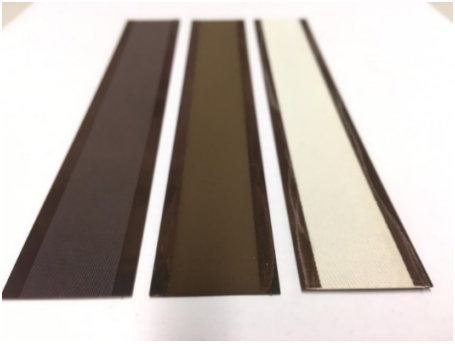

Figure 4-14 Coated Foils (left to right: empty, hybrid coating, double layer coating).

4.4.1 Structural Characterization of Hybrid Layer Systems

To achieve maximum cooperative effects, it may be advantageous to position the metal oxides and acid components in close proximity to each other, as this should allow for an effective interaction coupling of the two reactions. Therefore, in this section, the characteristics of a

hybrid planar configuration consisting of CZC-Z-HLA-C and CZZ-Z-HLA-C are examined. The SE-micrographs and cross-sectional analysis of the layer via EPMA and elemental distribution are presented in Figure 4.15A and Figure 4.15B, respectively. The hybrid catalyst paste was prepared using a 1:1 ratio by weight of the two catalysts, as explained in Section 4.2.1. A 15% powder hybrid paste was selected for both catalysts, as per the guidance provided in Section 4.2.1 with regard to the rheology of the pastes. In all catalyst layers, the top view shows (a) the absence of cracking and (b) a uniform distribution of the catalyst along the foils and within each micro-channel. This also allows assuming that each microchannel contained about the same amount of catalyst and, further, that each channel caused a similar pressure drop, i.e., the flow velocity and residence time in all channels was similar. Therefore, it is justified to assume that the microreactor can be considered as a system of 30x49 parallel plug-flow reactors [258]. After coating the hybrid paste, each of the 30 foils was found to contain an average of 29±4 mg of CZC/Z-Z-HLA-C catalyst per individual screen-printing run. In order to achieve a sufficient quantity of catalyst on the foils, the printing process was repeated twice, resulting in a total of 2.02 g and 2.29 g of CZC-Z-HLA and CZZ-Z-HLA catalyst on all 30 foils, respectively. Based on the results of image analysis, it could be determined that the thickness of the coating at the center line of the channels was approximately 18.85 μm for CZC-Z-HLA and 22.35 μm for CZZ- Z-HLA.

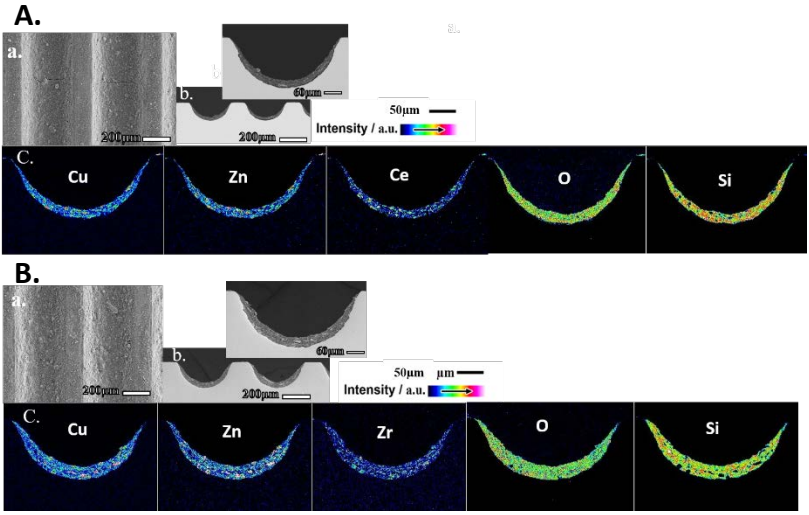

Figure 4-15 (a) SE-micrographs, (b) cross-sectional analysis of the layer via EPMA/BSE and c) elemental map via EPMA/WDX for the CZZ/C-Z-HLA layer obtained from the paste (A) CZC-Z-HLA15%-PA-C and (B) CZC-Z-HLA-15%-PA-C.

4.4.2 CO_2 Hydrogenation to DME over Hybrid Catalyst Layers

Recently, the development of novel hybrid multi-metallic/zeolite systems has gained attention through researchers in the technology of direct DME from CO_2. Various researchers have conducted studies on hybrid catalysts prepared through different methods such as physical mixing, co-precipitation, etc. for direct DME synthesis. [259–262]. This section focuses on the investigation of hybrid layer catalysts for direct DME synthesis in a microchannel reactor in accordance with the details provided in Section 3.4, the experiments were carried out using different operating conditions for both catalysts. The initial experiment was conducted with the CZZ-Z-HLA

catalyst at varying temperatures as can be seen in Figure 4.16. Unexpectedly, the conversion was less than 2% with no detectable DME at a temperature of 220°C. Moreover, the CO_2 conversion remained low even at higher temperatures. Specifically, at 240°C, the conversion was only 3.2%, and it increased to 8.8% at 280°C. Unexpected results were obtained regarding selectivity as well, as at all these temperatures, the selectivity towards DME was very low, whereas methanol was the dominant product. The highest percentage of DME was obtained at 280°C, but even then, the primary product was CO. In addition to the anticipated products of methanol, DME, and CO, there was also an increase in the concentration of methane observed as a byproduct with increasing temperature, similar to that of CO. The previous study at IMVT [222] also observed this phenomenon, but did not achieve any significant conversion of syngas with coated hybrid catalyst (CZA-HZSM-5) until a temperature of 240°C, and the conversion was less than 1% at temperatures between 260°C -280°C. As discussed in Section 3.2, the presence of terpinol was found to affect the activity of the zeolite paste. Based on the explanation provided in the previous study, it can be inferred that the proposed method for deactivating zeolite involves the participation of protons in the HZSM-5 structure. As a result of this reaction, there is a decrease in acidity and activity for the dehydration of MeOH. Thus, the reason for the acid catalyst's low activity can be attributed to its degradation [222]. However, it should be noted that the solvent used in this study the same as another previous studies at IMVT which they used HZSM-5 as hydrocracking catalyst in research , where there was no observed deactivation effect

on the zeolite paste [242]. It can be concluded that the zeolite paste is not affected by the solvent in this study.

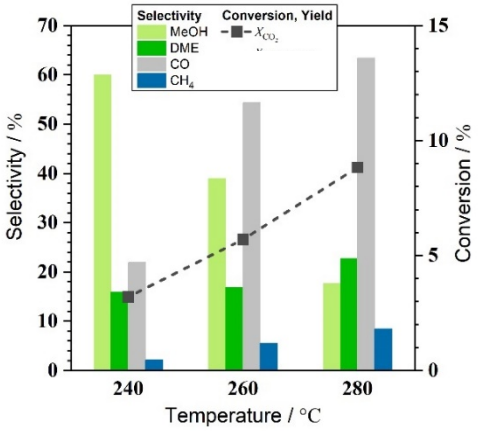

Figure 4-16 Activity of the CZZ- Z-HLA catalyst system in terms of X_{CO2} and S_i in the CTD reaction at reaction pressure of 30 bar(g), GHSV=9700 Nml_{reag} h^{-1} g_{cat}^{-1}.

The experimental conditions for the CZC-Z-HLA catalyst involved varying temperatures, and the results showed (Figure 4.17) that the CO_2 conversion increased from 7.2% at 220°C to 13.24% at 280°C which was comparable to CZZ-Z-HLA. In the case of methanol dehydration, a similar trend was observed. At 220°C, the methanol selectivity was around 73.6%, but it decreased to 26.1% with increasing temperature, as the RWGS reaction become more favorable at higher temperatures, as previously discussed. Furthermore, the selectivity of DME was only around 13% to 15%. By comparing both catalysts, it can be concluded that the methanol selectivity was higher, as evidenced in the methanol synthesis

section, and the CO selectivity was lower at higher temperatures. As discussed in the paste characterization section (see Section 4.2.4), the inclusion of cerium led to higher stability of the copper surface area, resulting in increased activity and conversion in the direct DME synthesis.

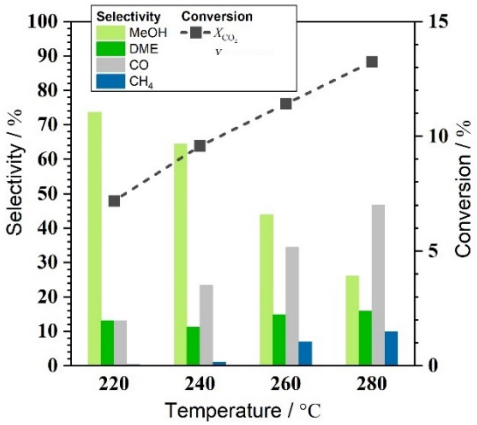

Figure 4-17 Activity of the CZC- Z-HLA catalyst system in terms of X_{CO2} and S_i in the CTD reaction at reaction pressure of 30 bar(g), GHSV=9700 Nml_{reag} h^{-1} g_{cat}^{-1}.

The hybrid catalyst was observed to have a reduction in micro-porosity compared to the pure zeolite, along with a higher reduction temperature, as explained in Section 4.2.4. However, in order to gain insight into the potential impact on the paste, TPD measurements were conducted using ammonia as a small probe molecule. This allowed for the detection of acid sites, even in the narrow pores of the catalyst, as pore accessibility is a critical factor that needs to be considered. Figure 4.18 illustrates that the pure zeolite paste displays three peaks in different regions, indicating the presence of three types

of acid sites. The first peak, between 100°C and 250°C, is typically attributed to the desorption of weakly bound ammonia from the zeolite framework's Lewis acid sites. The second peak falls within the range of 250°C - 400°C and is usually associated with the desorption of ammonia from medium-strength extra framework aluminum oxide/hydroxide species. The third peak, above 400°C, is attributed to the desorption of ammonia from strong Brønsted acid sites [263]. Obviously, the hybrid systems show changes not only in the relative distribution of the acid sites but also demonstrates that a reduction in the intensity of the third peak and the population of medium acid site is increased.

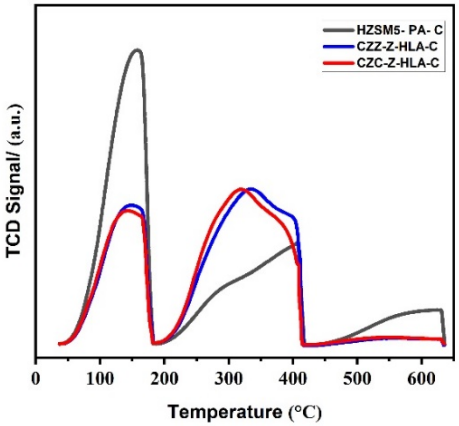

Figure 4-18 Comparison of NH_3-TPD profiles for HZSM-5-PA and hybrid CZZ-Z-HLA and CZC-Z-HLA with the ratio of (CZZ/C-Z= 1:1) catalyst after calcination.

From a quantitative point of view (see Table 4.6), the pure zeolite paste has the highest acid capacity which is 0.91 $mmol_{NH3}/g_{cat}$, which

is about 0.1 mmol/g_{cat} is for strong Brønsted acid sites.

Table 4-6 Quantitative values of NH_3-TPD of investigated pure zeolite and hybrid paste samples after calcination

Sample	**[a]NH_3 uptake (mmol/g_{cat})**	**[b]Td_1**	**[b]Td_2**	**[b]Td_3**	**[c]n_1**	**[c]n_2**	**[c]n_3**
HZSM-5_PA	0.91	157.9	406.2	629.6	0.6	0.29	0.11
CZZ-Z-HLA	0.68	148.9	335	-	0.4	0.57	0.03
CZC-Z-HLA	0.66	141.8	318.9	-	0.41	0.56	0.03

a. Cumulative acidity in the range of 100-600°C

b. Temperature of maximum desorption of NH_3 (Td)

c. Fractional population of acid sites

It is expected that the number of acid sites on the hybrid catalysts should be theoretically 50% lower than the bare zeolites, with an approximate 1:1 ratio between the two powdered catalysts. Despite the reduction in total acidity due to the deposition of CZZ on the zeolites, the NH_3 uptake on the hybrid catalysts is observed to be even higher than expected. Upon employing the CTM and CTD catalysts to formulate the paste, a noticeable redistribution of the acid population among the medium and strong acid sites was observed. This indicates the formation of new Lewis sites, possibly due to ion exchange of zeolite protons by metallic species during the paste preparation [264]. However, it is important to take into account possible alterations in the structure of zeolites under steaming

conditions, which could lead to dealumination and the formation of non-acidic aluminum species, ultimately resulting in a reduction in the volume of micropores [265]. It must also be taken into account that the decrease in the Brønsted acidity in the copper containing catalysts could be due to the migration of unreduced copper ions in the zeolite channels during the reduction and reaction can happen [266]. Ordomsky et al. and colleagues analyzed the deactivation of the CZA/HZSM-5 catalyst during DME synthesis. Over time, the hybrid catalyst's effectiveness decreased due to multiple factors, including copper sintering, copper oxidation, and ion exchange with zeolite hydroxyl groups. As a result of copper sintering, the number of metal active sites declined, and the ion exchange of Cu^{2+} ions with the hydroxyl groups of the zeolite resulted in fewer acid sites for methanol dehydration [193]. According to García-Trenco and colleagues, the syngas-to-DME reaction results in Cu^{2+} species and Zn^{2+} cations occupying exchange positions within the HZSM-5 zeolite. This action leads to a reduction in the number of Brønsted sites and the formation of Lewis sites in the CZA/HZSM-5 hybrid system, which ultimately causes deactivation [267]. The identification of this cause could have been achieved through analyzing the sample post-reaction. However, due to the catalyst being coated onto the foils, it was not feasible to separate the catalyst from the foil, rendering such analysis impossible in this study. Moreover, Bonura et al. studied the interaction between CZZ and various zeolite types and found the deactivation of their catalyst in few hours. Their findings indicated that while an excess of acid sites did not improve process performance, having an appropriate density of acid sites was

crucial in promoting the methanol-to-DME dehydration rate, as well as shifting the position of CO_2 conversion (CO_2 → MeOH → DME). This finding is significant in terms of the observed deactivation trend and should be carefully considered [247]. Moreover, through research, it has been established that the effectiveness of the methanol dehydration reaction catalyst is heavily influenced by the strength of its acid sites, as well as the presence of Brønsted acid sites. It has been observed that more active catalysts have stronger acid sites [268, 269].

4.4.3 Structural Characterization of Double Layers

As previously indicated, the two catalysts involved, namely the methanol synthesis catalyst CZZ/CZC and the methanol dehydration catalyst zeolite HZSM-5, are implemented in a double layer configuration within the channels of micro-structured foils using screen printing. Figure 4.19 shows the top-view resp. cross-sectional view of a double layer printed to a microchannels. The micrographs indicate that with the printing procedure applied, layers without cracks were achieved (Figure 4.19a). Especially the zeolite layers show a thickness distribution which follows the shape of the channel. This is due to gravity effects after screen printing. However, as exemplarily depicted in Figure 4.19b, all channels show a similar thickness distribution and total double layer thickness. Further, the elemental distribution (Figure 4.19c) shows a homogeneous distribution of the two catalysts within the channel with the zeolite layer completely covering the CZZ-layer as intended. By coating the CZZ paste, each of the 30 coated foils contained on average 19±5 mg of CZZ catalyst per individual run of screen printing. As mentioned,

to reach a larger thickness resp. catalyst mass, the CZZ catalyst was consequently printed twice resulting in 38±8 mg of CZZ per foil on average. For ZSM-5, due to the higher catalyst amount in the paste (see Table 3.1), a single run of printing was sufficient to achieve the same mass of catalyst printed resulting in the 1:1 mass ratio CZZ: zeolite within the double layer configuration (zeolite: 33±6 mg on average per foil of the set of 30 foils). Determined via image analysis, the overall thickness at the center of the channel is about 31 μm (CZZ catalyst layer thickness approx. 10 μm, zeolite layer thickness approx. 21 μm due to the differences in density). Consequently, for the performance test using the 30 coated foils, a total mass of 2.20 g double layer catalyst (1.12 g CZZ catalyst + 1.10 g zeolite catalyst) was loaded in the reactor. Figure A.2 also shows the cross-sectional and the elemental distribution of the CZC-Z-DLA catalyst. The total amount of the catalyst for the double layer was about 1.93 g (0.98 CZC catalyst+0.95 g of zeolite) and thickness about 21.

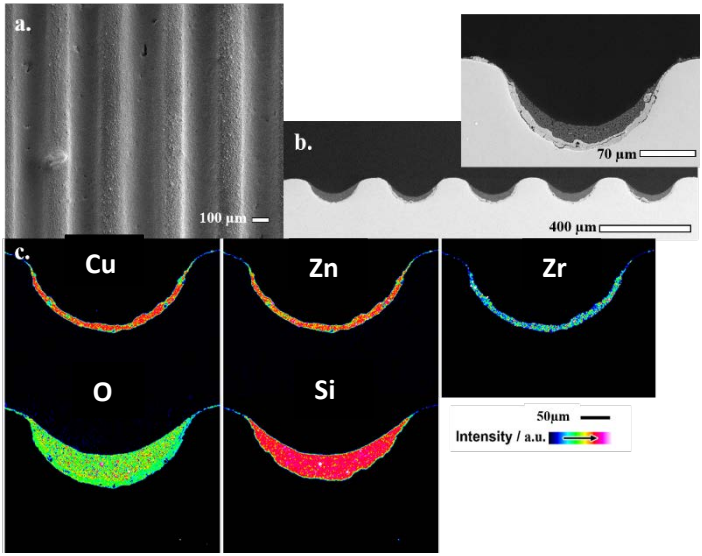

Figure 4-19 Characterization of the CZZ-Z printed double layer: Top-view (a) SE-micrograph (b) cross-sectional analysis of the layer via EPMA/BSE, (c) elemental map via EPMA/WDX.

4.4.4 CO_2 Hydrogenation to DME over Double layer Catalyst

As in the previous sectioned mentioned, the primary obstacle facing hybrid catalysts in direct DME synthesis from CO_2 is the issue of deactivation, which is heavily influenced by the interaction between the catalyst's metal and acid sites. As such, designing an effective catalyst requires careful consideration of how to achieve optimal synergy between these two functionalities by controlling their nature, balance, contact, and proximity. To address this problem, earlier investigations have shown that the CZA@Z and CZA-Z-DLA catalyst configurations exhibit different activity levels, owing to their distinct characteristics. The differences in intercrystalline porosity between

CZA@Z and CZA-Z-DLA are responsible for the variation in their activity levels. The former has a HZSM-5 shell with micropores that hinder the transport of reactants due to its low porosity, whereas the latter has randomly oriented crystals that allow for higher X_{CO} by preventing transport limitations. As a result, the double-layer structure was considered a promising configuration for DME direct synthesis [202, 270]. In this section, the performance of two CTM catalysts coated with MTD, as discussed in Section 3.4, was analyzed under various operating conditions. The catalytic performance of the CZZ-zeolite double layer was studied in the combined CO_2 hydrogenation to methanol and methanol dehydration to DME first at a reaction pressure of 30 bar(g) at different reaction temperatures. As can be seen in Figure 4.20, CO_2-conversion increased with increasing reaction temperature as to be expected. However, with increasing temperature, CO selectivity increased obviously due to a promoted reverse water-gas shift reaction (endothermic, see reaction eq. (3)) [271], while methanol and DME selectivity decreases from 16.9% to 7.4% and from 48.6% to 23.9%, respectively, between 220°C and 280°C. In parallel, methane formation, being a side reaction, is likewise increased with increasing reaction temperature. Eventually, at 30 bar(g), the highest yield of DME of about 3% was achieved at 240°C at a CO_2 conversion of 6.37% and the main product was CO at a temperature of 260°C. It is evident that the implementation of the double-layered configuration results in a significant improvement in the synergistic effect of the two catalysts, yielding in a substantial ratio of 2.9 in dimethyl ether selectivity at 240°C compared to the hybrid layer catalyst where the two components are mixed at the

powder scale for paste production. The observed phenomenon can be attributed to the fact that, although both hybrid catalyst and double-layer configurations have the same ratio of CTM/MTD catalyst, the total NH_3 uptake is higher for the pure zeolite catalyst. This higher uptake enables us to take advantage of the remaining Brønsted acid sites and greater quantity of Lewis acid sites present in the pure zeolite layers (see Figure 4.20). It means that the double-layer configuration effectively restricts the direct contact of the two components to the interfacial region, thereby minimizing any negative interactions between them and causes the deactivation to happen after longer time. Chen et al. also investigated a monolithic supported bifunctional catalyst recently, coated onto a channel surface of metallic monolith substrate as two layers (wash-coating method), to facilitate direct CO_2 synthesis to DME, recently. They discovered that a layered catalyst configuration significantly improved the synergistic effect of its two components. This led to a 20% increase in DME productivity at 240°C, in comparison to a catalyst with different levels of proximity (CZZ on FER<1 μm, CZZ+FER<10 μm and CZZ+FER> 250) which pelletized and sieved to 250-500 μm. They also found that the CO productivity for the layered catalyst was slightly higher than the pelletized catalyst at temperature higher than 240°C, however, the layered catalyst exhibited improved durability [272]. As a result, this design successfully overcomes the durability issues commonly associated with typical bifunctional catalysts.

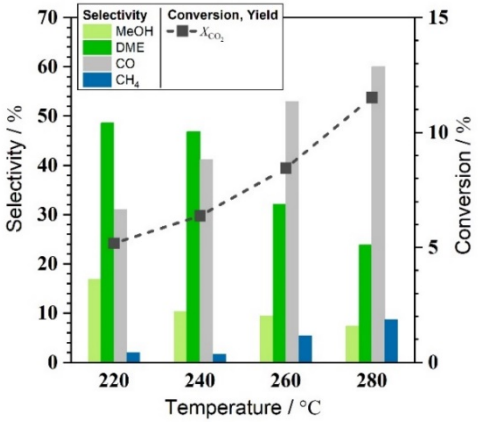

Figure 4-20 Effect of reaction temperature on CO_2 conversion and product selectivity at reaction pressure of 30 bar(g), GHSV=9700 $Nml_{reag}\ h^{-1}\ g_{cat}^{-1}$ for CZZ-Z-DLA catalyst layer.

Moreover, Jung et al. investigated how the catalytic activity of DME is affected by the surface area of copper and the presence of acidic sites [273]. Their findings revealed a significant correlation between these factors and the catalytic activity on the reactions. As it can be seen in the Figure 4.21, the activity of CZC-Z-DLA catalyst is higher than the CZZ-Z-DLA. It can be inferred that the higher copper surface area of the CZC catalyst, combined with constant amount of acidic site in the second layer (zeolite layer), resulted in a higher conversion of carbon dioxide and a greater yield of DME. Specifically, at a temperature of 240°C, the CZC-Z-DLA catalyst demonstrated approximately 23% and 20% higher conversion and DME yield, respectively, relative to the CZZ-Z-DLA catalyst.

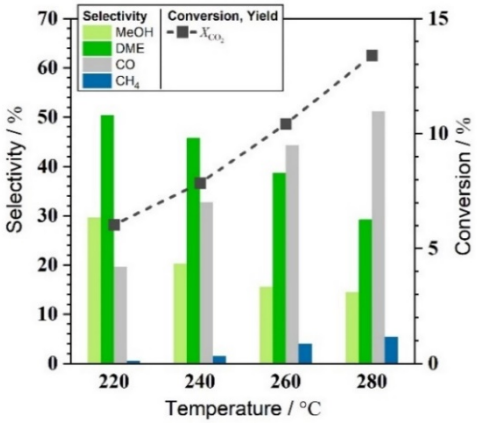

Figure 4-21 Effect of reaction temperature on CO_2 conversion and product selectivity at reaction pressure of 30 bar(g), GHSV=9700 $Nml_{reag}\ h^{-1}\ g_{cat}^{-1}$ for CZC-Z-DLA catalyst layer.

Additionally, to improve the conversion resp. to check the effect of residence time, the influence of the space velocity GHSV on the conversion-selectivity pattern of the CZC-zeolite double layer catalyst was examined by altering the space velocity from 9700 to 5250 $Nml_{reag}\ h^{-1}\ g_{cat}^{-1}$ at 240°C, which seemed to be the optimum temperature in terms of yield at 30 bar(g). The comparison is summarized in Figure 4.22. As to be expected, the CO_2 conversion increases for lower GHSV (X_{CO2} = 8% at 9700 $Nml_{reag}\ h^{-1}\ g_{cat}^{-1}$ versus X_{CO2} = 14.9% at 5250 $Nml_{reag}\ h^{-1}\ g_{cat}^{-1}$). Consequently, the reduction in the GHSV has a positive impact on the dimethyl ether yield. However, it is crucial to note that this decrease in GHSV is also accompanied by an approximately four-fold increase in the formation of byproducts, such as methane. It is also worth noting that although the catalyst double layer was exposed to various operating

conditions (GHSV, pressure, and temperature) no noticeable deactivation after 42 hours of reaction was observed: from the initial resp. final reference operating point (9700 Nml_{reag} h^{-1} g_{cat}^{-1}, 220 °C, 30 bar(g)), CO_2-conversion decreased by about 2.3% to 5.9 % and DME selectivity decreased by about 4% to 48.3%. This demonstrates that the CZC-zeolite double layer catalyst is quite stable even though long-term experiments would be needed in order to quantify potential deactivation behavior.

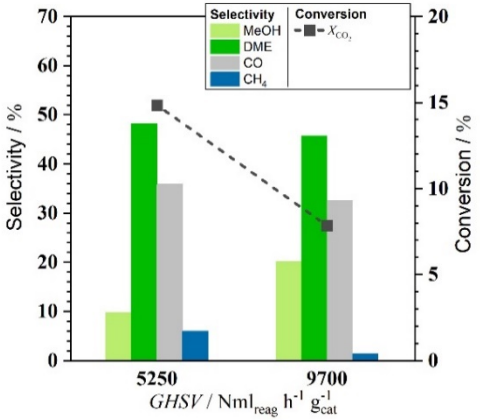

Figure 4-22 Effect of space velocity on CO_2 conversion, product selectivity at a reaction pressure of 30 bar(g) and a reaction temperature of 240 °C for CZC-Z-DLA.

Figure 4.23 presents the influence of gas hourly space velocity on the performance of the CZZ-Z-DLA catalyst. Decreasing GHSV resulted in an increase in the conversion of CO_2, albeit it is important to note that CO can be considered as a secondary product, as the yield of DME surpassed that of CO by approximately 2%. Moreover, a comparison between the two catalysts not only demonstrated that the

conversion of CZC-Z-DLA was approximately 20% higher than that of CZZ-Z-DLA, in line with the previously discussed expectations, but also exhibited an improvement in the DME yield and a lower CO percentage of around 18% at a GHSV of 5250 $Nml_{reag}\ h^{-1}\ g_{cat}^{-1}$.

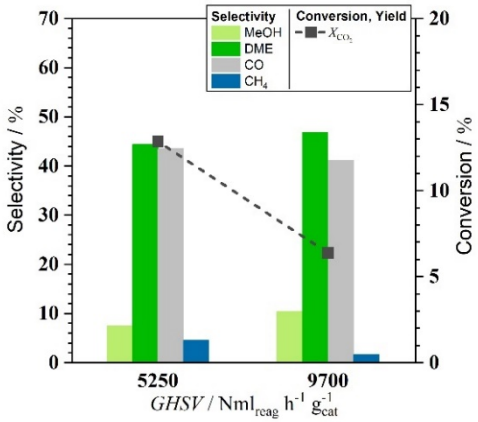

Figure 4-23 Effect of space velocity on CO_2 conversion product selectivity at a reaction pressure of 30 bar(g) and a reaction temperature of 240 °C for CZZ-Z-DLA.

To investigate the influence of pressure on the dimethyl ether (DME) yield, the effect of pressure was examined for the CZZ-Z-DLA catalyst. As the overall reaction stoichiometry of DME synthesis from CO_2/H_2 mixtures results in a strong decrease in volume, higher pressure favors MeOH and DME formation. As shown in Figure 4.24, with increasing reaction pressure from 30 bar(g) over 35 bar(g) to 40 bar(g), CO_2 conversion increases by a factor of 1.8 (from 12.8% at 30 bar(g) to 23.4 % at 40 bar(g)) at the reference reaction temperature of 240 °C and GHSV=5250 $Nml_{reag}\ h^{-1}\ g_{cat}^{-1}$. Besides the increase in

conversion, the selectivity is likewise positively affected by a higher reaction pressure: at 40 bar(g) the DME yield of 12.27% is by a factor of about 2 higher than at 30 bar(g), while the selectivity to CO and CH_4 decreases with increasing reaction pressure. Furthermore, at 240 °C, the average ratio of DME/MeOH selectivity is 6.7 at 40 bar(g) compared to 5.7 at 30 bar(g), demonstrating that high reaction pressure promotes further methanol dehydration to DME.

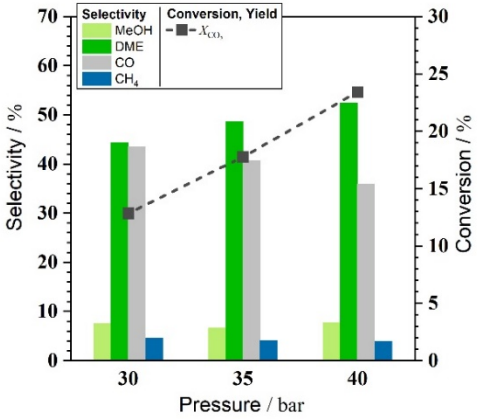

Figure 4-24 Effect of reaction pressure on CO_2 conversion, product selectivity at a reaction temperature of 240 °C and GHSV=5250 $Nml_{reag}\,h^{-1}\,g^{cat-1}$ for CZZ-Z-DLA.

4.4.5 Structural Characterization of Face-to-Face Layer

To construct the catalytic foil stack, 30 parallel foils are arranged in a facing position, resulting in the formation of 15 layers of circular channels. The printing process for CZZ and CZC catalysts were explained in the methanol section, which was the same for both catalysts. The amount of catalyst used was approximately 1 g, and the printing process for zeolite was performed twice with a catalyst amount of around 1.1 g. The thickness of zeolite was observed to be 36 μm, as shown in Figure 4.25. However, the thickness of the CTM catalyst was comparatively lower, as previously mentioned (see section 4.3). The catalyst layer exhibits the presence of blisters on its surface; however, the metallic active components are uniformly distributed throughout the channels.

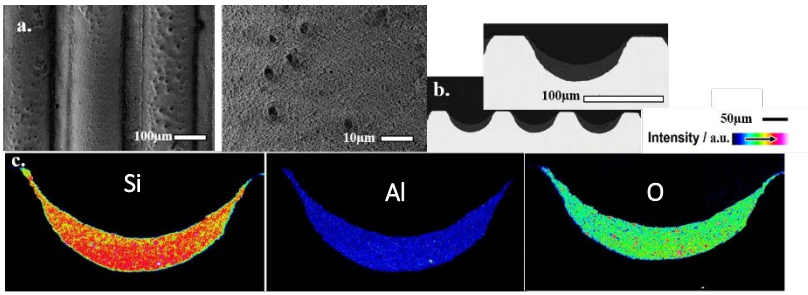

Figure 4-25 Characterization of the printed double layer: Top-view (a) SE-micrograph (b) cross-sectional analysis of the layer via EPMA/BSE, (c) elemental map via EPMA/WDX.

4.4.6 CO_2 Hydrogenation to DME over Face-to Face Catalyst

The reactor test was performed under identical operating conditions for both catalysts, similar to the other two configurations (double layer and hybrid layer). However, the product distribution differs between the two catalysts. Figure 4.26 shows that with the CZZ catalyst, even at 220°C, the selectivity towards CO is notably higher, by about 14%, compared to DME. Additionally, the increase of conversion is more pronounced for CZZ than for CZC as well as that of the selectivity of CO, especially at higher temperature (Figure 4.27 for CZC results). There exist several hypotheses for the CZZ catalyst that may account for the prevalence of CO as the primary product in face-to-face configuration. This is related to the CO_2 activation reaction mechanism on copper catalyst which is shown in Figure A.7 and also to the methanol dehydration reaction pathways which is shown in Figure A.8 (Appendix).

As it is discussed, the catalyst which is produced with cerium promoter has higher activity with regard to production of DME, therefore, one can conclude the cerium can promote the formate mechanism in which CO_2 is hydrogenated via formate as an intermediate to produce methanol [274]. However, zirconia may promote the RWGS mechanism in which CO_2 is first reduced to CO and then hydrogenated to produce methanol. Additionally, the CZZ catalyst might possesses low energy adsorption sites for CO, causing the rapid desorption of CO and facilitating improved RWGS, and the CO may not have enough time to convert to methanol and goes out of the reactor. Also, the presence of a gap between the two catalysts impedes the proper diffusion of methanol to the zeolite surface and

methanol is not produced fast enough, resulting in reduced DME selectivity. Consequently, CO_2 is utilized to generate higher quantities of CO and methane, rather than methanol and DME. Moreover, parallel reaction can happen easier as the synergic effect between the two catalyst is lower, therefore, more methane is produced in comparison to double layer. Methane can be produced from methanation of CO or CO_2 [275]. Formaldehyde also can be produced from CO which is adsorbed on the catalyst (Figure A.7). However, formaldehyde reacts very fast further to produce methanol or methane, methane being the final product [276]. Due to the rapid reaction rate of formaldehyde, the peak associated with formaldehyde either did not manifest or was underestimated because of limit of detection.

Regardless of the specific reaction conditions, both mechanisms (associative and dissociative pathway for methanol to DME mechanism Figure A.8) involve the cooperation of Brønsted acidic sites located on the dehydration component during methanol condensation [277–280]. Wang et.al also mentioned that the surface methoxy species in the conversion of methanol to DME on acidic zeolite play and important role [281]which could be the reason of different product distribution in double layer and face-to face layer. Nevertheless, it would need more specific investigations like (CO_2-TPD, methanol-TPD and CO-TPD) to prove which of the explanations is valid. Due to technical issues this was not possible at the institute during the respective time.

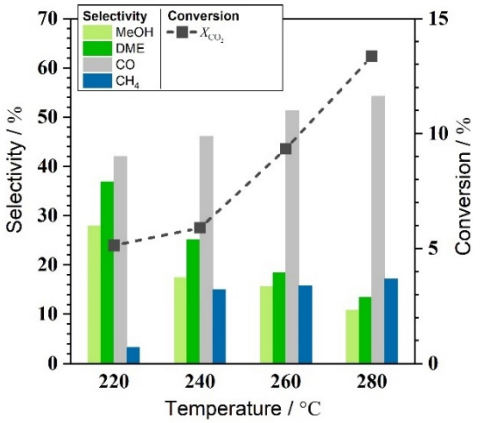

Figure 4-26 Effect of reaction temperature on CO_2 conversion and product selectivity at reaction pressure of 30 bar(g), GHSV=9700 $Nml_{reag}\ h^{-1}\ g_{cat}^{-1}$ for CZZ-Z-FLA catalyst layer.

Figure 4.27 demonstrates that the CZC catalyst produces more DME at lower temperatures (220°C and 240°C) and exhibits a higher conversion of methanol to DME compared to the CZZ catalyst. One possible explanation could be attributed to the increased partial pressure of methanol, resulting from the higher activity of the CZC catalyst. Consequently, the adsorbed methanol molecules attain a state of stabilization by means of dimerization, thereby undergoing subsequent dehydration to yield dimethyl ether (DME) [164]. Furthermore, the CZC catalyst produces less CO than the CZZ catalyst, which can be attributed to its higher energy desorption sites for CO and associative pathway that exhibits higher selectivity towards methanol dehydrogenation to the desired product. A comparison of the CZC-Z-DLA and CZC-Z-FLA configurations reveals that the face-to-face configuration exhibits lower conversion

of carbon dioxide, likely due to insufficient contact between the two catalysts. Additionally, when the temperature is reduced, methanol conversion is lower in the CZC-Z-FLA as opposed to the CZZ-Z-DLA arrangement, implying distinct reaction mechanisms between the two catalysts when they come into contact as in double layer, the layered catalyst structure guarantees that CH_3OH (and H_2O) molecules produced will have the chance to react on the zeolite catalyst, therefore, the synergic effect between the catalysts and the pathway of the reaction could be different from face-to-face.

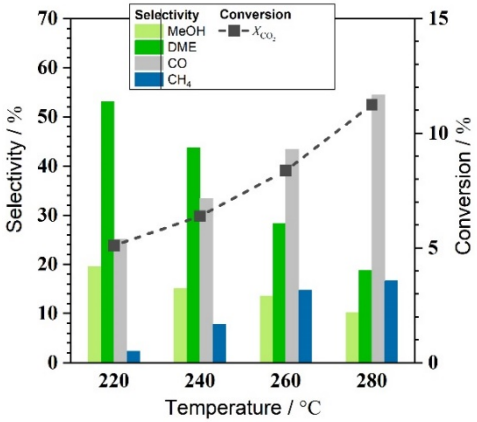

Figure 4-27 Effect of reaction temperature on CO_2 conversion and product selectivity at reaction pressure of 30 bar(g), GHSV=9700 $Nml_{reag}\ h^{-1}\ g_{cat}^{-1}$ for CZC-Z-FLA catalyst layer.

4.4.7 Comparison of Layers at Higher Pressure

As previously demonstrated in the double layer section, it is well established that lower gas hourly space velocity (GHSV) leads to higher conversion of CO_2 to DME. Furthermore, from a thermodynamic perspective, higher pressure is more favorable for the desired product. Hence, the experiments were conducted under the conditions of GHSV = 5250 $Nml_{reag}\ h^{-1}\ gcat^{-1}$, temperature of 240°C, and pressure of 40 bar, to investigate the DME yield for different layers under high-pressure conditions for CZC catalyst (see Table 4.7). The experimental results demonstrate that increasing pressure causes a decrease in the selectivity of carbon monoxide about 20% in comparison to 30 bar (Figure 4.22) for double layer configuration, while the selectivity of dimethyl ether (DME) increases. This finding reinforces the preference for elevated pressure conditions in the synthesis of DME via CO_2 hydrogenation, which is known to exhibit a molar decreasing reaction. Furthermore, the configuration with a double layer exhibits the highest conversion compared to the other configurations, indicating an increased interaction between CTM and MTD catalyst. The distance between the catalysts is found to play a role in the parallel reaction to produce methane, which is accelerated by an increase in CO production (S_{CH4}-HLA< S_{CH4} -DLA< S_{CH4}-FTF). The experimental findings clearly demonstrate that various catalyst configurations exhibit distinct synergistic effects on the yield of dimethyl ether (DME).

Table 4-7 Comparison of the conversion and selectivity of different layers for CZC-Z at T=240°C and GHSV=5250 $Nml_{reag}\ h^{-1}\ g_{cat}^{-1}$ P=40 bar.

Sample	X_{CO2}(%)	S_{MEOH}(%)	S_{DME}(%)	S_{CO}(%)	S_{CH4}(%)	Yield $_{DME}$
Hybrid	22.1	55.1	16.9	22.8	5.2	3.7
Double layer	26.6	9	53	27.6	10.4	14
Face-to-Face	18	7.5	44.2	34.5	13.8	8

5. Outlook and Summary

The present study explores the direct synthesis of dimethyl ether (DME) from carbon dioxide (CO_2) through the CTD reaction, using various catalyst configurations suitable for application in decentralized compact plants as part of the Power-to-X concept. To this end, two distinct nano-structured CTM catalysts (CZZ and CZC) have been synthesized via FSP and thoroughly characterized. Planar (coated) catalyst systems have been investigated for CZZ and CZC catalysts for methanol synthesis and also with combining with zeolite HZSM-5 (Z) for the subsequent dehydration, respectively. To ensure successful coating via screen printing for the planar systems, pastes containing the nano-powder (FSP-CZZ and/or C) were prepared, and their printability was evaluated by analyzing their rheological behavior. By optimizing the paste formulation, it was ensured that the coating process was carried out efficiently, resulting in high-quality coatings with good adhesion and uniformity. This step was crucial for achieving the desired catalytic activity and selectivity in the subsequent reactions. The use of FSP for the synthesis of the CZZ/C catalysts appears promising, as it satisfies the criteria outlined in the existing literature for nanoparticle structure, specific surface area, copper surface area and reducibility. Regarding the characterizing, it is showed that CZZ-631 and CZC-631 exhibits the most promising combination of specific surface area (BET and S_{Cu}), CuO crystallite size, particle size homogeneity within the sample,

and reduction behavior. Additionally, CZC shows higher stability during paste preparation as the copper surface area decreased lower after calcination in comparison to the CZZ. Therefore, CZC also shows higher activity during both CTM and CTD reactions in comparison to the CZZ catalyst. For the CTM-MTD integration, various configurations planar systems, such as the CZZ/C-Z-HLA, double layer (CZZ/C-Z-DLA), and face-to-face CZZ/C-Z-FLA layers, to be utilized in a micro-channel reactor (μ-CR).

The hybrid configuration of CTM and MTD catalysts (close contact) during paste preparation led to the degradation of Brønsted acid sites in zeolite catalysts, resulting in changes in the relative distribution of acid sites, ion exchange of Cu^{2+}, and dealumination. This transformation ultimately favored the production of CO and methanol as the major products. However, the double layer configuration (CZZ/C-Z-DLA) exhibited notable advantages as it effectively enhanced the synergistic effects between the two catalyst components. This double layer planar configuration demonstrated exceptional promise for the CO_2-to-DME (CTD) reaction in microchannel reactors (μ-CR), with high CO_2 conversion and yield of dimethyl ether. These findings suggest the potential of the CZC-Z-DLA system for efficient and selective dimethyl ether (DME) production as the yield of DME at 40 bar, 240 °C and GHSV= 5250 $Nml_{reag}\ h^{-1}\ gcat^{-1}$ was higher than CZZ-Z-DLA about 14% with lower percentage of byproducts. The face-to-face structure of CTM catalyst showed different production distribution due to lower catalytic activation of CZZ catalyst and different reaction mechanism between the two catalysts. It is noteworthy to mention that the selectivity of

dimethyl ether at lower temperatures and higher GHSV for the face-to-face configuration is comparable to that of the double layer configuration. However, the conversion of CO_2 to DME was lower for the face-to-face arrangement. Moreover, the distance between CTM and MTD catalysts caused different results compared to the double layer as MeOH was forced to pass through the zeolite catalyst, resulting in lower parallel reactions and lower percentage of CO and methane in the double layer catalyst. This study sets the foundation for future investigations to delve into a more detailed study of the reaction mechanism of various layer configurations through in situ characterization techniques such as TPH, XPS, SSITKA, and IR spectroscopy. These techniques can provide valuable insights into the interactions between the catalysts and the reactants, allowing for optimization of the layer configurations and catalysts to achieve higher DME product yields and avoiding the deactivation of the catalyst. Such studies are crucial for advancing the understanding and development of effective and efficient catalyst systems for the direct synthesis of DME from CO_2, contributing to the wider field of Power-to-X technology.

List of Abbreviation and Symbols

ANN	Artificial neural network
-C	Calcined
CA	CuO/ Al_2O_3
CTM	Carbon dioxide to methanol
CTD	Carbon dioxide to dimethylether
CZ	CuO/ZnO
CZZ	$CuO/ZnO/ZrO_2$
CZC	$CuO/ZnO/CeO_2$
CZA	$CuO/ZnO/Al_2O_3$
CZA@Z	Core shell
DFT	Density functional theory
DLA	Double layer
DME	Dimethylether
FID	Flame ionization detector
FLA	Face to face layer
FSP	Flame spray pyrolysis
GHSV	Gas hour space velocity
HLA	Hybrid layer
IR	Infrared spectroscopy
MEOH	Methanol
MOF	Metak-organic framework
MR	Membrane reactor
MTD	Methanol to DME
P	Pressure
PBMR	Packed bed membrane reactor
PBR	Packed bed reactor
PtF	Power to Fuel
PtX	Power-to-X
-PO	Powder
-PA	Paste

RWGS	Reverse water gas shift
SMSI	Specific metal/support interaction
STD	Syngas to dimethyl ether
STM	Syngas to methanol
Si	Selectivity of component
SSITKA	Steady-state isotopic transient kinetic analysis
T	Temperature
TCD	Thermal conductivity detector
TGA	Thermal gravimetric analysis
TPH	Total petroleum hydrocarbon
XPS	X-ray photoelectron spectroscopy
Xi	Conversion of component
Z	Zeolite HZSM-5
ZIF	Zeolitic imidazolate framework
μ-CR	Micro channel reactor
ΔG	Change in Gibbs free energy
ΔH	Enthalpy of reaction

List of Figures

List of Tables

Bibliography

[1] T. Bouman, M. Verschoor, C. J. Albers, G. Böhm, S. D. Fisher, W. Poortinga, L. Whitmarsh, L. Steg, *Global Environmental Change* **2020**, *62*, 102061. DOI: https://doi.org/10.1016/j.gloenvcha.2020.102061

[2] L.-W. Su, X.-R. Li, Z.-Y. Sun, *Energy Policy* **2013**, *63*, 130 – 138. DOI: https://doi.org/10.1016/j.enpol.2013.08.031

[3] E. Catizzone, G. Bonura, M. Migliori, F. Frusteri, G. Giordano, *Molecules (Basel, Switzerland)* **2017**, *23 (1)*. DOI: https://doi.org/10.3390/molecules23010031

[4] A. Berrada, K. Loudiyi, *Renewable and Sustainable Energy Reviews* **2016**, *59*, 1117 – 1129. DOI: https://doi.org/10.1016/j.rser.2016.01.048

[5] C. Jung, D. Taubert, D. Schindler, *Energy Conversion and Management* **2019**, *188*, 462 – 472. DOI: https://doi.org/10.1016/j.enconman.2019.03.072

[6] V. Dieterich, A. Buttler, A. Hanel, H. Spliethoff, S. Fendt, *Energy Environ. Sci.* **2020**, *13 (10)*, 3207 – 3252. DOI: https://doi.org/10.1039/D0EE01187H

[7] A. Goeppert, M. Czaun, G. K. Surya Prakash, G. A. Olah, *Energy Environ. Sci.* **2012**, *5 (7)*, 7833. DOI: https://doi.org/10.1039/C2EE21586A

[8] M. Yang, in *Towards Sustainable Chemical Processes*, Elsevier **2020**.

[9] P. Styring, G. R. M. Dowson, I. O. Tozer, *Front. Energy Res.* **2021**, *9*. DOI: https://doi.org/10.3389/fenrg.2021.663331

[10] [Cannot display the reference "IRENA 2021 – Renewable capacity statistics 2021", because the template "Bibliography - Internet Document - (Default template)" contains only fields that are empty in this reference.]

[11] J. R. Rostrup-Nielsen, *Catalysis Today* **2000**, *63 (2-4)*, 159 – 164. DOI: https://doi.org/10.1016/S0920-5861(00)00455-7

[12] *Beyond Oil and Gas: The Methanol Economy* (Eds: G. A. Olah, A. Goeppert, G. K. S. Prakash), Wiley-VCH Verlag GmbH & Co. KGaA, Weinheim, Germany **2009**.

[13] M. Behrens, *Angewandte Chemie (International ed. in English)* **2014**, *53 (45)*, 12022 – 12024. DOI: https://doi.org/10.1002/anie.201409282

[14] A. Buttler, H. Spliethoff, *Renewable and Sustainable Energy Reviews* **2018**, *82*, 2440 – 2454. DOI: https://doi.org/10.1016/j.rser.2017.09.003

[15] A. A. Tountas, G. A. Ozin, M. M. Sain, *Green Chem.* **2021**, *23 (1)*, 340 – 353. DOI: https://doi.org/10.1039/D0GC03115A

[16] M. Bukhtiyarova, T. Lunkenbein, K. Kähler, R. Schlögl, *Catal Lett* **2017**, *147 (2)*, 416 – 427. DOI: https://doi.org/10.1007/s10562-016-1960-x

[17] B. S. Clausen, J. Schitz, L. Grbk, C. V. Ovesen, K. W. Jacobsen, J. K. Nrskov, H. Topse, *Top Catal* **1994**, *1 (3-4)*, 367 – 376. DOI: https://doi.org/10.1007/BF01492289

[18] K. Omata, M. Hashimoto, Y. Watanabe, T. Umegaki, S. Wagatsuma, G. Ishiguro, M. Yamada, *Applied Catalysis A: General* **2004**, *262 (2)*, 207 – 214. DOI: https://doi.org/10.1016/j.apcata.2003.11.028

[19] S. Polierer, J. Jelic, S. Pitter, F. Studt, *J. Phys. Chem. C* **2019**, *123 (44)*, 26904 – 26911.

DOI: https://doi.org/10.1021/acs.jpcc.9b06500

[20] M. Behrens, F. Studt, I. Kasatkin, S. Kühl, M. Hävecker, F. Abild-Pedersen, S. Zander, F. Girgsdies, P. Kurr, B.-L. Kniep, M. Tovar, R. W. Fischer, J. K. Nørskov, R. Schlögl, *Science (New York, N.Y.)* **2012**, *336 (6083)*, 893 – 897. DOI: https://doi.org/10.1126/science.1219831

[21] F. Dalena, A. Senatore, M. Basile, S. Knani, A. Basile, A. Iulianelli, *Membranes* **2018**, *8 (4)*. DOI: https://doi.org/10.3390/membranes8040098

[22] C. H. Bartholomew, R. J. Farrauto, *Fundamentals of Industrial Catalytic Processes*, 2nd ed., John Wiley & Sons, New York, NY **2011**.

[23] J. Bart, R. Sneeden, *Catalysis Today* **1987**, *2 (1)*, 1 – 124. DOI: https://doi.org/10.1016/0920-5861(87)80001-9

[24] R. Dalebout, N. L. Visser, C. L. Pompe, K. P. de Jong, P. E. de Jongh, *Journal of Catalysis* **2020**, *392*, 150 – 158. DOI: https://doi.org/10.1016/j.jcat.2020.10.006

[25] R. van den Berg, G. Prieto, G. Korpershoek, L. I. van der Wal, A. J. van Bunningen, S. Lægsgaard-Jørgensen, P. E. de Jongh, K. P. de Jong, *Nature communications* **2016**, *7*, 13057. DOI: https://doi.org/10.1038/ncomms13057

[26] E. S. Borovinskaya, S. Trebbin, F. Alscher, C. Breitkopf, *Catalysts* **2019**, *9 (12)*, 1037. DOI: https://doi.org/10.3390/catal9121037

[27] J. Xiao, D. Mao, X. Guo, J. Yu, *Energy Technology* **2015**, *3 (1)*, 32 – 39. DOI: https://doi.org/10.1002/ente.201402091

[28] S. Asthana, C. Samanta, A. Bhaumik, B. Banerjee, R. K. Voolapalli, B. Saha, *Journal of Catalysis* **2016**, *334*, 89 – 101. DOI: https://doi.org/10.1016/j.jcat.2015.10.020

[29] J. Du, Y. Zhang, K. Wang, F. Ding, S. Jia, G. Liu, L. Tan, *RSC advances* **2021**, *11 (24)*, 14426 – 14433. DOI: https://doi.org/10.1039/D0RA10849A

[30] F. Frusteri, M. Cordaro, C. Cannilla, G. Bonura, *Applied Catalysis B: Environmental* **2015**, *162*, 57 – 65. DOI: https://doi.org/10.1016/j.apcatb.2014.06.035

[31] K. Li, J. G. Chen, *ACS Catal.* **2019**, *9 (9)*, 7840 – 7861. DOI: https://doi.org/10.1021/acscatal.9b01943

[32] Y. Wang, S. Kattel, W. Gao, K. Li, P. Liu, J. G. Chen, H. Wang, *Nature communications* **2019**, *10 (1)*, 1166. DOI: https://doi.org/10.1038/s41467-019-09072-6

[33] G. Bonura, M. Cordaro, C. Cannilla, F. Arena, F. Frusteri, *Applied Catalysis B: Environmental* **2014**, *152-153*, 152 – 161. DOI: https://doi.org/10.1016/j.apcatb.2014.01.035

[34] F. Frusteri, G. Bonura, C. Cannilla, G. Drago Ferrante, A. Aloise, E. Catizzone, M. Migliori, G. Giordano, *Applied Catalysis B: Environmental* **2015**, *176-177*, 522 – 531. DOI: https://doi.org/10.1016/j.apcatb.2015.04.032

[35] S. Chang, W. Na, J. Zhang, L. Lin, W. Gao, *New J. Chem.* **2021**, *45 (48)*, 22814 – 22823. DOI: https://doi.org/10.1039/d1nj04951h

[36] F. Arena, G. Mezzatesta, G. Zafarana, G. Trunfio, F. Frusteri, L. Spadaro, *Catalysis Today* **2013**, *210*, 39 – 46. DOI: https://doi.org/10.1016/j.cattod.2013.02.016

[37] D. Jin, B. Zhu, Z. Hou, J. Fei, H. Lou, X. Zheng, *Fuel* **2007**, *86 (17-18)*, 2707 – 2713. DOI: https://doi.org/10.1016/j.fuel.2007.03.011

[38] W. Xiaoning, Z. Zhen, X. Chunming, D. Aijun, Z. Li, J. Guiyuan, *Journal of Rare Earths* **2007**, *25 (3)*, 321 – 328. DOI: https://doi.org/10.1016/S1002-0721(07)60430-X

[39] P. Gao, F. Li, N. Zhao, F. Xiao, W. Wei, L. Zhong, Y. Sun, *Applied Catalysis A: General* **2013**, *468*, 442 – 452. DOI: https://doi.org/10.1016/j.apcata.2013.09.026

[40] J. Nakamura, T. Uchijima, Y. Kanai, T. Fujitani, *Catalysis Today* **1996**, *28 (3)*, 223 – 230. DOI: https://doi.org/10.1016/0920-5861(95)00240-5

[41] T. Fujitani, J. Nakamura, *Applied Catalysis A: General* **2000**, *191 (1-2)*, 111 – 129. DOI: https://doi.org/10.1016/S0926-860X(99)00313-0

[42] T. Lunkenbein, J. Schumann, M. Behrens, R. Schlögl, M. G. Willinger, *Angewandte Chemie (International ed. in English)* **2015**, *54 (15)*, 4544 – 4548. DOI: https://doi.org/10.1002/anie.201411581

[43] K. Stangeland, H. Li, Z. Yu, *Energ. Ecol. Environ.* **2020**, *5 (4)*, 272 – 285. DOI: https://doi.org/10.1007/s40974-020-00156-4

[44] S. Kuld, C. Conradsen, P. G. Moses, I. Chorkendorff, J. Sehested, *Angewandte Chemie (International ed. in English)* **2014**, *53 (23)*, 5941 – 5945. DOI: https://doi.org/10.1002/anie.201311073

[45] J. Nakamura, *Top Catal* **2003**, *22 (3/4)*, 277 – 285. DOI: https://doi.org/10.1023/A:1023588322846

[46] D. Großmann, K. Klementiev, I. Sinev, W. Grünert, *ChemCatChem* **2017**, *9 (2)*, 365 – 372. DOI: https://doi.org/10.1002/cctc.201601102

[47] S. Kattel, P. J. Ramírez, J. G. Chen, J. A. Rodriguez, P. Liu, *Science (New York, N.Y.)* **2017**, *355 (6331)*, 1296 – 1299. DOI: https://doi.org/10.1126/science.aal3573

[48] I. Orozco, E. Huang, M. Mahapatra, J. Kang, R. Shi, S. Nemšák, X. Tong, S. D. Senanayake, P. Liu, J. A. Rodríguez, *J. Phys.*

Chem. C **2021**, *125 (12)*, 6673 – 6683. DOI: https://doi.org/10.1021/acs.jpcc.1c00392

[49] M. S. Frei, M. Capdevila-Cortada, R. García-Muelas, C. Mondelli, N. López, J. A. Stewart, D. Curulla Ferré, J. Pérez-Ramírez, *Journal of Catalysis* **2018**, *361*, 313 – 321. DOI: https://doi.org/10.1016/j.jcat.2018.03.014

[50] C. BALTES, S. VUKOJEVIC, F. SCHUTH, *Journal of Catalysis* **2008**, *258 (2)*, 334 – 344. DOI: https://doi.org/10.1016/j.jcat.2008.07.004

[51] S. Schimpf, M. Muhler, in *Synthesis of Solid Catalysts* (Eds: K. P. de Jong), Wiley-VCH Verlag GmbH & Co. KGaA. Weinheim, Germany **2009**.

[52] M. Behrens, S. Kissner, F. Girsgdies, I. Kasatkin, F. Hermerschmidt, K. Mette, H. Ruland, M. Muhler, R. Schlögl, *Chemical communications (Cambridge, England)* **2011**, *47 (6)*, 1701 – 1703. DOI: https://doi.org/10.1039/C0CC04933F

[53] N. Phongprueksathat, A. Bansode, T. Toyao, A. Urakawa, *RSC advances* **2021**, *11 (24)*, 14323 – 14333. DOI: https://doi.org/10.1039/D1RA02103F

[54] L. Li, D. Mao, J. Yu, X. Guo, *Journal of Power Sources* **2015**, *279*, 394 – 404. DOI: https://doi.org/10.1016/j.jpowsour.2014.12.142

[55] F. Arena, G. Italiano, K. Barbera, G. Bonura, L. Spadaro, F. Frusteri, *Catalysis Today* **2009**, *143 (1-2)*, 80 – 85. DOI: https://doi.org/10.1016/j.cattod.2008.11.022

[56] S. Natesakhawat, J. W. Lekse, J. P. Baltrus, P. R. Ohodnicki, B. H. Howard, X. Deng, C. Matranga, *ACS Catal.* **2012**, *2 (8)*, 1667 – 1676. DOI: https://doi.org/10.1021/cs300008g

[57] O. Martin, C. Mondelli, D. Curulla-Ferré, C. Drouilly, R. Hauert, J. Pérez-Ramírez, *ACS Catal.* **2015**, *5 (9)*, 5607 – 5616.

DOI: https://doi.org/10.1021/acscatal.5b00877

[58] J. Liu, J. Shi, D. He, Q. Zhang, X. Wu, Y. Liang, Q. Zhu, *Applied Catalysis A: General* **2001**, *218 (1-2)*, 113 – 119. DOI: https://doi.org/10.1016/S0926-860X(01)00625-1

[59] C. L. Carnes, K. J. Klabunde, *Journal of Molecular Catalysis A: Chemical* **2003**, *194 (1-2)*, 227 – 236. DOI: https://doi.org/10.1016/S1381-1169(02)00525-3

[60] J. SLOCZYNSKI, R. GRABOWSKI, P. OLSZEWSKI, A. KOZLOWSKA, J. STOCH, M. LACHOWSKA, J. SKRZYPEK, *Applied Catalysis A: General* **2006**, *310*, 127 – 137. DOI: https://doi.org/10.1016/j.apcata.2006.05.035

[61] X. Guo, D. Mao, G. Lu, S. Wang, G. Wu, *Journal of Catalysis* **2010**, *271 (2)*, 178 – 185. DOI: https://doi.org/10.1016/j.jcat.2010.01.009

[62] X. Guo, D. Mao, G. Lu, S. Wang, G. Wu, *Catalysis Communications* **2011**, *12 (12)*, 1095 – 1098. DOI: https://doi.org/10.1016/j.catcom.2011.03.033

[63] Z.-Q. Wang, Z.-N. Xu, S.-Y. Peng, M.-J. Zhang, G. Lu, Q.-S. Chen, Y. Chen, G.-C. Guo, *ACS Catal.* **2015**, *5 (7)*, 4255 – 4259. DOI: https://doi.org/10.1021/acscatal.5b00682

[64] N. J. Brown, A. García-Trenco, J. Weiner, E. R. White, M. Allinson, Y. Chen, P. P. Wells, E. K. Gibson, K. Hellgardt, M. S. P. Shaffer, C. K. Williams, *ACS Catal.* **2015**, *5 (5)*, 2895 – 2902. DOI: https://doi.org/10.1021/cs502038y

[65] S. Lee, K. Schneider, J. Schumann, A. K. Mogalicherla, P. Pfeifer, R. Dittmeyer, *Chemical Engineering Science* **2015**, *138*, 194 – 202. DOI: https://doi.org/10.1016/j.ces.2015.08.021

[66] W. Y. Teoh, R. Amal, L. Mädler, *Nanoscale* **2010**, *2 (8)*, 1324 – 1347. DOI: https://doi.org/10.1039/C0NR00017E

[67] R. Strobel, L. Mädler, M. Piacentini, M. Maciejewski, A. Baiker, S. E. Pratsinis, *Chem. Mater.* **2006**, *18 (10)*, 2532 – 2537. DOI: https://doi.org/10.1021/cm0600529

[68] J. Jensen, *Journal of Catalysis* **2003**, *218 (1)*, 67 – 77. DOI: https://doi.org/10.1016/S0021-9517(03)00047-2

[69] S. Tada, K. Larmier, R. Büchel, C. Copéret, *Catal. Sci. Technol.* **2018**, *8 (8)*, 2056 – 2060. DOI: https://doi.org/10.1039/C8CY00250A

[70] O. Martin, J. Pérez-Ramírez, *Catal. Sci. Technol.* **2013**, *3 (12)*, 3343. DOI: https://doi.org/10.1039/C3CY00573A

[71] M. B. Fichtl, D. Schlereth, N. Jacobsen, I. Kasatkin, J. Schumann, M. Behrens, R. Schlögl, O. Hinrichsen, *Applied Catalysis A: General* **2015**, *502*, 262 – 270. DOI: https://doi.org/10.1016/j.apcata.2015.06.014

[72] M. POUTSMA, *Journal of Catalysis* **1978**, *52 (1)*, 157 – 168. DOI: https://doi.org/10.1016/0021-9517(78)90131-8

[73] Y. Matsumura, W.-J. Shen, Y. Ichihashi, M. Okumura, *Journal of Catalysis* **2001**, *197 (2)*, 267 – 272. DOI: https://doi.org/10.1006/jcat.2000.3094

[74] O. A. Ojelade, S. F. Zaman, M. A. Daous, A. A. Al-Zahrani, A. S. Malik, H. Driss, G. Shterk, J. Gascon, *Applied Catalysis A: General* **2019**, *584*, 117185. DOI: https://doi.org/10.1016/j.apcata.2019.117185

[75] N. Rui, Z. Wang, K. Sun, J. Ye, Q. Ge, C. Liu, *Applied Catalysis B: Environmental* **2017**, *218*, 488 – 497. DOI: https://doi.org/10.1016/j.apcatb.2017.06.069

[76] H. Sakurai, M. Haruta, *Applied Catalysis A: General* **1995**, *127 (1-2)*, 93 – 105. DOI: https://doi.org/10.1016/0926-860X(95)00058-5

[77] Y. Hartadi, D. Widmann, R. J. Behm, *Physical chemistry chemical*

physics PCCP **2016**, *18 (16)*, 10781 – 10791. DOI: https://doi.org/10.1039/C5CP06888F

[78] P. Liu, J. K. Nørskov, *Phys. Chem. Chem. Phys.* **2001**, *3 (17)*, 3814 – 3818. DOI: https://doi.org/10.1039/b103525h

[79] M. Zabilskiy, V. L. Sushkevich, M. A. Newton, F. Krumeich, M. Nachtegaal, J. A. van Bokhoven, *Angewandte Chemie (International ed. in English)* **2021**, *60 (31)*, 17053 – 17059. DOI: https://doi.org/10.1002/anie.202103087

[80] H. Bahruji, M. Bowker, G. Hutchings, N. Dimitratos, P. Wells, E. Gibson, W. Jones, C. Brookes, D. Morgan, G. Lalev, *Journal of Catalysis* **2016**, *343*, 133 – 146. DOI: https://doi.org/10.1016/j.jcat.2016.03.017

[81] Y. Yin, B. Hu, X. Li, X. Zhou, X. Hong, G. Liu, *Applied Catalysis B: Environmental* **2018**, *234*, 143 – 152. DOI: https://doi.org/10.1016/j.apcatb.2018.04.024

[82] J. Díez-Ramírez, J. L. Valverde, P. Sánchez, F. Dorado, *Catal Lett* **2016**, *146 (2)*, 373 – 382. DOI: https://doi.org/10.1007/s10562-015-1627-z

[83] J. Díez-Ramírez, P. Sánchez, A. Rodríguez-Gómez, J. L. Valverde, F. Dorado, *Ind. Eng. Chem. Res.* **2016**, *55 (12)*, 3556 – 3567. DOI: https://doi.org/10.1021/acs.iecr.6b00170

[84] J. Xu, X. Su, X. Liu, X. Pan, G. Pei, Y. Huang, X. Wang, T. Zhang, H. Geng, *Applied Catalysis A: General* **2016**, *514*, 51 – 59. DOI: https://doi.org/10.1016/j.apcata.2016.01.006

[85] H. Bahruji, M. Bowker, W. Jones, J. Hayward, J. Ruiz Esquius, D. J. Morgan, G. J. Hutchings, *Faraday discussions* **2017**, *197*, 309 – 324. DOI: https://doi.org/10.1039/C6FD00189K

[86] O. Martin, A. J. Martín, C. Mondelli, S. Mitchell, T. F. Segawa, R. Hauert, C. Drouilly, D. Curulla-Ferré, J. Pérez-Ramírez,

Angewandte Chemie (International ed. in English) **2016**, *55 (21)*, 6261 – 6265. DOI: https://doi.org/10.1002/anie.201600943

[87] J. Ye, C. Liu, D. Mei, Q. Ge, *ACS Catal.* **2013**, *3 (6)*, 1296 – 1306. DOI: https://doi.org/10.1021/cs400132a

[88] S. Dang, B. Qin, Y. Yang, H. Wang, J. Cai, Y. Han, S. Li, P. Gao, Y. Sun, *Science advances* **2020**, *6 (25)*, eaaz2060. DOI: https://doi.org/10.1126/sciadv.aaz2060

[89] T. Chen, C. Cao, T. Chen, X. Ding, H. Huang, L. Shen, X. Cao, M. Zhu, J. Xu, J. Gao, Y.-F. Han, *ACS Catal.* **2019**, *9 (9)*, 8785 – 8797. DOI: https://doi.org/10.1021/acscatal.9b01869

[90] M. S. Frei, C. Mondelli, A. Cesarini, F. Krumeich, R. Hauert, J. A. Stewart, D. Curulla Ferré, J. Pérez-Ramírez, *ACS Catal.* **2020**, *10 (2)*, 1133 – 1145. DOI: https://doi.org/10.1021/acscatal.9b03305

[91] A. Tsoukalou, P. M. Abdala, A. Armutlulu, E. Willinger, A. Fedorov, C. R. Müller, *ACS Catal.* **2020**, *10 (17)*, 10060 – 10067. DOI: https://doi.org/10.1021/acscatal.0c01968

[92] J. L. Snider, V. Streibel, M. A. Hubert, T. S. Choksi, E. Valle, D. C. Upham, J. Schumann, M. S. Duyar, A. Gallo, F. Abild-Pedersen, T. F. Jaramillo, *ACS Catal.* **2019**, *9 (4)*, 3399 – 3412. DOI: https://doi.org/10.1021/acscatal.8b04848

[93] M. S. Frei, C. Mondelli, R. García-Muelas, K. S. Kley, B. Puértolas, N. López, O. V. Safonova, J. A. Stewart, D. Curulla Ferré, J. Pérez-Ramírez, *Nature communications* **2019**, *10 (1)*, 3377. DOI: https://doi.org/10.1038/s41467-019-11349-9

[94] Z. Han, C. Tang, J. Wang, L. Li, C. Li, *Journal of Catalysis* **2021**, *394*, 236 – 244. DOI: https://doi.org/10.1016/j.jcat.2020.06.018

[95] M. M.-J. Li, H. Zou, J. Zheng, T.-S. Wu, T.-S. Chan, Y.-L. Soo, X.-P. Wu, X.-Q. Gong, T. Chen, K. Roy, G. Held, S. C. E. Tsang,

Angewandte Chemie (International ed. in English) **2020**, *59 (37)*, 16039 – 16046. DOI: https://doi.org/10.1002/anie.202000841

[96] C. Liu, J. Kang, Z.-Q. Huang, Y.-H. Song, Y.-S. Xiao, J. Song, J.-X. He, C.-R. Chang, H.-Q. Ge, Y. Wang, Z.-T. Liu, Z.-W. Liu, *Nature communications* **2021**, *12 (1)*, 2305. DOI: https://doi.org/10.1038/s41467-021-22568-4

[97] S. COLLINS, M. BALTANAS, A. BONIVARDI, *Journal of Catalysis* **2004**, *226 (2)*, 410 – 421. DOI: https://doi.org/10.1016/j.jcat.2004.06.012

[98] F. Studt, I. Sharafutdinov, F. Abild-Pedersen, C. F. Elkjær, J. S. Hummelshøj, S. Dahl, I. Chorkendorff, J. K. Nørskov, *Nature chemistry* **2014**, *6 (4)*, 320 – 324. DOI: https://doi.org/10.1038/nchem.1873

[99] M. Ding, R. W. Flaig, H.-L. Jiang, O. M. Yaghi, *Chemical Society reviews* **2019**, *48 (10)*, 2783 – 2828. DOI: https://doi.org/10.1039/C8CS00829A

[100] B. Liang, J. Ma, X. Su, C. Yang, H. Duan, H. Zhou, S. Deng, L. Li, Y. Huang, *Ind. Eng. Chem. Res.* **2019**, *58 (21)*, 9030 – 9037. DOI: https://doi.org/10.1021/acs.iecr.9b01546

[101] B. Hu, Y. Yin, Z. Zhong, D. Wu, G. Liu, X. Hong, *Catal. Sci. Technol.* **2019**, *9 (10)*, 2673 – 2681. DOI: https://doi.org/10.1039/C8CY02546K

[102] T. Liu, X. Hong, G. Liu, *ACS Catal.* **2020**, *10 (1)*, 93 – 102. DOI: https://doi.org/10.1021/acscatal.9b03738

[103] X. San, X. Gong, Y. Hu, Y. Hu, G. Wang, J. Qi, D. Meng, Q. Jin, *ChemistrySelect* **2021**, *6 (24)*, 6115 – 6118. DOI: https://doi.org/10.1002/slct.202101179

[104] S. S. Iyer, T. Renganathan, S. Pushpavanam, M. Vasudeva Kumar, N. Kaisare, *Journal of CO2 Utilization* **2015**, *10*, 95 – 104.

DOI: https://doi.org/10.1016/j.jcou.2015.01.006

[105] G. H. Graaf, E. J. Stamhuis, A. Beenackers, *Chemical Engineering Science* **1988**, *43 (12)*, 3185 – 3195. DOI: https://doi.org/10.1016/0009-2509(88)85127-3

[106] K. Bussche, G. F. Froment, *Journal of Catalysis* **1996**, *161 (1)*, 1 – 10. DOI: https://doi.org/10.1006/jcat.1996.0156

[107] C. Seidel, A. Jörke, B. Vollbrecht, A. Seidel-Morgenstern, A. Kienle, *Chemical Engineering Science* **2018**, *175*, 130 – 138. DOI: https://doi.org/10.1016/j.ces.2017.09.043

[108] Y. Slotboom, M. J. Bos, J. Pieper, V. Vrieswijk, B. Likozar, S. Kersten, D. Brilman, *Chemical Engineering Journal* **2020**, *389*, 124181. DOI: https://doi.org/10.1016/j.cej.2020.124181

[109] F. Nestler, V. P. Müller, M. Ouda, M. J. Hadrich, A. Schaadt, S. Bajohr, T. Kolb, *React. Chem. Eng.* **2021**, *6 (6)*, 1092 – 1107. DOI: https://doi.org/10.1039/D1RE00071C

[110] L. C. Grabow, M. Mavrikakis, *ACS Catal.* **2011**, *1 (4)*, 365 – 384. DOI: https://doi.org/10.1021/cs200055d

[111] J. Park, J. Cho, Y. Lee, M.-J. Park, W. B. Lee, *Ind. Eng. Chem. Res.* **2019**, *58 (20)*, 8663 – 8673. DOI: https://doi.org/10.1021/acs.iecr.9b01254

[112] D. Xu, P. Wu, B. Yang, *J. Phys. Chem. C* **2019**, *123 (14)*, 8959 – 8966. DOI: https://doi.org/10.1021/acs.jpcc.8b12460

[113] M. Huš, D. Kopač, N. S. Štefančič, D. L. Jurković, V. D. B. C. Dasireddy, B. Likozar, *Catal. Sci. Technol.* **2017**, *7 (24)*, 5900 – 5913. DOI: https://doi.org/10.1039/C7CY01659J

[114] B. Lacerda de Oliveira Campos, K. Herrera Delgado, S. Wild, F. Studt, S. Pitter, J. Sauer, *React. Chem. Eng.* **2021**, *6 (5)*, 868 – 887. DOI: https://doi.org/10.1039/D1RE00040C

[115] F. Studt, M. Behrens, E. L. Kunkes, N. Thomas, S. Zander, A.

Tarasov, J. Schumann, E. Frei, J. B. Varley, F. Abild-Pedersen, J. K. Nørskov, R. Schlögl, *ChemCatChem* **2015**, *7 (7)*, 1105 – 1111. DOI: https://doi.org/10.1002/cctc.201500123

[116] Y.-M. Liu, J.-T. Liu, S.-Z. Liu, J. Li, Z.-H. Gao, Z.-J. Zuo, W. Huang, *Journal of CO2 Utilization* **2017**, *20*, 59 – 65. DOI: https://doi.org/10.1016/j.jcou.2017.05.005

[117] L. P. de Oliveira, D. Hudebine, D. Guillaume, J. J. Verstraete, *Oil Gas Sci. Technol. – Rev. IFP Energies nouvelles* **2016**, *71 (3)*, 45. DOI: https://doi.org/10.2516/ogst/2016011

[118] M. Salciccioli, M. Stamatakis, S. Caratzoulas, D. G. Vlachos, *Chemical Engineering Science* **2011**, *66 (19)*, 4319 – 4355. DOI: https://doi.org/10.1016/j.ces.2011.05.050

[119] J.-D. Grunwaldt, A. Molenbroek, N.-Y. Topsøe, H. Topsøe, B. Clausen, *Journal of Catalysis* **2000**, *194 (2)*, 452 – 460. DOI: https://doi.org/10.1006/jcat.2000.2930

[120] Y. Choi, K. Futagami, T. Fujitani, J. Nakamura, *Catal Lett* **2001**, *73 (1)*, 27 – 31. DOI: https://doi.org/10.1023/A:1009074219286

[121] L. Pandit, A. Boubnov, G. Behrendt, B. Mockenhaupt, C. Chowdhury, J. Jelic, A.-L. Hansen, E. Saraçi, E.-J. Ras, M. Behrens, F. Studt, J.-D. Grunwaldt, *ChemCatChem* **2021**, *13 (19)*, 4120 – 4132. DOI: https://doi.org/10.1002/cctc.202100692

[122] K. F. Kalz, R. Kraehnert, M. Dvoyashkin, R. Dittmeyer, R. Gläser, U. Krewer, K. Reuter, J.-D. Grunwaldt, *ChemCatChem* **2017**, *9 (1)*, 17 – 29. DOI: https://doi.org/10.1002/cctc.201600996

[123] J. Schumann, J. Kröhnert, E. Frei, R. Schlögl, A. Trunschke, *Top Catal* **2017**, *60 (19-20)*, 1735 – 1743. DOI: https://doi.org/10.1007/s11244-017-0850-9

[124] S. M. Fehr, I. Krossing, *ChemCatChem* **2020**, *12 (9)*, 2622 – 2629. DOI: https://doi.org/10.1002/cctc.201902038

[125] A. Pavlišič, M. Huš, A. Prašnikar, B. Likozar, *Journal of Cleaner Production* **2020**, *275*, 122958. DOI: https://doi.org/10.1016/j.jclepro.2020.122958

[126] T. H. Fleisch, A. Basu, R. A. Sills, *Journal of Natural Gas Science and Engineering* **2012**, *9*, 94 – 107. DOI: https://doi.org/10.1016/j.jngse.2012.05.012

[127] A. Akhoondi, A. I. Osman, A. Alizadeh Eslami, *Synth. Sinter.* **2021**, *1 (2)*, 105 – 125. DOI: https://doi.org/10.53063/synsint.2021.1229

[128] I. Kiendl, H. Schmaderer, N. Schödel, H. Klein, *Chemie Ingenieur Technik* **2020**, *92 (6)*, 736 – 745. DOI: https://doi.org/10.1002/cite.201900164

[129] W. P. M. van Swaaij, S. R. A. Kersten, W. Palz, *Biomass power for the world*, 1st ed., Pan Stanford Publishing, Singapore **2015**.

[130] A. Ateka, P. Pérez-Uriarte, M. Gamero, J. Ereña, A. T. Aguayo, J. Bilbao, *Energy* **2017**, *120*, 796 – 804. DOI: https://doi.org/10.1016/j.energy.2016.11.129

[131] G. Jia, Y. Tan, Y. Han, *Ind. Eng. Chem. Res.* **2006**, *45 (3)*, 1152 – 1159. DOI: https://doi.org/10.1021/ie050499b

[132] F. Dadgar, R. Myrstad, P. Pfeifer, A. Holmen, H. J. Venvik, *Catalysis Today* **2016**, *270*, 76 – 84. DOI: https://doi.org/10.1016/j.cattod.2015.09.024

[133] M. Sánchez-Contador, A. Ateka, M. Ibáñez, J. Bilbao, A. T. Aguayo, *Renewable Energy* **2019**, *138*, 585 – 597. DOI: https://doi.org/10.1016/j.renene.2019.01.093

[134] F. J. Keil, *Reviews in Chemical Engineering* **2018**, *34 (2)*, 135 – 200. DOI: https://doi.org/10.1515/revce-2017-0085

[135] V. Hessel, *Micro process engineering: A comprehensive handbook / edited by Volker Hessel … [et al.]*, Wiley-VCH; [Chichester John

Wiley, Weinheim **2009**.

[136] P. Peter, in *Chemical Kinetics* (Eds: V. Patel), InTech **2012**.

[137] M. Fichtner, J. Mayer, D. Wolf, K. Schubert, *Ind. Eng. Chem. Res.* **2001**, *40 (16)*, 3475 – 3483. DOI: https://doi.org/10.1021/ie000967b

[138] A. Kursawe, D. Hönicke, *Catalysis Communications* **2001**, *2 (11-12)*, 347 – 351. DOI: https://doi.org/10.1016/S1566-7367(01)00057-7

[139] P. Liu, B. Zhao, S. Li, H. Shi, M. Ma, J. Lu, F. Yang, X. Deng, X. Jia, X. Ma, X. Yan, *Ind. Eng. Chem. Res.* **2020**, *59 (5)*, 1845 – 1854. DOI: https://doi.org/10.1021/acs.iecr.9b05951

[140] H. Kirsch, N. Lochmahr, C. Staudt, P. Pfeifer, R. Dittmeyer, *Chemical Engineering Journal* **2020**, *393*, 124553. DOI: https://doi.org/10.1016/j.cej.2020.124553

[141] J. Hu, Y. Wang, C. Cao, D. C. Elliott, D. J. Stevens, J. F. White, *Ind. Eng. Chem. Res.* **2005**, *44 (6)*, 1722 – 1727. DOI: https://doi.org/10.1021/ie0492707

[142] S. Allahyari, M. Haghighi, A. Ebadi, *Chemical Engineering Journal* **2015**, *262*, 1175 – 1186. DOI: https://doi.org/10.1016/j.cej.2014.10.062

[143] S. Baroutian, M. K. Aroua, A. A. A. Raman, N. M. N. Sulaiman, *Bioresource technology* **2011**, *102 (2)*, 1095 – 1102. DOI: https://doi.org/10.1016/j.biortech.2010.08.076

[144] R. Bedard, C. Liu, *Annu. Rev. Mater. Res.* **2018**, *48 (1)*, 83 – 110. DOI: https://doi.org/10.1146/annurev-matsci-070317-124605

[145] S.-J. Kim, P. S. Lee, M.-J. Park, D.-W. Lee, Y.-I. Park, S.-E. Nam, K.-H. Lee, *Separation Science and Technology* **2016**, *51 (12)*, 2062 – 2069. DOI: https://doi.org/10.1080/01496395.2016.1198378

[146] H. H. Koybasi, A. K. Avci, *Catalysis Today* **2022**, *383*, 133 – 145. DOI: https://doi.org/10.1016/j.cattod.2020.10.020

[147] I. Iliuta, F. Larachi, P. Fongarland, *Ind. Eng. Chem. Res.* **2010**, *49 (15)*, 6870 – 6877. DOI: https://doi.org/10.1021/ie901726u

[148] H. Li, S. Ren, S. Zhang, S. Padinjarekutt, B. Sengupta, X. Liang, S. Li, M. Yu, *J. Mater. Chem. A* **2021**, *9 (5)*, 2678 – 2682. DOI: https://doi.org/10.1039/D0TA10417E

[149] M. A. Scibioh, B. Viswanathan, *Carbon dioxide to chemicals and fuels*, Elsevier, Amsterdam **2018**.

[150] F. Gallucci, L. Paturzo, A. Basile, *Chemical Engineering and Processing: Process Intensification* **2004**, *43 (8)*, 1029 – 1036. DOI: https://doi.org/10.1016/j.cep.2003.10.005

[151] J. Gorbe, J. Lasobras, E. Francés, J. Herguido, M. Menéndez, I. Kumakiri, H. Kita, *Separation and Purification Technology* **2018**, *200*, 164 – 168. DOI: https://doi.org/10.1016/j.seppur.2018.02.036

[152] A. Brunetti, M. Migliori, D. Cozza, E. Catizzone, G. Giordano, G. Barbieri, *ACS Sustainable Chem. Eng.* **2020**, *8 (28)*, 10471 – 10479. DOI: https://doi.org/10.1021/acssuschemeng.0c02557

[153] P. Rodriguez-Vega, A. Ateka, I. Kumakiri, H. Vicente, J. Ereña, A. T. Aguayo, J. Bilbao, *Chemical Engineering Science* **2021**, *234*, 116396. DOI: https://doi.org/10.1016/j.ces.2020.116396

[154] Z. Li, Y. Deng, N. Dewangan, J. Hu, Z. Wang, X. Tan, S. Liu, S. Kawi, *Chemical Engineering Journal* **2021**, *420*, 129834. DOI: https://doi.org/10.1016/j.cej.2021.129834

[155] N. Delgado Otalvaro, M. Kaiser, K. Herrera Delgado, S. Wild, J. Sauer, H. Freund, *React. Chem. Eng.* **2020**, *5 (5)*, 949 – 960. DOI: https://doi.org/10.1039/D0RE00041H

[156] R. Peláez, P. Marín, S. Ordóñez, *Fuel Processing Technology* **2017**, *168*, 40 – 49. DOI: https://doi.org/10.1016/j.fuproc.2017.09.004

[157] S. Guffanti, C. G. Visconti, G. Groppi, *Ind. Eng. Chem. Res.* **2021**, *60 (18)*, 6767 – 6783. DOI: https://doi.org/10.1021/acs.iecr.1c00521

[158] G. Bercic, J. Levec, *Ind. Eng. Chem. Res.* **1993**, *32 (11)*, 2478 – 2484. DOI: https://doi.org/10.1021/ie00023a006

[159] M. Mollavali, F. Yaripour, H. Atashi, S. Sahebdelfar, *Ind. Eng. Chem. Res.* **2008**, *47 (9)*, 3265 – 3273. DOI: https://doi.org/10.1021/ie800051h

[160] W.-Z. Lu, L.-H. Teng, W.-D. Xiao, *Chemical Engineering Science* **2004**, *59 (22-23)*, 5455 – 5464. DOI: https://doi.org/10.1016/j.ces.2004.07.031

[161] J. Park, H. S. Kim, W. B. Lee, M.-J. Park, *Catalysts* **2020**, *10 (6)*, 655. DOI: https://doi.org/10.3390/catal10060655

[162] J. Park, J. Cho, M.-J. Park, W. B. Lee, *Catalysis Today* **2021**, *375*, 314 – 323. DOI: https://doi.org/10.1016/j.cattod.2020.02.011

[163] P. N. Plessow, F. Studt, *ACS Catal.* **2017**, *7 (11)*, 7987 – 7994. DOI: https://doi.org/10.1021/acscatal.7b03114

[164] A. J. Jones, E. Iglesia, *Angewandte Chemie (International ed. in English)* **2014**, *53 (45)*, 12177 – 12181. DOI: https://doi.org/10.1002/anie.201406823

[165] N. Delgado Otalvaro, P. Gül Bilir, K. Herrera Delgado, S. Pitter, J. Sauer, *Chemie Ingenieur Technik* **2021**, *93 (5)*, 754 – 761. DOI: https://doi.org/10.1002/cite.202000226

[166] J. Mohd Ali, M. A. Hussain, M. O. Tade, J. Zhang, *Expert Systems with Applications* **2015**, *42 (14)*, 5915 – 5931. DOI: https://doi.org/10.1016/j.eswa.2015.03.023

[167] M. Negnevitsky, V. Pavlovsky, *IEEE Trans. Power Delivery*

2005, *20 (2)*, 588 – 594. DOI: https://doi.org/10.1109/tpwrd.2004.843451

[168] P. Valeh-e-Sheyda, F. Yaripour, G. Moradi, M. Saber, *Ind. Eng. Chem. Res.* **2010**, *49 (10)*, 4620 – 4626. DOI: https://doi.org/10.1021/ie9020705

[169] S. Alamolhoda, M. Kazemeini, A. Zaherian, M. R. Zakerinasab, *Journal of Industrial and Engineering Chemistry* **2012**, *18 (6)*, 2059 – 2068. DOI: https://doi.org/10.1016/j.jiec.2012.05.027

[170] K. Omata, T. Ozaki, T. Umegaki, Y. Watanabe, N. Nukui, M. Yamada, *Energy Fuels* **2003**, *17 (4)*, 836 – 841. DOI: https://doi.org/10.1021/ef0202438

[171] K. Omata, Sutarto, M. Hashimoto, G. Ishiguro, Y. Watanabe, T. Umegaki, M. Yamada, *Ind. Eng. Chem. Res.* **2006**, *45 (14)*, 4905 – 4910. DOI: https://doi.org/10.1021/ie050640g

[172] G. R. Moradi, F. Parvizian, *Can. J. Chem. Eng.* **2011**, *89 (5)*, 1266 – 1273. DOI: https://doi.org/10.1002/cjce.20558

[173] F. S. Ramos, A. D. de Farias, L. Borges, J. L. Monteiro, M. A. Fraga, E. F. Sousa-Aguiar, L. G. Appel, *Catalysis Today* **2005**, *101 (1)*, 39 – 44. DOI: https://doi.org/10.1016/j.cattod.2004.12.007

[174] R. Ahmad, M. Hellinger, M. Buchholz, H. Sezen, L. Gharnati, C. Wöll, J. Sauer, M. Döring, J.-D. Grunwaldt, U. Arnold, *Catalysis Communications* **2014**, *43*, 52 – 56. DOI: https://doi.org/10.1016/j.catcom.2013.08.020

[175] K. Saravanan, H. Ham, N. Tsubaki, J. W. Bae, *Applied Catalysis B: Environmental* **2017**, *217*, 494 – 522. DOI: https://doi.org/10.1016/j.apcatb.2017.05.085

[176] A. García-Trenco, A. Martínez, *Applied Catalysis A: General* **2015**, *493*, 40 – 49. DOI: https://doi.org/10.1016/j.apcata.2015.01.007

[177] M. Gentzen, W. Habicht, D. E. Doronkin, J.-D. Grunwaldt, J. Sauer, S. Behrens, *Catal. Sci. Technol.* **2016**, *6 (4)*, 1054 – 1063. DOI: https://doi.org/10.1039/C5CY01043H

[178] K. Bizon, K. Skrzypek-Markiewicz, D. Pędzich, N. Reczek, *Catalysts* **2019**, *9 (12)*, 1020. DOI: https://doi.org/10.3390/catal9121020

[179] M. Cai, V. Subramanian, V. V. Sushkevich, V. V. Ordomsky, A. Y. Khodakov, *Applied Catalysis A: General* **2015**, *502*, 370 – 379. DOI: https://doi.org/10.1016/j.apcata.2015.06.030

[180] A. Ateka, I. Sierra, J. Ereña, J. Bilbao, A. T. Aguayo, *Fuel Processing Technology* **2016**, *152*, 34 – 45. DOI: https://doi.org/10.1016/j.fuproc.2016.05.041

[181] J. Ereña, R. Garoña, J. M. Arandes, A. T. Aguayo, J. Bilbao, *International Journal of Chemical Reactor Engineering* **2005**, *3 (1)*. DOI: https://doi.org/10.2202/1542-6580.1295

[182] H. Jiang, H. Bongard, W. Schmidt, F. Schüth, *Microporous and Mesoporous Materials* **2012**, *164*, 3 – 8. DOI: https://doi.org/10.1016/j.micromeso.2012.08.004

[183] G. Baracchini, A. G. Machoke, M. Klumpp, R. Wen, P. Arnold, W. Schwieger, R. Dittmeyer, *Catalysis Today* **2020**, *342*, 46 – 58. DOI: https://doi.org/10.1016/j.cattod.2019.07.016

[184] X. Fang, H. Jia, B. Zhang, Y. Li, Y. Wang, Y. Song, T. Du, L. Liu, *Journal of Environmental Chemical Engineering* **2021**, *9 (4)*, 105299. DOI: https://doi.org/10.1016/j.jece.2021.105299

[185] G. R. Moradi, S. Nosrati, F. Yaripor, *Catalysis Communications* **2007**, *8 (3)*, 598 – 606. DOI: https://doi.org/10.1016/j.catcom.2006.08.023

[186] A. García-Trenco, A. Vidal-Moya, A. Martínez, *Catalysis Today* **2012**, *179 (1)*, 43 – 51.

DOI: https://doi.org/10.1016/j.cattod.2011.06.034

[187] R. Khoshbin, M. Haghighi, *Catal. Sci. Technol.* **2014**, *4 (6)*, 1779 – 1792. DOI: https://doi.org/10.1039/C3CY01089A

[188] B. Voss, A. Katerinopoulou, R. Montesano, J. Sehested, *Chemical Engineering Journal* **2019**, *377*, 121940. DOI: https://doi.org/10.1016/j.cej.2019.121940

[189] G. Bonura, S. Todaro, L. Frusteri, I. Majchrzak-Kucęba, D. Wawrzyńczak, Z. Pászti, E. Tálas, A. Tompos, L. Ferenc, H. Solt, C. Cannilla, F. Frusteri, *Applied Catalysis B: Environmental* **2021**, *294*, 120255. DOI: https://doi.org/10.1016/j.apcatb.2021.120255

[190] K. S. Yoo, J.-H. Kim, M.-J. Park, S.-J. Kim, O.-S. Joo, K.-D. Jung, *Applied Catalysis A: General* **2007**, *330*, 57 – 62. DOI: https://doi.org/10.1016/j.apcata.2007.07.007

[191] J. Abu-Dahrieh, D. Rooney, A. Goguet, Y. Saih, *Chemical Engineering Journal* **2012**, *203*, 201 – 211. DOI: https://doi.org/10.1016/j.cej.2012.07.011

[192] J. Ereña, I. Sierra, M. Olazar, A. G. Gayubo, A. T. Aguayo, *Ind. Eng. Chem. Res.* **2008**, *47 (7)*, 2238 – 2247. DOI: https://doi.org/10.1021/ie071478f

[193] V. V. Ordomsky, M. Cai, V. Sushkevich, S. Moldovan, O. Ersen, C. Lancelot, V. Valtchev, A. Y. Khodakov, *Applied Catalysis A: General* **2014**, *486*, 266 – 275. DOI: https://doi.org/10.1016/j.apcata.2014.08.030

[194] M. Migliori, A. Condello, F. Dalena, E. Catizzone, G. Giordano, *Catalysts* **2020**, *10 (6)*, 671. DOI: https://doi.org/10.3390/catal10060671

[195] G. Bonura, M. Cordaro, L. Spadaro, C. Cannilla, F. Arena, F. Frusteri, *Applied Catalysis B: Environmental* **2013**, *140-141*,

16 – 24. DOI: https://doi.org/10.1016/j.apcatb.2013.03.048

[196] R. Nie, H. Lei, S. Pan, L. Wang, J. Fei, Z. Hou, *Fuel* **2012**, *96*, 419 – 425. DOI: https://doi.org/10.1016/j.fuel.2011.12.048

[197] G. Yang, N. Tsubaki, J. Shamoto, Y. Yoneyama, Y. Zhang, *Journal of the American Chemical Society* **2010**, *132 (23)*, 8129 – 8136. DOI: https://doi.org/10.1021/ja101882a

[198] S. Baier, C. D. Damsgaard, M. Klumpp, J. Reinhardt, T. Sheppard, Z. Balogh, T. Kasama, F. Benzi, J. B. Wagner, W. Schwieger, C. G. Schroer, J.-D. Grunwaldt, *Microscopy and microanalysis the official journal of Microscopy Society of America, Microbeam Analysis Society, Microscopical Society of Canada* **2017**, *23 (3)*, 501 – 512. DOI: https://doi.org/10.1017/S1431927617000332

[199] T. L. Sheppard, S. W. T. Price, F. Benzi, S. Baier, M. Klumpp, R. Dittmeyer, W. Schwieger, J.-D. Grunwaldt, *Journal of the American Chemical Society* **2017**, *139 (23)*, 7855 – 7863. DOI: https://doi.org/10.1021/jacs.7b02177

[200] G. Yang, M. Thongkam, T. Vitidsant, Y. Yoneyama, Y. Tan, N. Tsubaki, *Catalysis Today* **2011**, *171 (1)*, 229 – 235. DOI: https://doi.org/10.1016/j.cattod.2011.02.021

[201] R. Phienluphon, K. Pinkaew, G. Yang, J. Li, Q. Wei, Y. Yoneyama, T. Vitidsant, N. Tsubaki, *Chemical Engineering Journal* **2015**, *270*, 605 – 611. DOI: https://doi.org/10.1016/j.cej.2015.02.071

[202] G. Baracchini, M. Klumpp, P. Arnold, R. Dittmeyer, *Chemical Engineering Journal* **2020**, *396*, 125155. DOI: https://doi.org/10.1016/j.cej.2020.125155

[203] S. Guffanti, C. G. Visconti, G. Groppi, *Ind. Eng. Chem. Res.* **2020**, *59 (32)*, 14252 – 14266.

DOI: https://doi.org/10.1021/acs.iecr.0c01938

[204] W. Ding, M. Klumpp, S. Lee, S. Reuß, S. A. Al-Thabaiti, P. Pfeifer, W. Schwieger, R. Dittmeyer, *Chemie Ingenieur Technik* **2015**, *87 (6)*, 702 – 712. DOI: https://doi.org/10.1002/cite.201400157

[205] A. Ateka, A. Portillo, M. Sánchez-Contador, J. Bilbao, A. T. Aguayo, *Renewable Energy* **2021**, *169*, 1242 – 1251. DOI: https://doi.org/10.1016/j.renene.2021.01.062

[206] B. Li, Y. Liu, Y. Guo, D. Yang, D. Yang, P. Ming, C. Zhang, *International Journal of Hydrogen Energy* **2021**, *46 (63)*, 32215 – 32225. DOI: https://doi.org/10.1016/j.ijhydene.2021.06.216

[207] S. Kamiya, M. Yamada, M. Washino, K. Nakashima, *Current nanoscience* **2018**, *14 (2)*, 143 – 147. DOI: https://doi.org/10.2174/1573413713666171109155955

[208] R. Zhao, Y. Han, M. He, Y. Li, *Powder Technology* **2017**, *305*, 418 – 425. DOI: https://doi.org/10.1016/j.powtec.2016.07.050

[209] A. Saheki, J. Seki, T. Nakanishi, I. Tamai, *International journal of pharmaceutics* **2012**, *422 (1-2)*, 489 – 494. DOI: https://doi.org/10.1016/j.ijpharm.2011.10.060

[210] B. G. Pollet, J. T. Goh, *Electrochimica Acta* **2014**, *128*, 292 – 303. DOI: https://doi.org/10.1016/j.electacta.2013.09.160

[211] M. Wang, J. H. Park, S. Kabir, K. C. Neyerlin, N. N. Kariuki, H. Lv, V. R. Stamenkovic, D. J. Myers, M. Ulsh, S. A. Mauger, *ACS Appl. Energy Mater.* **2019**, *2 (9)*, 6417 – 6427. DOI: https://doi.org/10.1021/acsaem.9b01037

[212] R. Xiang, H. Zeng, Y. Su, X. Gui, T. Wu, E. Einarsson, S. Maruyama, Z. Tang, *Carbon* **2013**, *64*, 537 – 540. DOI: https://doi.org/10.1016/j.carbon.2013.07.034

[213] M. Ben-Naim, D. W. Palm, A. L. Strickler, A. C. Nielander, J. Sanchez, L. A. King, D. C. Higgins, T. F. Jaramillo, *ACS applied materials & interfaces* **2020**, *12 (5)*, 5901 – 5908. DOI: https://doi.org/10.1021/acsami.9b20099

[214] M. Mandal, A. Valls, N. Gangnus, M. Secanell, *J. Electrochem. Soc.* **2018**, *165 (7)*, F543-F552. DOI: https://doi.org/10.1149/2.1101807jes

[215] W. Wang, S. Chen, J. Li, W. Wang, *International Journal of Hydrogen Energy* **2015**, *40 (13)*, 4649 – 4658. DOI: https://doi.org/10.1016/j.ijhydene.2015.02.027

[216] H.-W. Lin, C.-P. Chang, W.-H. Hwu, M.-D. Ger, *Journal of Materials Processing Technology* **2008**, *197 (1-3)*, 284 – 291. DOI: https://doi.org/10.1016/j.jmatprotec.2007.06.067

[217] P. Ried, C. Lorenz, A. Brönstrup, T. Graule, N. H. Menzler, W. Sitte, P. Holtappels, *Journal of the European Ceramic Society* **2008**, *28 (9)*, 1801 – 1808. DOI: https://doi.org/10.1016/j.jeurceramsoc.2007.11.018

[218] A. Sanson, E. Roncari, S. Boldrini, P. Mangifesta, L. Doubova, *Journal of Fuel Cell Science and Technology* **2010**, *7 (5)*. DOI: https://doi.org/10.1115/1.3120271

[219] S. Ito, T. N. Murakami, P. Comte, P. Liska, C. Grätzel, M. K. Nazeeruddin, M. Grätzel, *Thin Solid Films* **2008**, *516 (14)*, 4613 – 4619. DOI: https://doi.org/10.1016/j.tsf.2007.05.090

[220] S. Ito, M. K. Nazeeruddin, S. M. Zakeeruddin, P. Péchy, P. Comte, M. Grätzel, T. Mizuno, A. Tanaka, T. Koyanagi, *International Journal of Photoenergy* **2009**, *2009*, 1 – 8. DOI: https://doi.org/10.1155/2009/517609

[221] V. Zardetto, F. Di Giacomo, D. Garcia-Alonso, W. Keuning, M. Creatore, C. Mazzuca, A. Reale, A. Di Carlo, T. M. Brown, *Adv.*

Energy Mater. **2013**, *3 (10)*, 1292 – 1298. DOI: https://doi.org/10.1002/aenm.201300101

[222] G. Baracchini, *Optimization of layered bifunctional catalytic systems for one-step synthesis of dimethyl ether*, Dissertation, IMVT **2020**.

[223] R. Zapf, G. Kolb, H. Pennemann, V. Hessel, *Chem. Eng. Technol.* **2006**, *29 (12)*, 1509 – 1512. DOI: https://doi.org/10.1002/ceat.200600204

[224] G. CHINCHEN, *Journal of Catalysis* **1987**, *103 (1)*, 79 – 86. DOI: https://doi.org/10.1016/0021-9517(87)90094-7

[225] Y. H. Wang, W. G. Gao, H. Wang, Y. E. Zheng, W. Na, K. Z. Li, *RSC Adv.* **2017**, *7 (14)*, 8709 – 8717. DOI: https://doi.org/10.1039/C6RA28305E

[226] T. Witoon, J. Chalorngtham, P. Dumrongbunditkul, M. Chareonpanich, J. Limtrakul, *Chemical Engineering Journal* **2016**, *293*, 327 – 336. DOI: https://doi.org/10.1016/j.cej.2016.02.069

[227] R. GRABOWSKI, J. Słoczyński, M. Śliwa, D. Mucha, R. P. Socha, M. LACHOWSKA, J. SKRZYPEK, *ACS Catal.* **2011**, *1 (4)*, 266 – 278. DOI: https://doi.org/10.1021/cs100033v

[228] X. Zhou, T. Su, Y. Jiang, Z. Qin, H. Ji, Z. Guo, *Chemical Engineering Science* **2016**, *153*, 10 – 20. DOI: https://doi.org/10.1016/j.ces.2016.07.007

[229] T. Witoon, N. Kachaban, W. Donphai, P. Kidkhunthod, K. Faungnawakij, M. Chareonpanich, J. Limtrakul, *Energy Conversion and Management* **2016**, *118*, 21 – 31. DOI: https://doi.org/10.1016/j.enconman.2016.03.075

[230] M. Turco, G. Bagnasco, C. Cammarano, P. Senese, U. Costantino, M. Sisani, *Applied Catalysis B: Environmental* **2007**, *77 (1-2)*, 46 – 57.

DOI: https://doi.org/10.1016/j.apcatb.2007.07.006

[231] F. Arena, R. Giovenco, T. Torre, A. Venuto, A. Parmaliana, *Applied Catalysis B: Environmental* **2003**, *45 (1)*, 51 – 62. DOI: https://doi.org/10.1016/S0926-3373(03)00163-2

[232] R. Singh, K. Tripathi, K. K. Pant, J. K. Parikh, *Fuel* **2022**, *318*, 123641. DOI: https://doi.org/10.1016/j.fuel.2022.123641

[233] J. Y. Kim, J. A. Rodriguez, J. C. Hanson, A. I. Frenkel, P. L. Lee, *Journal of the American Chemical Society* **2003**, *125 (35)*, 10684 – 10692. DOI: https://doi.org/10.1021/ja0301673

[234] W. Kriprasertkul, T. Witoon, P. Kim-Lohsoontorn, *International Journal of Hydrogen Energy* **2022**, *47 (78)*, 33338 – 33351. DOI: https://doi.org/10.1016/j.ijhydene.2022.07.212

[235] J. Zhu, D. Ciolca, L. Liu, A. Parastaev, N. Kosinov, E. J. M. Hensen, *ACS Catal.* **2021**, *11 (8)*, 4880 – 4892. DOI: https://doi.org/10.1021/acscatal.1c00131

[236] L. Angelo, K. Kobl, L. M. M. Tejada, Y. Zimmermann, K. Parkhomenko, A.-C. Roger, *Comptes Rendus Chimie* **2015**, *18 (3)*, 250 – 260. DOI: https://doi.org/10.1016/j.crci.2015.01.001

[237] T. Tsoncheva, G. Issa, T. Blasco, P. Concepcion, M. Dimitrov, S. Hernández, D. Kovacheva, G. Atanasova, J. M. López Nieto, *Journal of colloid and interface science* **2013**, *404*, 155 – 160. DOI: https://doi.org/10.1016/j.jcis.2013.05.005

[238] V. L'hospital, L. Angelo, Y. Zimmermann, K. Parkhomenko, A.-C. Roger, *Catalysis Today* **2021**, *369*, 95 – 104. DOI: https://doi.org/10.1016/j.cattod.2020.05.018

[239] M. Kurtz, N. Bauer, C. Büscher, H. Wilmer, O. Hinrichsen, R. Becker, S. Rabe, K. Merz, M. Driess, R. A. Fischer, M. Muhler, *Catal Lett* **2004**, *92 (1/2)*, 49 – 52. DOI: https://doi.org/10.1023/B:CATL.0000011085.88267.a6

[240] S. Polierer, D. Guse, S. Wild, K. Herrera Delgado, T. N. Otto, T. A. Zevaco, M. Kind, J. Sauer, F. Studt, S. Pitter, *Catalysts* **2020**, *10 (8)*, 816. DOI: https://doi.org/10.3390/catal10080816

[241] M. R. Somalu, A. Muchtar, W. R. W. Daud, N. P. Brandon, *Renewable and Sustainable Energy Reviews* **2017**, *75*, 426 – 439. DOI: https://doi.org/10.1016/j.rser.2016.11.008

[242] H. Kirsch, *Dezentrale Synthese strombasierter flüssiger Kraftstoffe über die Fischer-Tropsch Route*, Dissertation, IMVT **2021**.

[243] C. Sun, *Direct syngas to fuel: integration of Fischer Tropsch synthesis and hydrocracking in micro structured reactors*, Dissertation, IMVT **2017**.

[244] S. Navarro-Jaén, M. Virginie, J. Thuriot-Roukos, R. Wojcieszak, A. Y. Khodakov, *J Mater Sci* **2022**, *57 (5)*, 3268 – 3279. DOI: https://doi.org/10.1007/s10853-022-06890-w

[245] D. Gamarra, G. Munuera, A. B. Hungría, M. Fernández-García, J. C. Conesa, P. A. Midgley, X. Q. Wang, J. C. Hanson, J. A. Rodríguez, A. Martínez-Arias, *J. Phys. Chem. C* **2007**, *111 (29)*, 11026 – 11038. DOI: https://doi.org/10.1021/jp072243k

[246] G. Marbán, A. B. Fuertes, *Applied Catalysis B: Environmental* **2005**, *57 (1)*, 43 – 53. DOI: https://doi.org/10.1016/j.apcatb.2004.10.011

[247] G. Bonura, C. Cannilla, L. Frusteri, E. Catizzone, S. Todaro, M. Migliori, G. Giordano, F. Frusteri, *Catalysis Today* **2020**, *345*, 175 – 182. DOI: https://doi.org/10.1016/j.cattod.2019.08.014

[248] D. Sheldon, *Johnson Matthey Technology Review* **2017**, *61 (3)*, 172 – 182. DOI: https://doi.org/10.1595/205651317x695622

[249] S. Kar, R. Sen, A. Goeppert, G. K. S. Prakash, *Journal of the American Chemical Society* **2018**, *140 (5)*, 1580 – 1583. DOI: https://doi.org/10.1021/jacs.7b12183

[250] M. Pérez-Fortes, J. C. Schöneberger, A. Boulamanti, E. Tzimas, *Applied Energy* **2016**, *161*, 718 – 732. DOI: https://doi.org/10.1016/j.apenergy.2015.07.067

[251] F. Arena, G. Italiano, K. Barbera, S. Bordiga, G. Bonura, L. Spadaro, F. Frusteri, *Applied Catalysis A: General* **2008**, *350 (1)*, 16 – 23. DOI: https://doi.org/10.1016/j.apcata.2008.07.028

[252] I. A. Fisher, A. T. Bell, *Journal of Catalysis* **1997**, *172 (1)*, 222 – 237. DOI: https://doi.org/10.1006/jcat.1997.1870

[253] W. Wang, S. Wang, X. Ma, J. Gong, *Chemical Society reviews* **2011**, *40 (7)*, 3703 – 3727. DOI: https://doi.org/10.1039/C1CS15008A

[254] X. Fang, Y. Men, F. Wu, Q. Zhao, R. Singh, P. Xiao, T. Du, P. A. Webley, *International Journal of Hydrogen Energy* **2019**, *44 (39)*, 21913 – 21925. DOI: https://doi.org/10.1016/j.ijhydene.2019.06.176

[255] S. Ren, W. R. Shoemaker, X. Wang, Z. Shang, N. Klinghoffer, S. Li, M. Yu, X. He, T. A. White, X. Liang, *Fuel* **2019**, *239*, 1125 – 1133. DOI: https://doi.org/10.1016/j.fuel.2018.11.105

[256] H. Zhang, W. Li, W. Xiao, *International Journal of Chemical Reactor Engineering* **2012**, *10 (1)*. DOI: https://doi.org/10.1515/1542-6580.3027

[257] A. Prašnikar, A. Pavlišič, F. Ruiz-Zepeda, J. Kovač, B. Likozar, *Ind. Eng. Chem. Res.* **2019**, *58 (29)*, 13021 – 13029. DOI: https://doi.org/10.1021/acs.iecr.9b01898

[258] S. Tauro, *One-Step Synthesis of Dimethyl Ether Using Microreactors*, IMVT **2013**.

[259] G. Bonura, F. Frusteri, C. Cannilla, G. Drago Ferrante, A. Aloise, E. Catizzone, M. Migliori, G. Giordano, *Catalysis Today* **2016**, *277*, 48 – 54.

DOI: https://doi.org/10.1016/j.cattod.2016.02.013

[260] A. Kornas, M. Śliwa, M. Ruggiero-Mikołajczyk, K. Samson, J. Podobiński, R. Karcz, D. Duraczyńska, D. Rutkowska-Zbik, R. GRABOWSKI, *Reac Kinet Mech Cat* **2020**, *130 (1)*, 179 – 194. DOI: https://doi.org/10.1007/s11144-020-01778-9

[261] H. R. Godini, S. R. Kumar, N. Tadikamalla, F. Gallucci, *International Journal of Hydrogen Energy* **2022**, *47 (21)*, 11341 – 11358.
DOI: https://doi.org/10.1016/j.ijhydene.2021.11.073

[262] E. Catizzone, G. Bonura, M. Migliori, G. Braccio, F. Frusteri, G. Giordano, *ACSM* **2019**, *43 (3)*, 141 – 149. DOI: https://doi.org/10.18280/acsm.430302

[263] G. Bonura, C. Cannilla, L. Frusteri, A. Mezzapica, F. Frusteri, *Catalysis Today* **2017**, *281*, 337 – 344. DOI: https://doi.org/10.1016/j.cattod.2016.05.057

[264] I. Miletto, E. Catizzone, G. Bonura, C. Ivaldi, M. Migliori, E. Gianotti, L. Marchese, F. Frusteri, G. Giordano, *Materials (Basel, Switzerland)* **2018**, *11 (11)*. DOI: https://doi.org/10.3390/ma11112275

[265] M. Migliori, E. Catizzone, A. Aloise, G. Bonura, L. Gómez-Hortigüela, L. Frusteri, C. Cannilla, F. Frusteri, G. Giordano, *Journal of Industrial and Engineering Chemistry* **2018**, *68*, 196 – 208. DOI: https://doi.org/10.1016/j.jiec.2018.07.046

[266] S. Navarro-Jaén, M. Virginie, J.-C. Morin, J. Thuriot-Roukos, R. Wojcieszak, A. Y. Khodakov, *New J. Chem.* **2022**, *46 (8)*, 3889 – 3900. DOI: https://doi.org/10.1039/D1NJ05734K

[267] A. García-Trenco, S. Valencia, A. Martínez, *Applied Catalysis A: General* **2013**, *468*, 102 – 111. DOI: https://doi.org/10.1016/j.apcata.2013.08.038

[268] R. Ladera, E. Finocchio, S. Rojas, G. Busca, J. Fierro, M. Ojeda, *Fuel* **2013**, *113*, 1 – 9. DOI: https://doi.org/10.1016/j.fuel.2013.05.083

[269] R. Ladera, E. Finocchio, S. Rojas, J. Fierro, M. Ojeda, *Catalysis Today* **2012**, *192 (1)*, 136 – 143. DOI: https://doi.org/10.1016/j.cattod.2012.01.025

[270] W. Ding, *Simulation-Assisted Design of Polycrystalline Zeolite Catalysts*, IMVT **2016**.

[271] B. Şeker, A. K. Dizaji, V. Balci, A. Uzun, *Renewable Energy* **2021**, *171*, 47 – 57. DOI: https://doi.org/10.1016/j.renene.2021.02.060

[272] H.-Y. Chen, J. Pihl, T. J. Toops, S. Sinha Majumdar, *Applied Catalysis A: General* **2023**, *656*, 119140. DOI: https://doi.org/10.1016/j.apcata.2023.119140

[273] J. W. Jung, Y. J. Lee, S. H. Um, P. J. Yoo, D. H. Lee, K.-W. Jun, J. W. Bae, *Applied Catalysis B: Environmental* **2012**, *126*, 1 – 8. DOI: https://doi.org/10.1016/j.apcatb.2012.06.026

[274] K. F. Kapiamba, H. O. Otor, S. Viamajala, A. C. Alba-Rubio, *Energy Fuels* **2022**, *36 (19)*, 11691 – 11711. DOI: https://doi.org/10.1021/acs.energyfuels.2c02131

[275] Y. Liu, *Top Catal*, in press. DOI: https://doi.org/10.1007/s11244-021-01495-0

[276] F. M. Kirchberger, Y. Liu, P. N. Plessow, M. Tonigold, F. Studt, M. Sanchez-Sanchez, J. A. Lercher, *Proceedings of the National Academy of Sciences of the United States of America* **2022**, *119 (4)*. DOI: https://doi.org/10.1073/pnas.2103840119

[277] A. Giuliano, E. Catizzone, C. Freda, *International journal of environmental research and public health* **2021**, *18 (2)*. DOI: https://doi.org/10.3390/ijerph18020807

[278] X. Jiang, X. Nie, X. Guo, C. Song, J. G. Chen, *Chemical reviews*

2020, *120 (15)*, 7984 – 8034. DOI: https://doi.org/10.1021/acs.chemrev.9b00723

[279] A. Aloise, A. Marino, F. Dalena, G. Giorgianni, M. Migliori, L. Frusteri, C. Cannilla, G. Bonura, F. Frusteri, G. Giordano, *Microporous and Mesoporous Materials* **2020**, *302*, 110198. DOI: https://doi.org/10.1016/j.micromeso.2020.110198

[280] L. Frusteri, G. Bonura, C. Cannilla, S. Todaro, G. Giordano, M. Migliori, F. Frusteri, *Pet. Chem.* **2020**, *60 (4)*, 508 – 515. DOI: https://doi.org/10.1134/S0965544120040076

[281] W. Wang, M. Seiler, M. Hunger, *J. Phys. Chem. B* **2001**, *105 (50)*, 12553 – 12558. DOI: https://doi.org/10.1021/jp0129784

Appendix

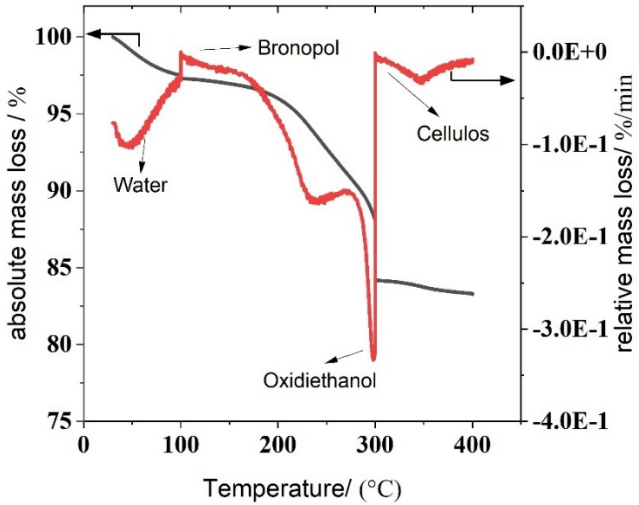

Figure A-1 Plot of absolute CZZ-Z-HLA-15%-PA sample mass versus temperature obtained from TGA analysis of screen-printing paste. The experiment was conducted in air at a heating rate of 2°C/min, with a hold time of 2 hours at 300°C, and a maximum temperature of 400°C.

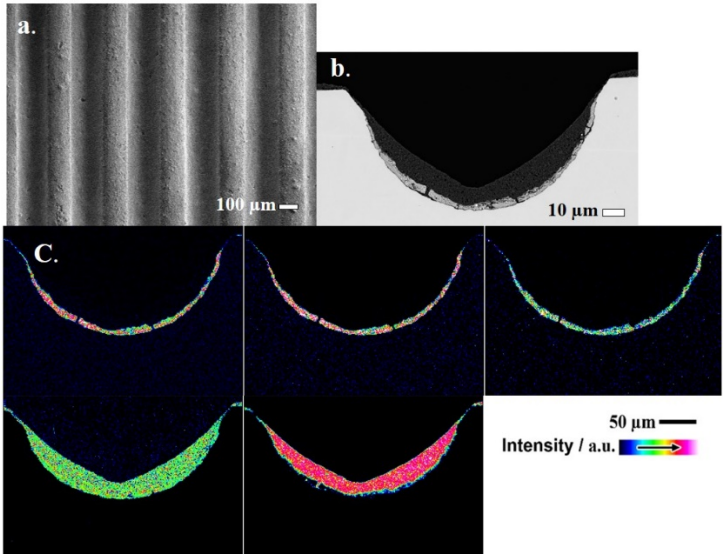

Figure A-2 Characterization of the CZC printed double layer: Top-view (a) SE-micrograph (b) cross-sectional analysis of the layer via EPMA/BSE, (c) elemental map via EPMA/WDX.

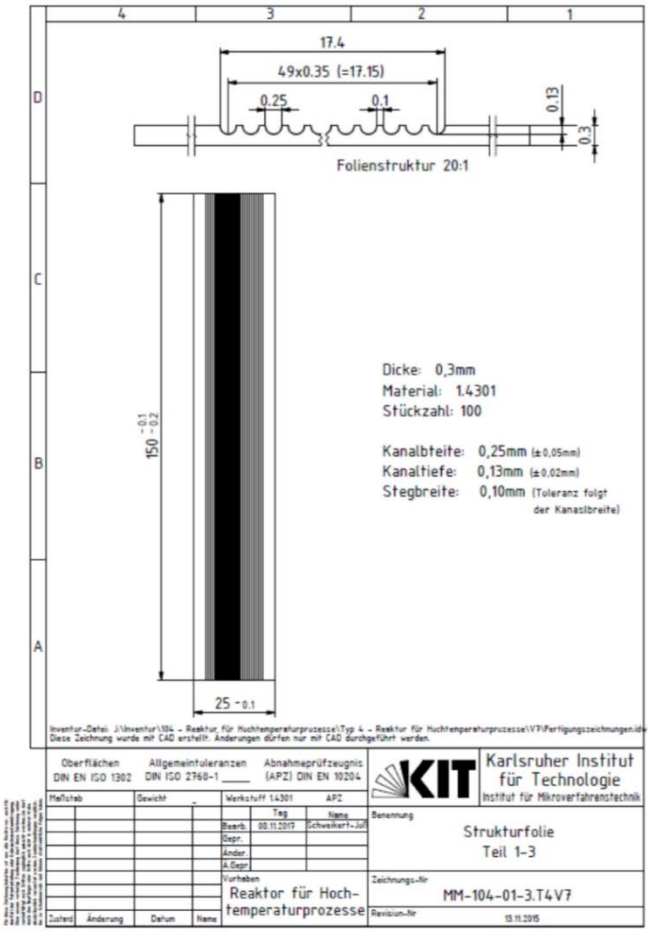

Figure A-3 Scheme and the dimension information of the foils used in the micro-channel reactor.

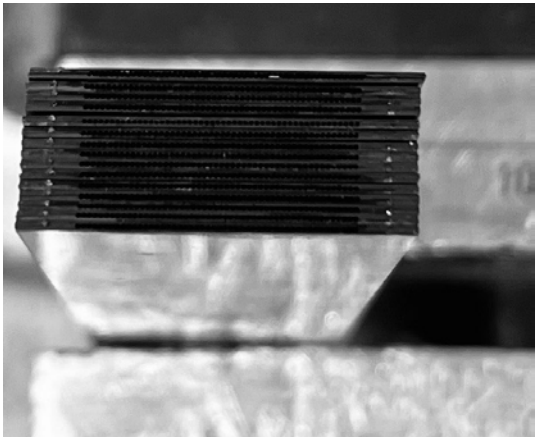

Figure A-4 30 stacked foils used in microchannel reactor.

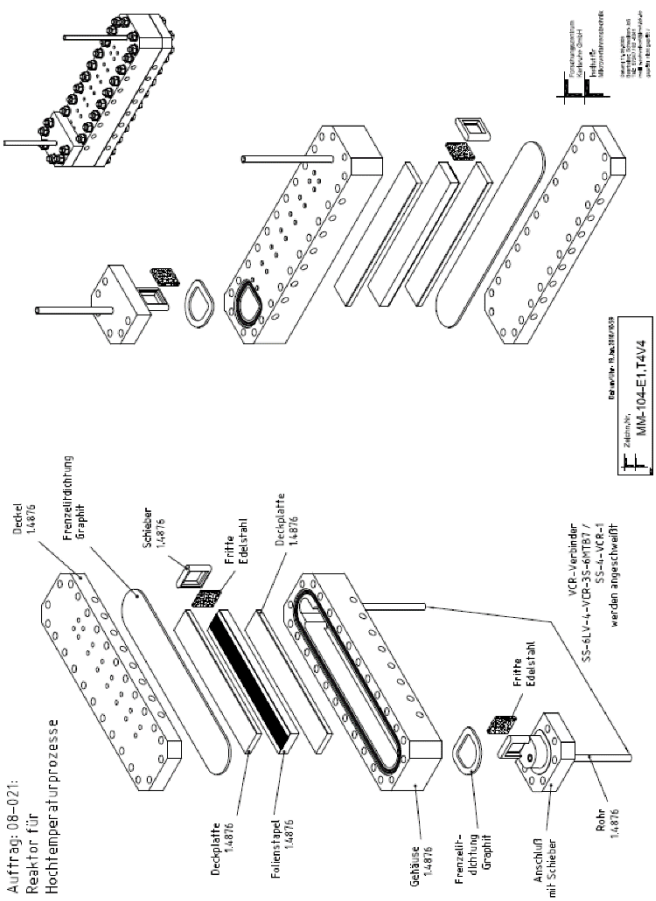

Figure A-5 Scheme of the Microchannel reactor.

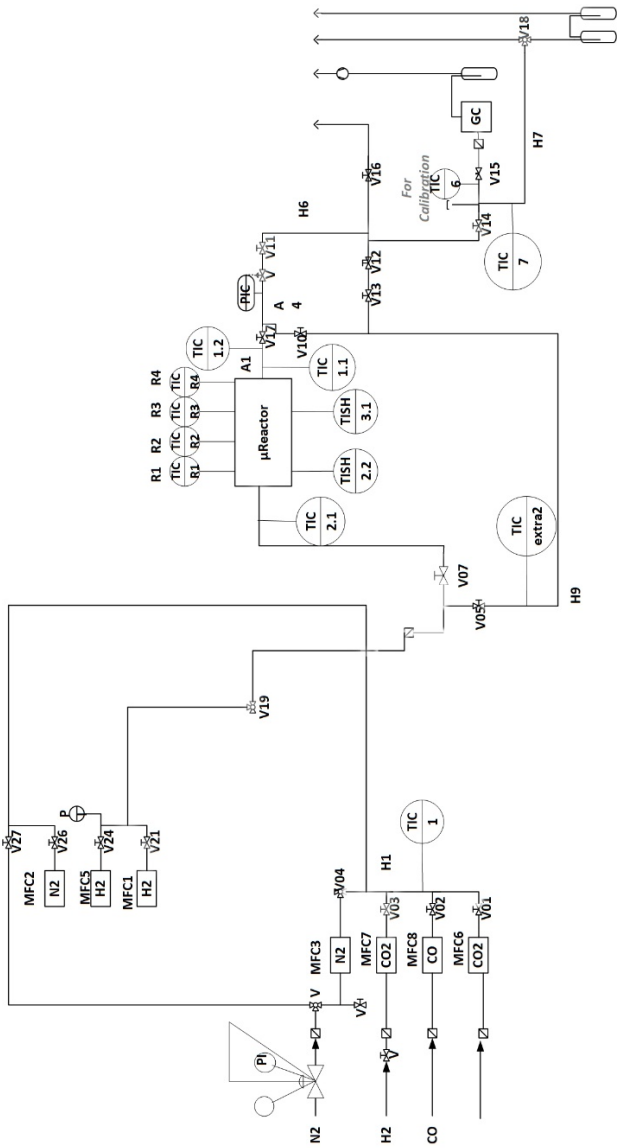

Figure A-6 Flow diagram of the experimental setup for the CTM-MTD integration study.

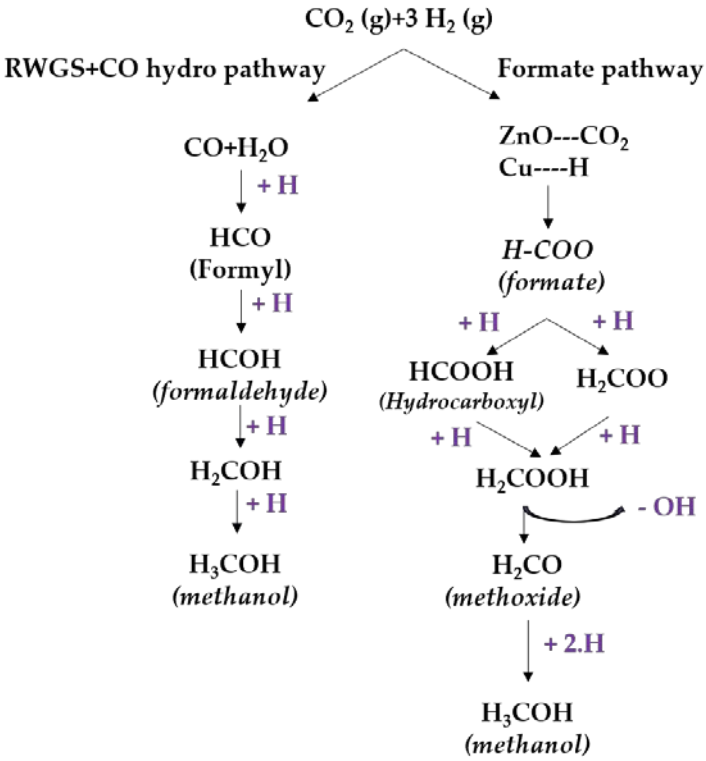

Figure A-7 CO_2 to methanol mechanisms: RWGS + CO hydrogenation vs formate pathway [273].

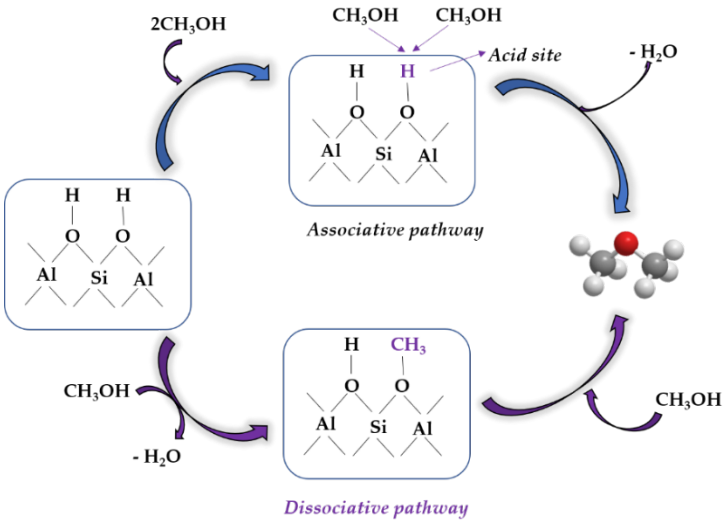

Figure A-8 Associative and dissociative routes of the methanol dehydration on acid sites.

Table A-1 Physico properties of zeolite (powder, paste and calcined paste).

	Zeolite (HZSM-5)		
	Powder	**Paste (dry)**	**Paste(calcined)**
BET surface area (m2/g)	398.8	376.3	377.8
Total pore volume (Cm^3/gr)	0.23	0.22	0.22
Micro pore volume (Cm^3/gr)	0.1	0.1	0.1
Average pore width (nm)	8.2	9.04	8.8